GALILEO GALILEI (GG)

TECHNICAL REPORT ON DRAG AND ATTITUDE CONTROL

DRL/DRD: DEL- 036

Written by	***Responsibility***
G. Sechi	Author
Verified by	
G. Catastini	Checker
Approved by	
	Product Assurance
	Configuration Control
	Design Engineer
	System Engineering Manager
A. Anselmi	Study Manager
Documentation Manager	
R. Cavaglià	

The validations evidence are kept through the documentation management system.

ISSUE	DATE	§ CHANGE RECORDS	AUTHOR
1	05/03/09	First issue submitted to IRR	
2	05/06/09	Issue submitted to PRR	

TABLE OF CONTENTS

1. SCOPE AND PURPOSE

The report provides synthesis of the results outcome from the activities executed in the frame of the WP 1B3-AD "Drag and Attitude Control Design" of the Phase A2 of the ASI program "Galileo Galilei".

The document provides:

- the review of experiment requirements and flow-down of experiment/mission requirements into drag and attitude requirements;
- detailed design of the control algorithms (drag and whirl) and implementation of them into software mathematical models;
- requirement for the drag-free actuators and sensors;
- attitude and drag-free control architecture;
- high level design of the operating modes, including both science modes and non-science modes;
- candidate equipment for attitude control.

The report starts from the spin-axis pointing accuracy and stability analyses on the new mission scenario (up to 3 years mission with respect to the 6/7 months considered in past). These because one of the major point outcomes of Phase A1 study (see [RD 1]) was the uselessness of spin-axis re-pointing control. At system level, it is necessary to understand if this result may be still considered valid and, if not, which solutions may be proposed to the Agency taking into account the reduced budget foreseen for the satellite.

The Drag-Free and Attitude Control (DFAC) architecture (mode organization and equipment) is described in chapter 6. The proposed solution has been conceived to permit both spin-stabilized and three-axis stabilized separations, opening the possibility to any multiple launches by VEGA launcher.

Chapter 7 copes with the derivation of drag-free requirements starting from high-level scientific requirements. They have been derived for XY plane, and Z axis drag-free controls.

Chapter 8 is dedicated to the most innovative aspects of the designed DFAC, i.e. the real-time compensation of the drag and the whirl stabilization. The algorithms for each control loop are described and mathematical models are provided.

Key technologies for the drag-free control like actuators and spin-rate sensor have been presented in chapters 9 and 10. It will be show that the already available micro-thrusters are very close to the GG requirements.

The candidate equipment for DFAC have been presented in chapter 11. Chapter 12 collects all results coming from numerical simulation obtained using a simulator environment representative for control design. They show the effectiveness of the studied control algorithms and their compatible with existing hardware equipment.

During Phase B, the overall design will be reviewed looking for any possible optimization and improvement.

2. REFERENCES

2.1 Applicable Documents

[AD 1]	ASI, "Progetto Galileo Galilei-GG Fase A-2, Capitolato Tecnico", DC-IPC-2007-082, Rev. B, 10-10-2007
[AD 2]	"Galileo Galilei Mission Requirement Document", SD-TN-AI-1167, Issue 1 draft, October 2008
[AD 3]	Experiment Concept and Requirements Document (ERD), SD-TN-AI-1163, Issue 1 draft, October 2008
[AD 4]	"Galileo Galilei System Technical Specification", SD-TN-AI-XXXX, Issue 1 draft, December 2008

2.2 Standards

[SD 1]	ECSS-M-00-02A, Space Project Management – Tailoring of Space Standards, 25 April 2000
[SD 2]	ECSS-E-ST-10C, Space Engineering - System Engineering General Requirements, 6 March 2009
[SD 3]	ECSS-E-10-02A, Space Engineering – Verification
[SD 4]	ECSS-Q-00A, Space Product Assurance - Policy and Principles, and related Level 2 standards.

2.3 Reference Documents

[RD 1]	GG Phase A Study Report, Nov. 1998, revised Jan. 2000, available at: http://eotvos.dm.unipi.it/nobili/ggweb/phaseA/index.html
[RD 2]	Supplement to GG Phase A Study (GG in sun-synchronous Orbit) "Galileo Galilei-GG": design, requirements, error budget and significance of the ground prototype", A.M. Nobili et al., Physics Letters A 318 (2003) 172–183, available at: http://eotvos.dm.unipi.it/nobili/documents/generalpapers/GG_PLA2003.pdf
[RD 3]	A. Nobili, DEL001: GG Science Requirements, Pisa, September 2008
[RD 4]	Arianespace, Vega User's Manual, Issue 3, Rev. 0, March 2006
[RD 5]	Selex GA private communication, 24 February 2009.
[RD 6]	TAS-I, "Mission and Payload Support Guide", PRIMA Class Platforms, Version 2.1E, July 2005
[RD 7]	E. Canuto, Critical Technologies Report: Microthrusters (DEL-43), to be provided
[RD 8]	F. Ceccanti, Preliminary Information on FEEP, GG.ALT.TN.2001, Jan 2009
[RD 9]	F. Ceccanti, Evaluation of Preliminary Thruster Requirement, GG.ALT.TN.2002, March 2009
[RD 10]	G. Matticari, Input on Cold Gas Thrusters for GG, TAS-I, draft, Jan 2009
[RD 11]	G. Catastini, Technical Report on Simulators (DEL-40), to be provided

[RD 12] S. Mottini, Critical Technologies Report: Spin Rate Sensor (DEL-43), to be provided

[RD 13] TAS-I document, Mission and Payload Support Guide, PRIMA Class Platforms, Version 2.1E, July 2005.

[RD 14] TAS-I internal note, Small GEO Cold Gas Propulsion, March 2009

[RD 15] J.L Crassidis, K.L. Lai, R.R. Harman, “Real-Time attitude-independent three-axis magnetometer calibration”, Journal of Guidance, Control, and Dynamics, Vol. 28, No. 1,

[RD 16] G. Natanson, “Attitude-Independent magnetometer calibration for spin-stabilized spacecraft”, January–February 2005

[RD 17] J.E.Sedlak, “Iterative magnetometer calibration”, AIAA/AAS Astrodynamics Specialist Conference, Keystone, CO, August 2006

[RD 18] P.C. Hughes, “Spacecraft attitude dynamics”, Dover Pubblications, Inc. Mineola, New York, 2004

[RD 19] TAS-I document, GO-TR-AI-0033, “GOCE PFM mass properties test report”, 21/04/2008

[RD 20] NASA Report, SP-8018, “Spacecraft Magnetic Torques”, March 1969.

[RD 21] R. Schafer, C. Heiden, “Eddy current losses of cylindrical conductors rotating in a magnetic field”, Applied Physics 9, 121-125, 1976

[RD 22] M. D. Shuster and S. D. Oh “Three-Axis Attitude Determination from Vector Observations”, Journal of Guidance and Control, Vol. 4, No. 1, January–February 1981, pp. 70–77.

3. INTRODUCTION

3.1 Background

The Galileo Galilei (GG) mission is a part of the Cosmology and Fundamental Physics project of the ASI Unit on Observation of the Universe, the purpose of which is providing support to the Italian Scientific Community in its participation in the European and worldwide development of knowledge in this field, both by independent projects and by international collaboration.

GG participates in the worldwide programme of verifying the founding principles of physics by means of groundbreaking experiments which can only performed in the space environment. The goal of GG is to test the “Equivalence Principle” (EP) to 1 part in 10^{17}, more than 4 orders of magnitude better than today’s ground experiments. As an EP experiment, GG shares the same goal as the STEP experiment of NASA and the Microscope experiment of CNES. Its contribution to the field consists in an original and innovative experiment concept, which promises an accuracy and precision unparalleled by any other experiment.

A one-g version of the differential accelerometer designed to fly onboard the GG satellite, called the GGG experiment, is currently operational in the INFN laboratory in San Piero a Grado, Pisa. It is designed to test the main features of the space instrument in a laboratory experiment. The GGG experiment is carried out with Istituto Nazionale di Fisica Nucleare (INFN) funding and ASI support.

The GG mission and satellite have already been studied at both scientific and industrial level. Between 1997 and 2000, a mission based on an equatorial orbit was studied under ASI contract [RD 1]. In 2001, adaptation of the mission to a sun-synchronous orbit, driven by launcher availability, was addressed [RD 2]. The successful launch of *Agile* has now demonstrated the feasibility for ASI of launching, at low cost, a small satellite into near perfectly equatorial orbit. Thus the equatorial orbit, which was preferred anyway because of simplicity of design and operation, can be taken again as the GG baseline.

The GG project of ASI is carried out in tight collaboration with INFN. ASI and INFN have signed an agreement for collaboration in a number of scientific projects. In the implementation phases of GG, if approved, ASI and INFN will sign a specific agreement which will define the contributions by each institution to the mission.

References for GG mission definition and design study are illustrated in [AD 1].

4. SPIN AXIS POINTING ACCURACY AND STABILITY

4.1 Introduction

In the following chapter, the problem of the long-term effect on spin-axis stability has been addressed.

The envisaged perturbations are:

- orbital plane precession;
- solar pressure;
- atmospheric drag;
- gravity gradient;
- residual magnetic dipole;
- eddy current;
- residual torque left by thrusters assembly.

A raw but conservative estimate of the resulting effect has been obtained overlapping each single effect (since the acceptable spin axis de-pointing for scientific measurements is in the order of 10÷15 deg, the system may be considered almost linear). Additional simplifications have been introduced in order to limit the computation complexity.

At the beginning of the mission, the satellite spin axis is aligned with the unit vector normal to the orbit plane. The orbit plane is nominally 5deg inclined.

As well known, only dedicated simulations provide confidence and reliable data on the spin-axis de-pointing during the mission lifetime. This does not limit in any case the value of the analysis executed because it provides sensitivity issues addressing.

4.2 Spacecraft spin-up and PGB release

The spin-up procedure increases the spacecraft angular rate around Z axis from values (i.e. 20-30deg/s us provided for example by Vega launcher) up to 360deg/s. During this phase, as it will be described later in the technical note (see chapter 6), the spin axis pointing direction is determinate by three axis magnetometer and Sun sensor.

Since when the spin-up is stopped the composite satellite+ plus PGB (PGB is still locked) spins around its major principal axis of inertia, and the principal axis of inertia processes around the satellite angular momentum vector with a constant nutation angle[1] equals to

$$\gamma = \operatorname{atan}\left(\frac{\|\boldsymbol{H}_t\|}{\|\boldsymbol{H}_a\|}\right) = \operatorname{atan}\left(\frac{I_t\|\boldsymbol{\omega}_t\|}{I_a\omega_S}\right) = \operatorname{atan}\left(\frac{I_t\sqrt{\omega_X^2+\omega_Y^2}}{I_a\omega_Z}\right)$$

---

[1] Actually, since the inertia along the transverse axes is not exactly the same (not axisymmetrical body), the precession trajectory is not a circle but an ellipse with small eccentricity.

After PGB release, it acts as a nutation damper and after a time TBD the spacecraft will spin around the angular momentum vector at the epoch (the angular momentum vector is moved by external perturbation as it will be analyzed later).

It is clear that after energy dissipation due to PGB suspension, the spacecraft will rotate around the angular momentum vector at the epoch, but the attitude control action may be oriented only to the pointing of the "best known" principal inertia major-axis. Considering negligible the movement of the angular momentum vector during the nutation damping phase, the angle between the angular momentum vector and the "best known" principal inertia major-axis depends on:

- uncertainty on the transformation between attitude control reference frame and principal inertia reference frame;
- residual angular rate $\|\boldsymbol{\omega}_t\|$.

The uncertainty on the transformation between attitude control reference frame and principal inertia reference frame depends on the inertia products amplitude and uncertainty. Taking into account that the uncertainty on mass properties measurement is better than ±1% (see [RD 18]), in order to limit the uncertainty to 0.5deg, it is necessary to have (TBC):

$$|I_{XY}| \le 0.02\ I_t$$
$$|I_{XZ}| \le 0.00125\ I_a$$
$$|I_{YZ}| \le 0.00125\ I_a$$

In order to limit the mispointing due to the residual angular rate at 0.1 deg, the residual angular rate on transverse axes shall be lower than 0.5deg/s.

After the separation between satellite and PGB, it will be possible to observe a negligible relative movement of the satellite and PGB centre of masses. Satellite and PGB are weakly coupled by the mechanical suspension acting also as nutation damper.

Spacecraft spin-axis pointing direction is affected by:

- orbital plane precession
- solar pressure;
- atmospheric drag;
- gravity gradient;
- residual magnetic dipole;
- eddy current;
- residual torque left by thrusters assembly.

PGB spin-axis pointing direction is instead affected by:

- orbital plane precession
- gravity gradient;
- eddy current.

Solar pressure and atmospheric drag act on spacecraft only, and the PGB interaction with magnetic field is limited by mu-metal used in PGB shield. The linear displacement between PGB and satellite are limited by drag-free control and whirl control. The relative rotation around spin axis is limited by an active angular rate and angular displacement control. The tilt between satellite spin axis and PGB spin axis shall be taken into account by mechanical stop sizing (the torsional rigidity of the suspension is very little to introduce a significant coupling).

4.3 How the computations have been performed

For a spin-stabilized satellite there are three characteristic times associated with the motion: the rotation period, the orbital period, and the lifetime (see [RD 17]). For GG, the rotation period is 1s, the orbital period is about 6000s, and the lifetime is in the range 3.16 10^7s (one year mission) and 6.32 10^7s (two years mission).

These three widely separated characteristic times are the basis for the most basic assumption used in the theoretical study of practical spin-stabilized spacecraft: the dynamics of the spin stabilization, the disturbances over one orbit, and the long-term motion of the angular momentum vector can be studied separately.

The variation on the angular momentum vector $\Delta\boldsymbol{H}$ due to environmental disturbances is computed according to the following scheme:

- the effect of the instantaneous perturbing torque is computed in body frame/orbital frame and averaged on the rotation period ($\Delta\overline{\boldsymbol{H}}$);
- the mean torque resulting from previous computation is averaged on one orbit ($\Delta\overline{\overline{\boldsymbol{H}}}$) or one day;
- the small $\Delta\overline{\overline{\boldsymbol{H}}}$ is integrate to establish how the spin orientation evolves over mission duration time.

The following formula and definition will be considered in the following:

$$\Delta\boldsymbol{H} = \Delta\overline{\overline{\boldsymbol{H}}}\,\frac{T_M}{T_O}$$

$$\Delta\overline{\overline{\boldsymbol{H}}} = \overline{\overline{\boldsymbol{T}}}_O\, T_O$$

$$\Delta\overline{\boldsymbol{H}} = \overline{\boldsymbol{T}}_O\, T_S$$

$$\overline{\boldsymbol{T}}_O = \frac{1}{T_S}\int_0^{T_S} \boldsymbol{T}_O\, dt$$

$$\overline{\overline{\boldsymbol{T}}}_O = \frac{1}{T_O}\int_0^{T_O} \overline{\boldsymbol{T}}_O\, dt$$

being:

T_M : satellite lifetime/mission duration time
T_O : orbital period
T_S : spin period
$\bar{\boldsymbol{T}}_O$: torque averaged on one spin period in the orbital reference frame
$\bar{\bar{\boldsymbol{T}}}_O$: torque averaged on one orbital period (or in one day) in the orbital reference frame

4.4 Orbital plane precession

Since the orbit plane is not in the Equator plane, a precession exists. It occurs around the Earth Gravitation field North pole, with amplitude 5deg. The maximum deviation of the spin-axis with respect its init direction becomes 10deg.

Precession angular rate reads

$$\omega_P = -\frac{3}{2}\left(\frac{R_\oplus}{R_\oplus + H}\right)^2 \omega_{ORB} J_{2\oplus} \cos(i)$$

For GG, the precession angular rate is equal to 1.4633 10^{-6} rad/s, which corresponds to a period of 49.7 days.

4.5 Solar radiation pressure

The resultant of the solar pressure force is applied at the centre of pressure. The spacecraft rotates around its major principal axis of inertia. The satellite centre of mass does not coincide with the centre of symmetry of the external structure, which result in a movement of the centre of pressure with respect to the satellite spin axis.

For the specific case, it is convenient to consider directly the effect of the torque

$$\bar{\boldsymbol{T}}_O = \frac{1}{T_S}\int_0^{T_S}\left(\boldsymbol{r}_{CS\_O} - \boldsymbol{r}_{COM\_O}\right)\times \boldsymbol{F}_{SP}\,dt \cong \frac{1}{T_{SPIN}}\left(\left(\int_0^{T_S}\boldsymbol{r}_{CS\_O}\,dt\right) - \boldsymbol{r}_{COM\_O}\right)\times \boldsymbol{F}_{SP}$$

where:
$\boldsymbol{r}_{CS\_O}$: position of the centre of pressure
$\boldsymbol{r}_{COM\_O}$: position of the satellite COM
$\boldsymbol{F}_{SP}$: solar pressare force

Developing about formula, it results:

- solar pressure provides a torque on spin axis and another normal to it;
- taking into account the seasonality effects and precession period, it is possible to say that on mission duration, the average value of the spacecraft spin rate will not change;
- torque component normal to the angular momentum is responsible of the precession around the Sun line of sight.

In a simplified way, it results:

$$\bar{T}_O = \left\|\bar{\boldsymbol{T}}_O\right\| = F_O \bar{d}$$

$$\Delta\vartheta = \frac{F_0 \bar{d}}{I_a \omega_S} \Delta t$$

$$\omega_P = \frac{F_0 \bar{d}}{I_a \omega_S}$$

The solar pressure force is about 10-5 N (see chapter 15), and the position of the COM and the CP may be in the order of few centimetres. The CP position with respect to the COM depends on satellite design and initial trimming, solar panels and other surface differential ageing.

For example, if $d = 0.1m$ than $\omega_P = 1.0616\text{e-}009$. It means that in 1 years mission the angular momentum vector moves of about 1.9deg, and after 2 years 3.8deg.

Taking into account experience gained in other missions, it is possible to consider $d < 0.05m$ or better. Hereafter, it has been assumed 0.025 as bound for uncertainty position for each axis, that is representative for $d < 0.035m$. Considering a factor 100% of margin on the estimated perturbing force, this corresponds to an angular momentum vector movement of 2.7deg for two years mission.

Actually, the movement of the angular momentum vector is more complex due to the season movement of the Sun line of sight in the inertial reference frame.

4.6 Atmospheric drag

The resultant of the drag force is applied at the centre of area (centre of area and centre of pressure are in general not coincident). The drag may be managed as the solar pressure, taking into account that the force change direction during the orbit.

Due to the tilt of the satellite spin axis with respect to the unit vector normal to the orbital plane, there are a rotating force component in the satellite XY plane, and another one almost constant along Z axis. In the following the tilt is considered negligible.

In a preliminary a simplified way, it is possible consider the drag force rotating in the orbital plane and with amplitude periodic as well.

$$F_O = \left(F_0 + F_1\cos(\omega_{ORB}t+\varphi_1) + F_2\cos(2\omega_{ORB}t+\varphi_2)\right)\cos(\omega_{ORB}t)$$

The torque reads

$$T_O = \bar{d}\left(F_0 + F_1\cos(\omega_{ORB}t+\varphi_1) + F_2\cos(2\omega_{ORB}t+\varphi_2)\right)\cos(\omega_{ORB}t)$$

It results:

- the constant drag force is responsible of a little periodic movement of the angular momentum vector due to dF_0 (nutation oscillation);
- angular momentum vector drift proportional to $\frac{dF_1}{2}$.

The amplitude of the small nutation oscillation reads

$$\gamma = \frac{\bar{d}F_0}{I_a\omega_{ORB}\omega_S}$$

From the drift it derives an angular momentum vector angular movement equals to:

$$\Delta\vartheta = \frac{\bar{d}F_1}{2I_a\omega_S}\Delta t$$

Considering the drag force estimated in see chapter 15, and $\bar{d} = 0.1m$, $\frac{\Delta\vartheta}{\Delta t} = 1.3e-9$. After one year mission, the expected de-pointing is lower than 2.4 deg, and after two years lower it is lower than 4.8deg.

Taking into account experience on other spacecraft, it is possible to consider $d < 0.05m$ or better. Hereafter, it has been assumed 0.025 as bound for uncertainty position for each axis, that is representative for $d < 0.035m$. This corresponds to an angular momentum vector movement of 3.3 deg for two years mission.

In first approximation, the spin rate is not affected by drag-torque.

4.7 Gravity Gradient

As indicated in [RD 17], the effect of the gravity gradient is a precession of the satellite and PGB around the unit vector normal to the orbital plane at the epoch.

The precession angular rate reads:

$$\omega_P = -\left(\frac{3(\omega_{ORB})^2}{2} \frac{(I_a - I_t)}{I_a \omega_{SPIN}} \right) \cos(\vartheta) = -\left(\frac{3(\omega_{ORB})^2}{2\omega_{SPIN}} \left(\frac{\Delta I}{I_a} \right) \right) \cos(\vartheta)$$

Where ϑ is the angle between the spin axis and the normal to the orbital plane. If spin axis is perfectly aligned with the normal to the orbital plane or it is in the orbital plane, the precession does not exist. To minimize the spin-axis movement (minimization of the precession rate), $\frac{\Delta I}{I_a}$ should be reduced as much as possible. This contrasts with stability of the spin axis requirement, by which the spin axis shall be the higher inertia moment with margin (at least 15÷20%). If $\frac{\Delta I}{I_a} = 0.2$, considering for example $\vartheta = 5\deg$, it results a precession period equals to 7.50e+007 s (2.38 years).

The relative movement between PGB and satellite spin axes shall be compatible with mechanical stop design. In any case, to reduce such a displacement the $\frac{\Delta I}{I_a}$ for satellite without PGB and PGB shall be as close as possible.

The spin rate is not affected by gravity gradient torque.

4.8 Residual magnetic dipole

Spacecraft residual magnetic dipole interacts with the Earth magnetic field giving rise to a instantaneous torque equal to

$$\boldsymbol{T} = \boldsymbol{\mu}_B \times \boldsymbol{B}$$

being

$\boldsymbol{\mu}_B$: spacecraft magnetic dipole;

$\boldsymbol{B}$: Earth's magnetic field.

The spacecraft magnetic dipole depends on current loop and materials subject to permanent or induced magnetism. Since the force required for drag-compensation changes in body axis with period equal to the spin period, it seams possible to consider:

$$\boldsymbol{\mu}_B = \begin{bmatrix} \mu_{X0} + \mu_{X1C}\cos(\omega_{S\_ORB}t) + \mu_{X1S}\sin(\omega_{S\_ORB}t) + \mu_{X2C}\cos(2\omega_{S\_ORB}t) + \mu_{X2S}\sin(2\omega_{S\_ORB}t) + \dots \\ \mu_{Y0} + \mu_{Y1C}\cos(\omega_{S\_ORB}t) + \mu_{Y1S}\sin(\omega_{S\_ORB}t) + \mu_{Y2C}\cos(2\omega_{S\_ORB}t) + \mu_{Y2S}\sin(2\omega_{S\_ORB}t) + \dots \\ \mu_{Z0} + \mu_{Z1C}\cos(\omega_{S\_ORB}t) + \mu_{Z1S}\sin(\omega_{S\_ORB}t) + \mu_{Z2C}\cos(2\omega_{S\_ORB}t) + \mu_{Z2S}\sin(2\omega_{S\_ORB}t) + \dots \end{bmatrix}$$

with

$$\omega_{S\_ORB} = (\omega_S - \omega_{ORB})$$
$$\mu_{X1C} \cong \mu_{Y1S}$$
$$\mu_{X1S} \cong -\mu_{Y1C}$$

Considering the simple dipole model:

$$\boldsymbol{B} = B_0\left[\hat{\boldsymbol{k}}_m - 3\left(\hat{\boldsymbol{r}} \bullet \hat{\boldsymbol{k}}_m\right)\hat{\boldsymbol{r}}\right]$$

where

$\hat{\boldsymbol{k}}_m$: unit vector for the Earth North magnetic Pole;

$\hat{\boldsymbol{r}}$: unit vector associated to the spacecraft position .

The instantaneous torque in body axis results

$$\boldsymbol{T}_B = \boldsymbol{\mu}_B \times \boldsymbol{B}_B = \boldsymbol{\mu}_B \times \left({}_O\boldsymbol{R}_B{}^T\boldsymbol{B}_O\right)$$

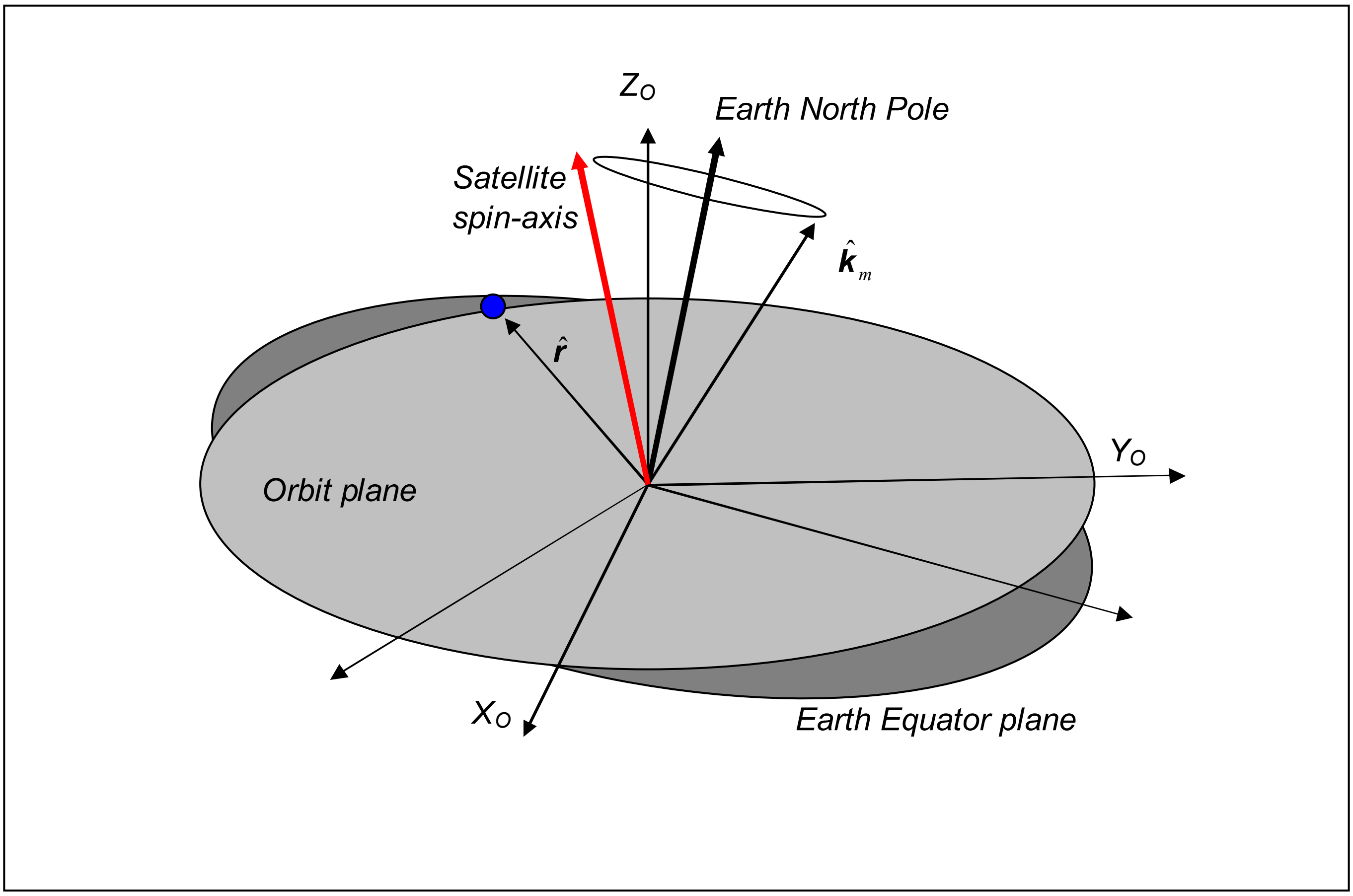

Figure 4-1 – Reference frames used for the computation

$$ {}_{O}\boldsymbol{R}_{B} = \begin{bmatrix} \cos(\psi) & -\sin(\psi) & 0 \\ \sin(\psi) & \cos(\psi) & 0 \\ 0 & 0 & 1 \end{bmatrix} $$

$$ \boldsymbol{B}_{O} = B_{0}\left[{}_{O}\boldsymbol{R}_{E}\hat{\boldsymbol{k}}_{m} - 3\left(\hat{\boldsymbol{r}}\bullet{}_{O}\boldsymbol{R}_{E}\hat{\boldsymbol{k}}_{m}\right)\hat{\boldsymbol{r}} \right] $$

being

$$ {}_{O}\boldsymbol{R}_{E} = \begin{bmatrix} 1 & 0 & 0 \\ 0 & \cos(i) & \sin(i) \\ 0 & -\sin(i) & \cos(i) \end{bmatrix} $$

$$ \hat{\boldsymbol{k}}_{m} = \begin{bmatrix} \sin(\delta)\cos(\omega_{E}t + \varphi_{E}) \\ \sin(\delta)\sin(\omega_{E}t + \varphi_{E}) \\ \cos(\delta) \end{bmatrix} $$

$$ \hat{\boldsymbol{r}} = \begin{bmatrix} \cos(\omega_{O}t) \\ \sin(\omega_{O}t) \\ 0 \end{bmatrix} $$

δ : tilt of the Earth Magnetic Pole with respect to the Earth North geographic pole
ω_E : Earth rotation angular rate
ω_O : satellite orbit rate

The instantaneous torque in inertial orbit plane becomes

$$ \boldsymbol{T}_{O} = {}_{O}\boldsymbol{R}_{B}\boldsymbol{T}_{B} = {}_{O}\boldsymbol{R}_{B}\left[\boldsymbol{\mu}_{B} \times \left({}_{O}\boldsymbol{R}_{B}{}^{T}\boldsymbol{B}_{O}\right)\right] $$

$$ {}_{O}\boldsymbol{R}_{B} = \boldsymbol{R}_{X}(\vartheta_{1})\boldsymbol{R}_{Y}(\vartheta_{2})\boldsymbol{R}_{Z}(\vartheta_{3}) $$

Assuming that during one satellite rotation (1s, which corresponds to an angle shift of about 0.06deg) the local magnetic field does not change ($\boldsymbol{B}_O = \overline{\boldsymbol{B}}_O$), and small spin-axis tilt angles ϑ_1 and ϑ_2 with respect to the normal to the orbit plane

$$ \overline{\boldsymbol{T}}_{O} = \frac{1}{2}\begin{bmatrix} B_{Z}\left(\mu_{X1S} + \mu_{Y1C} - 2\mu_{Z0}\vartheta_{1}\right) - B_{Y}\left(\mu_{X1S}\vartheta_{1} + \mu_{Y1C}\vartheta_{1} + 2\mu_{Z0} - \mu_{X1C}\vartheta_{2} + \mu_{Y1S}\vartheta_{2}\right) \\ B_{X}\left(\mu_{X1S}\vartheta_{1} + \mu_{Y1C}\vartheta_{1} + 2\mu_{Z0} - \mu_{X1C}\vartheta_{2} + \mu_{Y1S}\vartheta_{2}\right) - B_{Z}\left(\mu_{X1C} - \mu_{Y1S} + 2\mu_{Z0}\vartheta_{2}\right) \\ -B_{X}\left(\mu_{X1S} + \mu_{Y1C} - 2\mu_{Z0}\vartheta_{1}\right) + B_{Y}\left(\mu_{X1C} - \mu_{Y1S} + 2\mu_{Z0}\vartheta_{2}\right) \end{bmatrix} $$

For ϑ_1 and ϑ_2 equals to 0

$$\overline{\boldsymbol{T}}_O = \frac{1}{2}\begin{bmatrix} B_Z\mu_{X1S} - 2B_Y\mu_{Z0} + B_Z\mu_{Y1C} \\ -B_Z\mu_{X1C} + 2B_X\mu_{Z0} + B_Z\mu_{Y1S} \\ -\left(B_X\mu_{X1S} + B_X\mu_{Y1C} - B_Y\mu_{X1C} + B_Y\mu_{Y1S}\right) \end{bmatrix}$$

Since the magnetic field changes with respect to orbital reference frame with periodicity one day, instead to consider the average on one orbit, it has been considered more significant to compute the average on one day. Then

$$\overline{\overline{\boldsymbol{T}}}_O = \frac{1}{T_{DAY}}\int_0^{T_{DAY}} \overline{\boldsymbol{T}}_O dt$$

Only magnetic field component shall be averaged

$$\overline{\overline{\boldsymbol{B}}}_O = \frac{1}{T_{ORB}}\int_0^{T_{ORB}} \overline{\boldsymbol{B}}_O dt$$

$$\overline{\overline{\boldsymbol{T}}}_O \cong \frac{1}{2}\begin{bmatrix} \overline{\overline{B}}_Z\left(\mu_{X1S} + \mu_{Y1C}\right) - 2\overline{\overline{B}}_Y\mu_{Z0} \\ -\overline{\overline{B}}_Z\left(\mu_{X1C} - \mu_{Y1S}\right) \\ \overline{\overline{B}}_Y\left(\mu_{X1C} - \mu_{Y1S}\right) \end{bmatrix}$$

Considering $\vartheta_1 = 0$, $\vartheta_2 = 0$, $i = 5\deg$ e , the average magnetic field has been computed considering the simplified dipole model; results are given in Table 4-1.

$\overline{\overline{B}}_X$	$\overline{\overline{B}}_Y$	$\overline{\overline{B}}_Z$
3.0720e-008	-1.3379e-006	2.9337e-005

Table 4-1 - One day-average magnetic field (in Tesla)

The relevant contributors to the torque are:

- dipole constant term along Z body axis;
- dipole first harmonic terms along X and Y body axes.

Considering $\mu_{X1C} \cong \mu_{Y1S}$ and $\mu_{X1S} \cong -\mu_{Y1C}$, $\overline{\overline{\boldsymbol{T}}}_O$ becomes

$$\overline{\overline{\boldsymbol{T}}}_O \cong \begin{bmatrix} -B_Y\mu_{Z0} \\ 0 \\ 0 \end{bmatrix}$$

The interaction with the magnetic field is responsible of a drift, that in 2 years mission results

$$\Delta\vartheta = \frac{1.4\ 10^{-6}}{I_a\omega_{SPIN}}\, 6.32\ 10^{7}\,\mu_{Z0} = 0.094\,\mu_{Z0} rad$$

For a constant dipole of about 1Am2 on Z body axis, a spin axis drift of about 5.4 deg in 2 years occurs ($\vartheta_1 = 0$, $\vartheta_2 = 0$). It means that the residual magnetic dipole along Z axis shall be reduced to no more than 0.3÷0.6 Am^2 to add a drift no greater than 2÷3 deg.

Using a more conservative approach that considers $\mu_{X1C} \cong \mu_{Y1S}$ and $\mu_{X1S} \cong -\mu_{Y1C}$ with a residual of about 20% with respect to μ_{Z0} (i.e. $|\mu_{X1}| = 0.2|\mu_{Z0}|$), it is possible to obtain:

$$\bar{\bar{\boldsymbol{T}}}_O \cong \begin{bmatrix} B_Z \\ -B_Z \\ B_Y \end{bmatrix} \mu_{X1} + \begin{bmatrix} B_Y \\ 0 \\ 0 \end{bmatrix} \mu_{Z0} = \left(\begin{bmatrix} 30\,10^{-6} \\ 30\,10^{-6} \\ 1.4\,10^{-6} \end{bmatrix} 0.1 + \begin{bmatrix} 1.4\,10^{-6} \\ 0 \\ 0 \end{bmatrix} \right) \mu_{Z0} = \begin{bmatrix} 3.3 \\ 3 \\ 0.14 \end{bmatrix} 10^{-6} \mu_{Z0}$$

The resulting drift becomes

$$\left\| \bar{\bar{T}}_{XY} \right\| \cong 9.5\,10^{-6}\,\mu_{Z0}$$

$$\left\| \bar{\bar{T}}_{Z} \right\| \cong 0.28\,10^{-6}\,\mu_{Z0}$$

$$\Delta\vartheta = \frac{9.5\ 10^{-6}}{I_a \omega_{SPIN}} \mu_{Z0} 6.32\,10^{7} = 0.64 \mu_{Z0} rad$$

and de-spin

$$\frac{\Delta\omega}{\omega_S} = \frac{0.28\ 10^{-6}}{I_a} \mu_{Z0} 6.32\,10^{7} = 0.12 \mu_{Z0}$$

To limit the spin axis de-pointing to 5 deg in two years mission, $\mu_{Z0} < 0.14 Am2$. It is a strong requirement to be achieved also for a little satellite like GG.

From above analysis, it is evident that $\mu_{X1C} \cong \mu_{Y1S}$ and $\mu_{X1S} \cong -\mu_{Y1C}$ shall be as close as possible, with acceptable differences in the order of no more 10% and $\mu_{Z0} < 0.3 Am2$ (to be reviewed during early B phase).

4.9 Eddy current

The following chapter starts from [RD 19].

Since the satellite moves with respect to the magnetic field vector, torques caused by induced currents (named eddy currents but also known as Foucault current) and the irreversible magnetization of permeable materials (hysteresis effects) must be considered. They produce dissipative torques (damping torques).

In general, an accurate assessment of these torques is extremely difficult and simplifying assumptions regarding the shape of the spinning section, its electro-magnetic properties (electrical conductivity), and the nature of the interaction with the ambient field are required to approximate the magnetic field effects.

The instantaneous value of the eddy current damping torque on a body whose angular velocity vector is $\boldsymbol{\omega}$ in a magnetic field $\boldsymbol{B}$ is

$$\boldsymbol{T} = -k_e\, \boldsymbol{B} \times (\boldsymbol{\omega} \times \boldsymbol{B})$$

where k_e is a constant that depends on the geometry and electromagnetic properties of the rotating object.

The despin component of torque reads

$$T_{DE} = -k_e\,(B_\perp)^2\,\omega_S$$

being

$B_\perp$: component of $\boldsymbol{B}$ orthogonal to the spin axis
ω_S : spin angular velocity

The spin axis acceleration caused by eddy current is

$$\dot{\omega}_S = -k_e\,\frac{(B_\perp)^2}{I_a}\,\omega_S$$

The precession component of torque reads:

$$T_{PE} = -k_e\, B_\perp B_{|}\, \omega_S$$

where

$B_\parallel$: component of $\boldsymbol{B}$ parallel to the spin axis

For GG satellite and PGB, two elementary shape may be considered:

- thin spherical shell
- circular loop
- thin-walled cylinder.

For a thin spherical shell, with radius r, thickness d, and static electrical conductivity σ

$$k_e = \frac{2}{3}\pi\,\sigma\, r^4\, d$$

For a circular loop, located in a plane through the spin axis, with radius r, cross-sectional area S, and conductivity σ

$$k_e = \frac{\pi}{4}\sigma\, r^3\, S$$

For a thin-walled cylinder, with length L, radius r, thickness τ and static electrical conductivity σ

$$k_e = \pi\,\sigma\, r^3\, L\,\tau \left(1 - \frac{2\tau}{L}\tanh\left(\frac{L}{2\tau}\right)\right)$$

The computation has been done following the same approach outlined for the computation of magnetic dipole.

The instantaneous value of the torque is equal to:

$$\boldsymbol{T}_O = {}_O\boldsymbol{R}_B \boldsymbol{T}_B = {}_O\boldsymbol{R}_B \left[-k_e \left({}_O\boldsymbol{R}_B{}^T \boldsymbol{B}_O\right) \times \left(\boldsymbol{\omega} \times \left({}_O\boldsymbol{R}_B{}^T \boldsymbol{B}_O\right)\right)\right]$$

$${}_O\boldsymbol{R}_B = \boldsymbol{R}_X(\vartheta_1)\boldsymbol{R}_Y(\vartheta_2)\boldsymbol{R}_Z(\vartheta_3)$$

Considering $\vartheta_1 = \vartheta_2 = 0$, the averaged torque becomes

$$\overline{\boldsymbol{T}}_O = -k_e\ \omega_S \begin{bmatrix} 0 \\ 0 \\ B_X^2 + B_Y^2 \end{bmatrix}$$

Considering the movement on one day, the

$$\overline{\overline{\boldsymbol{T}}}_O = -k_e\ \omega_S \begin{bmatrix} 0 \\ 0 \\ \overline{\overline{B}}{}_X^2 + \overline{\overline{B}}{}_Y^2 \end{bmatrix}$$

$\overline{\overline{B}}{}_X^2$ and $\overline{\overline{B}}{}_Y^2$ have been computed using the simplified dipole model; results are provided in

$\overline{\overline{B}}{}_X^2$	$\overline{\overline{B}}{}_Y^2$
4.8623e-011	4.9997e-011

Table 4-2 - One day-average magnetic field

$$\dot{\omega}_S = -\frac{k_e\,\omega_S}{I_a}10^{-10}$$

$$\frac{\Delta\omega_S}{\omega_S} = -\frac{k_e}{I_a}10^{-10}\,\Delta t$$

In order to stay inside an angular rate variation of 10% in three years mission, the resulting satellite k_e shall be lower than 1500.

A preliminary assessment of the k_e has been done considering the two 6Al-4V Titanium tanks (high conductivity, large component). The thin spherical shell model has been considered, with $r = 0.158m$, $d = 0.015m$ and $\sigma = 5.85\;10^5 m^{-1}\Omega^{-1}$. It results $k_e = 11.4534$ for each tank. It seams that we are far from significant satellite de-spin due to eddy currents.

The PGB has the external cover constituted by aluminium honeycomb and carbon fibers, with inside a cover in mu-metal. Since the PGB inertia moment around spin axis is in the order of 1kgm^2, in order to limit the PGB de-spin to 10% in two years mission then $k_e < 15.7$.

Preliminarily and considering the PGB external cover a cylinder with with length 0.5m, radius 0.3m, the mu-metal layer shall not be larger than 0.1÷0.2 mm ($\sigma_{mumetal} = 1.73\,10^6\,\Omega^{-1}m^{-1}$) (TBC) (see [RD 20] [RD 21]).

Above computation shall be considered as preliminary, also taking into account the well known difficulties in the design of magnetic shields.

4.10 Residual torque in body axis.

Due to thrusters' misalignment and mounting position errors, and due to the uncertainty on COM position, the actual thrust left by thrusters is never zero. Considering typical mounting error and uncertainty on thrust direction provided by FEEP, residual torque shall be considered by design.

Using FEEP and depending on the selected assembly, the residual torque increases after thruster failure.

This residual torque is correlated to the commanded force, and that it is periodic (see for example Figure 9-16). Each component may be written as:

$$T_B = \left(T_0 + T_1\cos(\omega_{S\_ORB}t + \varphi_1) + T_2\cos(\omega_{S\_ORB}t + \varphi_2) + \ldots\right)$$

$$T_B = \left(T_0 + T_1\cos(\omega_{S\_ORB}t + \varphi_1) + T_2\cos(\omega_{S\_ORB}t + \varphi_2) + \ldots\right)$$

where

$\omega_{S\_ORB} = \left(\omega_S - \omega_{ORB}\right)$

The instantaneous torque reads:

$$\boldsymbol{T}_O = {}_O\boldsymbol{R}_B \boldsymbol{T}_B$$

$$\boldsymbol{T}_B = \begin{bmatrix} T_{X0} + T_{X1C}\cos(\omega_{S\_ORB}t) + T_{X1S}\sin(\omega_{S\_ORB}t) + T_{X2C}\cos(2\omega_{S\_ORB}t) + T_{X2S}\sin(2\omega_{S\_ORB}t) + \ldots \\ T_{Y0} + T_{Y1C}\cos(\omega_{S\_ORB}t) + T_{Y1S}\sin(\omega_{S\_ORB}t) + T_{Y2C}\cos(2\omega_{S\_ORB}t) + T_{Y2S}\sin(2\omega_{S\_ORB}t) + \ldots \\ T_{Z0} + T_{Z1C}\cos(\omega_{S\_ORB}t) + T_{Z1S}\sin(\omega_{S\_ORB}t) + T_{Z2C}\cos(2\omega_{S\_ORB}t) + T_{Z2S}\sin(2\omega_{S\_ORB\,SPIN}t) + \ldots \end{bmatrix}$$

As it will show further in the technical note, a satellite spin-rate control has been foreseen to maintain satellite and PGB relative position and velocity. This means that also after 1 failure, no spurious action on Z axis may be tolerated. Residual torque is possible only around X and Y axes.

The average torque on a rotation reads:

$$\bar{\boldsymbol{T}}_O = \frac{1}{2}\begin{bmatrix} T_{X1C} - T_{Y1S} + 2T_{Z0}\vartheta_2 \\ T_{X1S} + T_{Y1C} - 2T_{Z0}\vartheta_1 \\ \left(T_{X1S} + T_{Y1C}\right)\vartheta_1 + 2T_{Z0} - \left(T_{X1C} - T_{Y1S}\right)\vartheta_2 \end{bmatrix}$$

For $\vartheta_1 = \vartheta_2 = 0$, it becomes

$$\bar{\boldsymbol{T}}_O = \frac{1}{2}\begin{bmatrix} T_{X1C} - T_{Y1S} \\ T_{X1S} + T_{Y1C} \\ 2T_{Z0} \end{bmatrix}$$

The first harmonic torque is responsible for the drift of angular momentum vector:

$$\Delta\vartheta = \frac{T_{XY1}}{2I_a\omega_S}\Delta t$$

$$T_{XY1} = \sqrt{\left(T_{X1C} - T_{Y1S}\right)^2 + \left(T_{X1S} + T_{Y1C}\right)^2}$$

and then

$$T_{XY1} < \frac{2I_a\omega_S\Delta\vartheta}{\Delta t}$$

For a maximum de-pointing of the spin axis not greater than $\Delta\vartheta = 1\,\mathrm{deg}$ in 1 years mission, than the $T_{XY1} < 1\,10^{-6}\ \mathrm{Nm}$. It is very strong requirement after first failure, if compared with the result provided in Figure 9-16 (about 25 times greater), that suggest to review the proposed assembly (cluster configuration or number of clusters[2]) or two accept such a degradation of performance after first failure.

4.11 Simulation results

In order to show the complexity of the interaction between perturbing actions, two simulations have been executed.

Both assume at the beginning a spacecraft with Z-axis perfectly aligned with the normal to the orbit plane.

First simulation is long 1.5 year and it considers one FEEP fault, leaving residual perturbing torque in body frame with significant first harmonic magnitude (see Figure 9-16). Satellite dipole and residual perturbing torque has been provided in Table 4-3.

After 1.5 year mission, de-pointing magnitude is about 11deg (see Figure 4-2, blue curve is the nominal spin axis movement due to orbit plane precession). In the considered case, satellite de-spin is negligible (see Figure 4-2). The considered results are clearly much better with respect to may be predicted considering each perturbing torque independently.

	μ_0	μ_{1C}	μ_{1S}	μ_{2C}	μ_{2S}
X	-0.3 Am2	0.05 Am2	0.05 Am2	0.0	0.0
Y	-0.3 Am2	0.05 Am2	-0.05 Am2	0.0	0.0
Z	0.3 Am2	0.03 Am2	0.03 Am2	0.0	0.0
	T_0	T_{1C}	T_{1S}	T_{2C}	T_{2S}
X	5 μNm	0.0	5 μNm	0.0	0.0
Y	-2.5 μNm	0.0	-30 μNm	0.0	0.0
Z	0.0 μNm	0.0	0.0	0.0	0.0

Table 4-3 – Parameter considered for first simulation (drag, solar pressure, gravity gradient are active too).

---

[2] Using three clusters instead of 2 the residual torque becomes significant only after more than one FEEP failure.

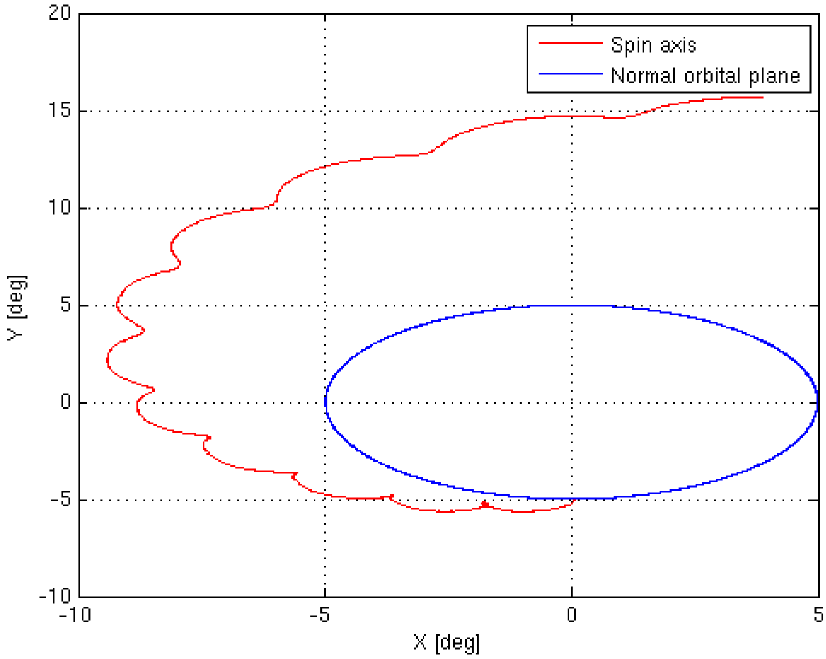

Figure 4-2 – Spin axis evolution for 1year mission after one FEEP fault (residual perturbing torque not zero).

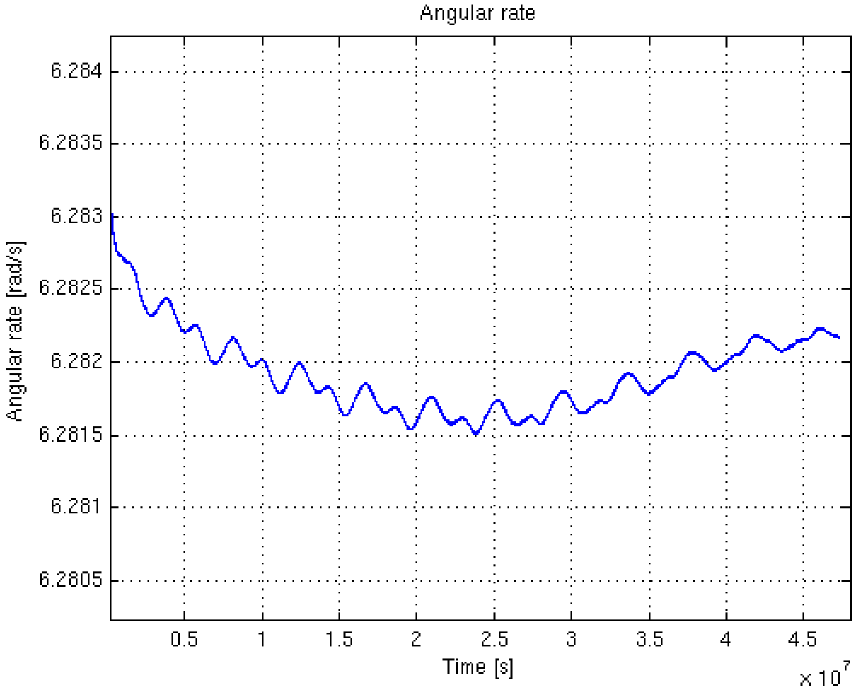

Figure 4-3 – Spin rate evolution for 1year mission after one FEEP fault (residual perturbing torque not zero).

Second simulation is long about 1.2 years, without FEEP failure (see parameters in Table 4-4). After about 14 months, the de-pointing magnitude is lower than 1deg (see Figure 4-4, blue curve is the nominal spin axis movement due to orbit plane precession). In the considered case, satellite de-spin is negligible and comparable with that observed for first simulation (see Figure 4-5).

	μ_0	μ_{1C}	μ_{1S}	μ_{2C}	μ_{2S}
X	-0.3 Am2	0.05 Am2	0.05 Am2	0.0	0.0
Y	-0.3 Am2	0.05 Am2	-0.05 Am2	0.0	0.0
Z	0.3 Am2	0.03 Am2	0.03 Am2	0.0	0.0
	T_0	T_{1C}	T_{1S}	T_{2C}	T_{2S}
X	0.0	0.0	0.0	0.0	0.0
Y	0.0	0.0	0.0	0.0	0.0
Z	0.0	0.0	0.0	0.0	0.0

Table 4-4 – Parameter considered for second simulation (drag, solar pressure, gravity gradient are active too).

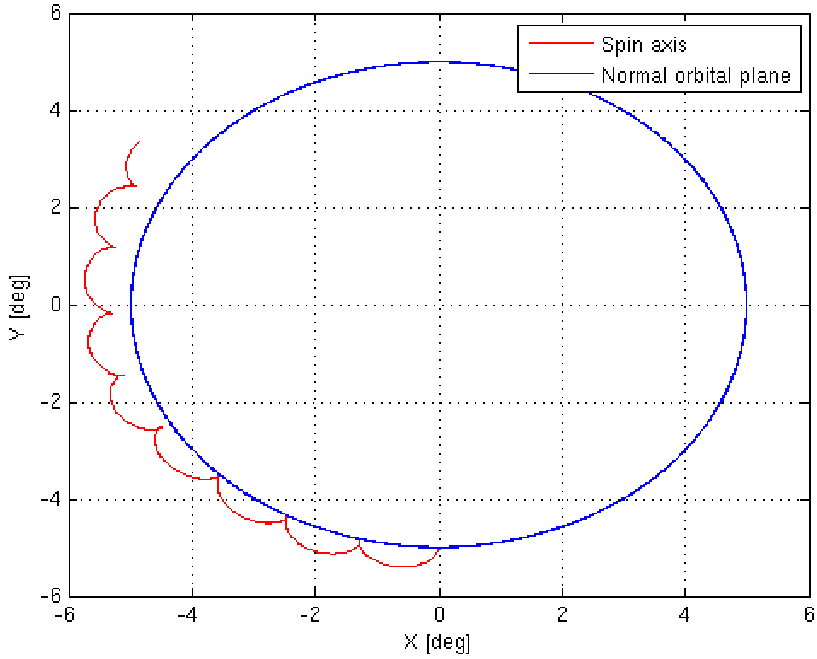

Figure 4-4 – Spin axis evolution for 14 months (residual perturbing torque zero).

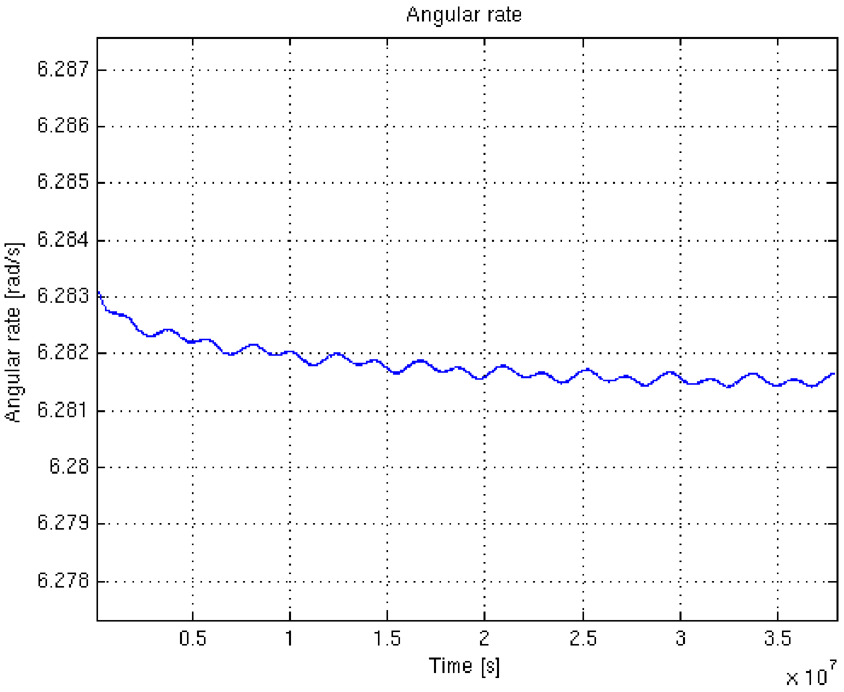

Figure 4-5 – Spin rate evolution for 14 months (residual perturbing torque zero).

4.12 Conclusions and budget

In previous chapters it has been shown the spin-axis de-pointing and angular rate reduction of satellite and PGB due to the interaction with the space environment.

Several simplifications have been done to maintain the computation complexity manageable. The obtained results are in any case useful to estimate a sort of worst case, to drive the spacecraft design, the equipment and material selection.

Synthesis of derived results is provided in Table 4-5. Table 4-6 shows the same results after 2 years mission (without FEEP failure).

Perturbing source	**Satellite spin axis**	**Satellite de-spin**	**PGB spin axis**	**PGB de-spin [%/year]**
orbital plane precession	5 deg	-	5 deg	-
solar pressure	1.3 deg/year	-	-	-
atmospheric drag	1.6 deg/year		-	-
gravity gradient				
residual magnetic dipole	3 deg/year (*)	4%/year	-	-
eddy current		negligible		5%/year (****)
residual torque left by thrusters assembly	1deg/year (**) 20deg/year (***)	Active control foreseen	-	-

(*) allocation, see chapter 4.8
(**) no FEEP failure (allocation to be assessed)
(***) after FEEP failure (current assembly). It may accepted taking into account cost limits and FEEP reliability
(****) mumethal shield as indicated in chapter 4.9

Table 4-5 – Yearly satellite and PGB spin-axis de-pointing and de-spin.

Perturbing source	**Satellite spin axis [deg]**	**Satellite de-spin [%]**	**PGB spin axis [deg]**	**PGB de-spin [%]**
Attitude determination error	1			
Control error	0.5			
Uncertainty on principal inertia frame attitude	0.5			
orbital plane precession	5		5	
solar pressure	2.7			
atmospheric drag	3.3			
gravity gradient				
residual magnetic dipole	6(*)	8%		

eddy current				10%
residual torque left by thrusters assembly	2 (**)			
Total de-pointing	21	8%	5	10%

(*) allocation, see chapter 4.8
(**) no FEEP failure (allocation)
(***) after FEEP failure (current assembly)
(****) mumethal shield as indicated in chapter 4.9

Table 4-6 – Budget for satellite and PGB spin-axis de-pointing and de-spin for 2 years mission

5. DRAG-FREE AND ATTITUDE CONTROL ARCHITECTURE

5.1 Functional description

The Drag-Free and Attitude Control (DFAC) has in charge:

- before PGB unlock:
  - the spacecraft attitude control after launcher separation, in order to guarantee safe power and communication conditions;
  - spacecraft spin-up to achieve the spin rate required by scientific observation (360deg/s);
- after PGB unlock:
  - the stabilization of whirl control;
  - drag compensation with very high rejection to permit the detection of the EP violation (if any);
  - the control of the spacecraft spin-rate and of the PGB-spacecraft relative spin angle. It is necessary for PGB suspension, sensors and actuators integrity.

5.2 Operating modes organization

Depending on the separation conditions (pre-defined attitude, spin-rate, attitude and angular rate errors) different scenario may be envisaged for the starting operating phase of the spacecraft.
According to [RD 4], two separation options are available using Vega launcher:

- 3-axis stabilisation;
- spin stabilization around the upper composite longitudinal axis.

The accuracy provided by launcher in terms of orbital parameters and attitude accuracy are given in Table 5-1.

DFAC mode organization has been designed to be compliant with both separation options in order to permit different launch opportunities.

Considering a spin stabilized separation, the spacecraft Z-axis may be considered close to required one with errors lower than 5÷10deg half-cone. The separation conditions with a spin rate close to the maximum allowed (30deg/s) gives an enough gyroscopic stability achieving safe power and communication operating conditions.

In the three axis stabilized separation option, the attitude control system shall provide:

- rate damping;
- Sun acquisition and slow-spin up of the spacecraft around Z-axis, to provide a slow but effective spin-stabilization for fuel saving.

No	Parameter	Unit	Value	Comments
	Injection accuracy (700km altitude, 3σ)			
1	Altitude error	km	15	
2	Inclination	deg	0.15	
3	Argument of perigee	deg	-	
4	RAAN	deg	0.3	
	Three-axis stabilized mode (3σ)			
5	Longitudinal axis de-pointing	deg	1	
6	Transversal axis de-pointing	deg	1.5	
7	Angular tip-off rates along longitudinal axis	deg/s	0.6	
8	Angular tip-off rates along transversal axis	deg/s	1.0	
	Spin stabilized mode (3σ)			
9	Max spin rate	deg/s	30	
10	Spin rate accuracy	deg/s	1	@ 30 deg/s
11	Transverse angular tip-off rates	deg/s	0.6	@ 30 deg/s
12	Nutation	deg	5	@ 30 deg/s, half angle

Table 5-1 - Vega launcher performances (see [RD 4])

After separation, the residual angular rate is damped to be lower than 0.1deg/s. Then, the spacecraft is slewed in order to have the spacecraft z-axis close to the final required pointing (Earth Z-axis). The rate-damping may be obtained using coarse gyroscope. The pointing close to the Earth z-axis may be obtained using magnetometer tanks to the almost equatorial orbital plane. The spin-axis pointing may be improved after early ground contacts and orbit determination, using an on-board orbit propagator and Earth magnetic model.

Taking into account the spacecraft geometry, any attitude providing the spacecraft Z-axis almost normal with the orbit plane may be considered safe for power and communication

In order to permit higher accuracy with respect to what it may be expected using only magnetometer also after in-flight calibration (key procedure), it has been retained convenient to consider another sensor (fine Sun sensor) to improve spin-axis pointing. Using such equipment, the determination of satellite spin-axis pointing will be possible during the overall spacecraft mission.

The separation occurs with AOCS in Stand-By Mode (SBM). After separation in stabilized three-axis mode, the Rate Damping Mode (RDM) is activated to reduce the angular rate, and then the Coarse Pointing Mode (CPM) is autonomously activated to steer the spacecraft Z-axis toward the local magnetic field, and to introduce a weak spin stabilization to save propellant. In such a way, taking into account the satellite shape, safe power and communication conditions will be met. After on-ground orbit determination, the pointing may be improved thank to an on-board Earth Magnetic Field model.

After separation in spin stabilized mode, the spacecraft kinematics condition are almost the same that the exit condition from CPM (FPM entry conditions).
Improving the pointing conditions is in charge of Fine Pointing Mode (FPM) using Sun sensor.

In Spin-Up Mode (SUM), the angular rate around spacecraft Z axis will be increased up to 360deg/s (±10%). Satellite Z-axis pointing direction is estimated starting from magnetometer, Sun sensor, on-board Sun propagator, orbit propagator and Earth magnetic model. Before starting SUM, the three-axis flux-gate magnetometers shall be calibrated to recover bias, scale factor, non orthogonality errors.

When the required angular rate is achieved (spin rate equal to 360deg/s, transversal angular rate close to zero), transition in Spin Stabilized Mode (SSM) is commanded.

In SSM, after PGB unlock, DFAC shall guarantee PGB integrity, by stabilization of PGB-satellite relative movement (whirl control, spin rate and PGB-satellite rotation around spin axis control).

In Drag-Free Mode (DFM), the drag compensation in the XY plane and Z axis is done in parallel with whirl control, spin rate and PGB-satellite rotation control. The drag is captured by capacitive sensors (CapS) as relative movement between PGB and satellite. The drag compensation and the spin-rate control are done by micro-propulsion (μProp); whirl stabilization actuators are capacitive actuators (CapA). DFM is quite complex, due to the spin nature of the satellite. In order to meet the very demanding requirement on drag attenuation (greater than 50000), very accurate measurement of the satellite spin rate is needed (Spin Rate Sensor (SpRS) is used for such a purpose).

The transition between SSM and DFM is commanded any time the scientific observation is required. Back-transition from DFM to SSM is convenient for fuel saving (no-drag compensation).

No attitude control for spin-axis re-pointing has been foreseen during scientific phase. Analysis executed in the frame of the study show that limiting the mission to two years and managing carefully system aspects like residual magnetic dipole and residual unwanted torque, the expected de-pointing is still acceptable for scientific purpose. This aspect will be re-considered in early phase B.

5.3 Failure detection, isolation and recovery approach.

The rate damping phase and the alignment of the spacecraft Z-axis with the Earth magnetic field are typically the most critical operating phases for the mission. With respect other three-axis stabilized spacecraft, for GG a power safe condition is achieved as far as the Z-axis is almost close to the Earth pole direction. With the dispersion introduced by Earth magnetic pole daily movement, attitude error and seasonality, the Sun aspect angle (normal to the satellite solar array plane) is in the range 12÷35deg. After the initialization of the on-board spacecraft orbit-propagator (2-3 orbits after launcher separation), it is possible to compensate the Earth magnetic pole daily movement and to align the spacecraft Z-axis with the Earth pole direction, or other more suitable direction taking into the specific season (Sun Aspect Angle <23.5deg).

Since the rate damping and Sun acquisition is “critical phase” they are full covered by multiple sensors: it is possible to detect and isolate the first failure. This operating requirement is met by three three-axis magnetometers and four one-axis gyroscope. In the case of only two three axis gyro will be considered, an additional functional redundancy unit may be provided building in real time the angular rate by magnetometer measurement.

Since the orbital plane is inclined with only 5 deg with respect to the equatorial plane, using magnetometers only it is not possible to have during one orbit the full angular rate observability. In any case, to access the functionality of one gyro, the comparison based only on the observable part is enough.

During early phase of the mission, switch on of the sun sensor is possible, and monitoring of SAA is possible, in addition to other classical monitoring based on battery low voltages.

The spin-up phase is another mission critical phase due to the limitation of fuel and final pointing requirements of the spin-axis and residual angular rate.

In this phase the attitude is build considering magnetometers and Sun sensors. Both the sun sensors are switched on (they will be mounted in opposite direction, to permits more measurement during spinning phase). Using Sun measurement the spacecraft angular rate will be derived and compared with that provided by rate sensors, and magnetometers. Using magnetometer, EMF model it will possible to predict the sun elevation angle. At the end, it will possible to build several additional sensors to monitor the correct evolution of spin-up phase.

Mode	GYRO	MGM	SSS	SpRS	CapS	RCS	µProp	CapA
Stand-By								
Rate Damping	●					●		
Coarse Pointing	●	●				●		
Fine Pointing	●	●	●			●		
Spin-Up	●	●	●			●		
Spin Stabilized	×	×	×		●		●	●
Drag-Free	×	×	×	●	●		●	●

Table 5-2 – Equipment versus operating mode

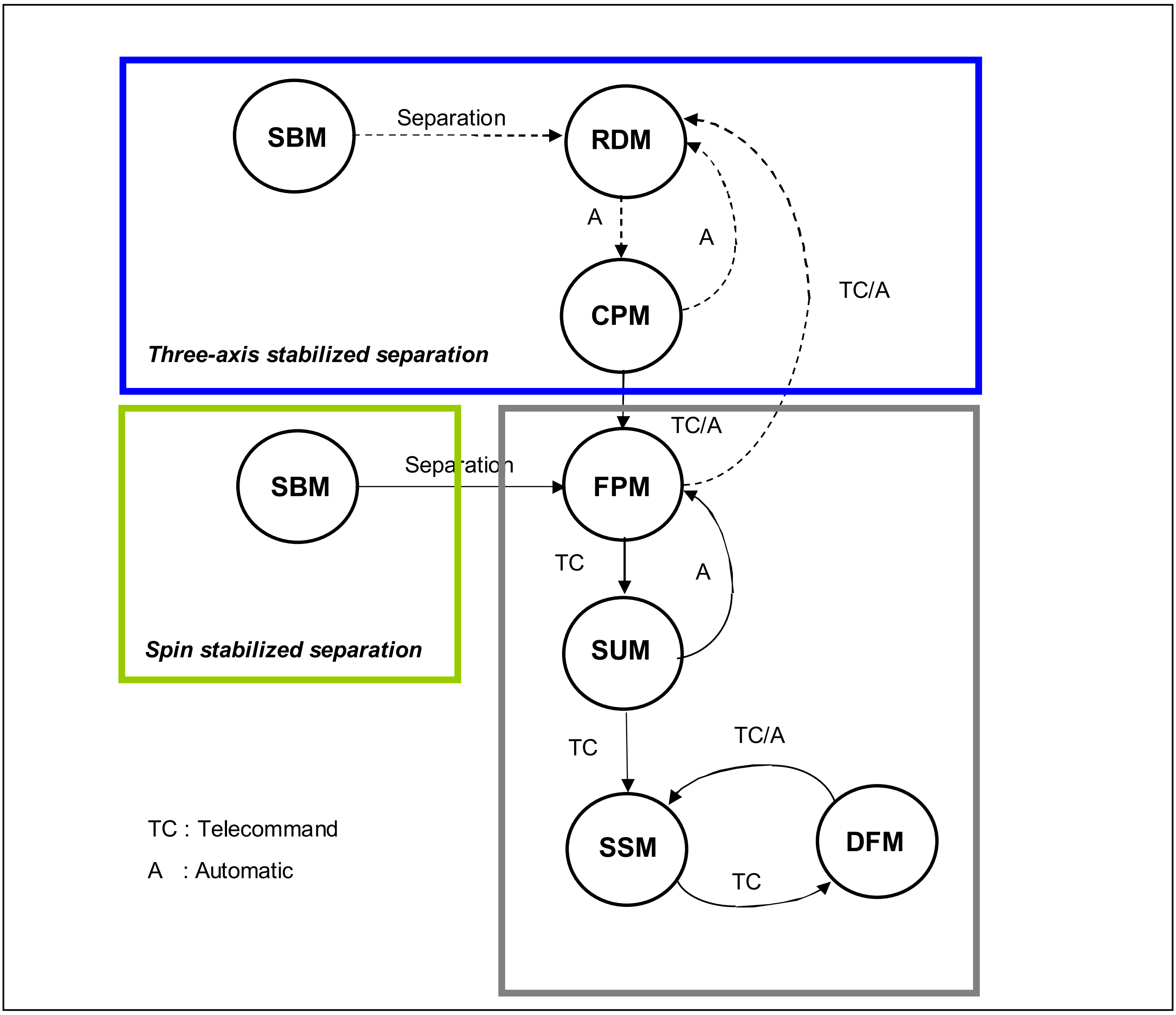

Legend	
SBM	Stand-By Mode
RDM	Rate Damping Mode
CPM	Coarse Pointing Mode
FPM	Fine Pointing Mode
SUM	Spin-Up Mode
SSM	Spin Stabilized Mode
DFM	Drag-Free Mode (scientific mode)

Figure 5-1 - DFAC mode organization.

6. ATTITUDE CONTROL DESIGN

6.1 Introduction

Hereafter, the design of the attitude control algorithm mode will be described.

As written in chapter 5, the number of attitude control modes depends on the separation conditions (in spin stabilized mode or in three axes stabilized mode).

Although the design of Rate Dumping Mode and the Coarse Pointing Mode do not present particularly criticism, it seams possible to take them from PRIMA platform design. In particular, with minor changes, the Safe Hold Mode (SHM) and Emergency Mode (EM) may be re-used (see [RD 12]). This observation limits the number of control modes to be designed to the Fine Pointing Mode (FPM), satellite Spin-Up Mode (SUM) and Drag-free mode (DFM).

6.2 Rate Dumping

The rate-dumping has in charge the decreasing satellite angular momentum after separation. The mode uses coarse rate sensor to measure the angular rate, and cold-gas thrusters as actuators.

The control law may be very simple like:

$$\boldsymbol{T}_R = -[\boldsymbol{I}][\boldsymbol{K}_V]\tilde{\boldsymbol{\omega}}$$

being:

$\boldsymbol{T}_R$: required control torque to be applied by RCS

$$\boldsymbol{T}_R = \begin{bmatrix} T_{R\_X} \\ T_{R\_Y} \\ T_{R\_Z} \end{bmatrix}$$

$[\boldsymbol{I}]$: inertia matrix based only on inertia moments

$$[\boldsymbol{I}] = \begin{bmatrix} I_{XX} & 0 & 0 \\ 0 & I_{YY} & 0 \\ 0 & 0 & I_{ZZ} \end{bmatrix}$$

$[\boldsymbol{K}_V]$: gain matrix for the

$$[\boldsymbol{K}_V] = \begin{bmatrix} K_{V\_X} & 0 & 0 \\ 0 & K_{V\_Y} & 0 \\ 0 & 0 & K_{V\_Z} \end{bmatrix}$$

$\tilde{\boldsymbol{\omega}}$: measured angular rate

$$\tilde{\boldsymbol{\omega}} = \begin{bmatrix} \tilde{\omega}_X \\ \tilde{\omega}_Y \\ \tilde{\omega}_Z \end{bmatrix}$$

In order to improve the performances, an observer may be introduced. The observer shall embed the dynamic relation between applied torque and angular rate, and a simplified model of perturbing torque. The estimated torque will be put as feed-forward in control law introducing a sort of integrative action.

Rate dumping is a classical operating mode. It may be also derived from the Safe Hold Mode (SHM) provided in PRIMA platform (see [RD 12]).

6.3 Coarse Pointing Mode

CPM has in charge the pointing of the satellite Z axis as close as possible to the Earth Mean Rotation axis at the epoch. In CPM, the Earth Mean Rotation axis is approximated at the first stage by the local Earth magnetic field. After on-ground orbit determination, the correct direction of the Earth Mean Rotation axis may be pointed taking into account the actual local magnetic field.

The CPM points the satellite Z-axis and introduces a small angular rate around it to have a small gyroscopic stabilization, useful for fuel saving.

Coarse Rate Sensors and Magnetometer are used as sensors[3]; cold-gas thrusters are used as actuators.

CPM may be derived from the Emergency Mode (EM) provided in PRIMA platform (see [RD 12]), or as particular case of the logic designed for spacecraft spin-up.

6.4 Spacecraft spin-up

Spin-up Mode shall increase the angular rate up to 360deg/s, corresponding to a magnitude of the angular momentum of about 950Nms.

---

[3] The Sun sensor may be used too, if closer Sun pointing will be envisaged during the phase B design.

The equipment used by SUM may be: Gyroscope, Sun sensor, magnetometer, and cold-gas thrusters. The attitude determination will be based on magnetometer and Sun sensor; the gyroscope will be used only in eclipse and for FDIR.

Taking into account the high angular rate, the magnetometer and the sun sensor shall be acquired with a sampling frequency not lower than 10÷20Hz. The magnetometer shall provide an extended bandwidth (not lower than 10Hz) or well known delays to limit the uncertainties on measured magnetic field (additional systematic errors), and specific in-flight calibration shall be considered.

The attitude determination is done according to the TRIAD (see [RD 22]) method that suit very well for such kind of application. The satellite inertial spin-axis pointing is computed using:

- inertial Sun direction (to be provided by a Sun propagator);
- inertial Earth magnetic field (to be computed using satellite orbit propagator, time propagator and Earth magnetic field model);
- on-board measured sun direction;
- on-board measured magnetic field.

Let be:

$\hat{\boldsymbol{n}}_1, \hat{\boldsymbol{n}}_2$ non-parallel reference unit vectors in inertial reference frame;

$\tilde{\boldsymbol{n}}_1, \tilde{\boldsymbol{n}}_2$ measured unit vectors related to previous non-parallel reference vectors in body reference frame.

According to TRIAD method, the rotation matrix from inertial reference frame to body reference frame holds:

$$
\begin{aligned}
{}_B\tilde{\boldsymbol{R}}_M &= \begin{bmatrix} \tilde{\boldsymbol{r}}_1 & \tilde{\boldsymbol{r}}_2 & \tilde{\boldsymbol{r}}_3 \end{bmatrix} \\
{}_I\hat{\boldsymbol{R}}_M &= \begin{bmatrix} \hat{\boldsymbol{r}}_1 & \hat{\boldsymbol{r}}_2 & \hat{\boldsymbol{r}}_3 \end{bmatrix}
\end{aligned}
$$

where:

$$\boldsymbol{r}_1 = \boldsymbol{n}_1$$

$$\boldsymbol{r}_2 = \frac{\boldsymbol{n}_1 \times \boldsymbol{n}_2}{\left\| \boldsymbol{n}_1 \times \boldsymbol{n}_2 \right\|}$$

$$\boldsymbol{r}_3 = \boldsymbol{n}_1 \times \frac{\boldsymbol{n}_1 \times \boldsymbol{n}_2}{\left\| \boldsymbol{n}_1 \times \boldsymbol{n}_2 \right\|}$$

Then the rotation matrix from inertial reference frame to body reference frame (attitude matrix) holds:

$${}_I\tilde{\boldsymbol{R}}_B = {}_I\hat{\boldsymbol{R}}_M \, {}_B\tilde{\boldsymbol{R}}_M^{\,T}$$

Considering:

$$_I\tilde{\boldsymbol{R}}_B = {}_I\boldsymbol{R}_B(\boldsymbol{I}+\boldsymbol{E})$$

being

$_I\boldsymbol{R}_B$: true value of the spacecraft attitude matrix;
$(\boldsymbol{I}+\boldsymbol{E})$: additional error matrix
$\boldsymbol{I}$: identity matrix

$$\boldsymbol{E} = [\boldsymbol{\alpha}\times] = \begin{bmatrix} 0 & -\psi & \theta \\ \psi & 0 & -\varphi \\ -\theta & \varphi & 0 \end{bmatrix}$$

$$\alpha = \begin{bmatrix} \varphi \\ \vartheta \\ \psi \end{bmatrix}$$

Determining the spacecraft attitude by TRIAD, the covariance matrix of the attitude error holds:

$$E\{\boldsymbol{\alpha}\boldsymbol{\alpha}^T\} = \sigma_1^2[\boldsymbol{I}] + \frac{1}{\|\hat{\boldsymbol{n}}_1 \times \hat{\boldsymbol{n}}_2\|^2}\left[(\sigma_2^2 - \sigma_1^2)\hat{\boldsymbol{n}}_1\hat{\boldsymbol{n}}_1^{\mathrm{T}} + \sigma_1^2(\hat{\boldsymbol{n}}_1\hat{\boldsymbol{n}}_2)(\hat{\boldsymbol{n}}_1\hat{\boldsymbol{n}}_2^{\mathrm{T}} + \hat{\boldsymbol{n}}_2\hat{\boldsymbol{n}}_1^{\mathrm{T}})\right]$$

where:

$$\sigma_1^2 = \sigma_{11}^2 + \sigma_{12}^2$$
$$\sigma_2^2 = \sigma_{21}^2 + \sigma_{22}^2$$

are the overall variance due to measured LOS (σ_{i1}) and expected one (σ_{i2}).

Before using the TRIAD methods, in order to have a correct use of estimated attitude, it is necessary to check the separation angle between unit vectors to limit the co-linearity errors.

In order to provide the better accuracy, due to the not symmetry in the algorithm (the attitude matrix is built using 1 as pivoting), it is necessary to assign the index 1 to the more accurate measurement ($\sigma_1^2 < \sigma_2^2$).

A preliminary assessment of the spin axis accuracy and its variation with respect satellite position, season (Sun elevation) has been done.

The Sun LOS determination accuracy (σ_1) depends on:

- Sun line of sight propagator accuracy;
- Sun sensor accuracy

The Sun LOS holds:

$$\hat{\boldsymbol{n}}_{LOS}(t)=\begin{bmatrix}-\cos(\omega+\upsilon(t))\cos(\Omega)+\sin(\omega+\upsilon(t))\sin(\Omega)\cos(i)\\ -\cos(\omega+\upsilon(t))\sin(\Omega)-\sin(\omega+\upsilon(t))\cos(\Omega)\cos(i)\\ -\sin(\omega+\upsilon(t))\sin(i)\end{bmatrix}$$

where:
Ω : longitude of the ascending node;
i : orbit inclination (angle between ecliptic plane and equatorial plane. At J2000.0 *i*=23° 26' 21");
ω : argument of periapsis;
$\upsilon(t)$: true anomaly at the epoch *t*.

The anomaly as function of the time can be computed by:

$$\upsilon(t)=2\,\mathrm{atan}\left(\sqrt{\frac{1+e}{1-e}}\tan\left(\frac{E(t)}{2}\right)\right)$$

where $E(t)$ is the eccentric anomaly at the epoch, and e is the eccentricity of the Earth orbit ($e=0.01673$). It can be computed solving the not-linear equation:

$$E(t)-e\sin(E(t))=n\left[t-t_0\right]$$

where
n : Earth mean motion (about 0.2 10^{-6} rad/s)

The use of the circular approximation (eccentricity equal to 0 and then $E(t)=n\left[t-t_0\right]$) leads to an error in Sun LOS determination of about 2°. This accuracy is considered not adequate for GG application. Considering the true eccentricity and stopping the solution of the not-linear equation at the first step, the error in Sun LOS can be reduced to 0.01°. The error on Earth initial state knowledge has been considered negligible.

So the following model will be used to compute the true anomaly:

$$M(t)=n\left[t-t_0\right]$$
$$E(t)=M(t)+e\sin(M(t))$$
$$\upsilon(t)=2\,\mathrm{atan}\left((1+e)\tan\left(\frac{E(t)}{2}\right)\right)$$

The on board time error with respect to the actual one introduces an additional negligible error.

The Sun sensor accuracy is provided in Table *** ([RD***]).

The Earth Magnetic Field LOS determination accuracy (σ_2) depends on:

- On-board Earth Magnetic Field model accuracy;
- On-board orbit propagator accuracy;
- EMF measurement accuracy.

The on-board EMF model accuracy is mainly related to its truncation error. The results reported in Table 6-1 come from a study that has been done for GOCE spacecraft, for a polar orbit. They may be considered representative of the GG scenario though a specific analysis shall be re-executed in the early phase of Phase-B. Results show that to limit such an error to 0.1÷0.2deg, the on-board model order shall be greater than 10÷12.

Model order	Maximum observed error	Maximum angular error	Error standard deviation
2	4.0 μT (13%)	7.6°	2.7°
4	2.6 μT (8.7%)	5.0°	1.8°
6	0.85 μT (2.7%)	1.6°	0.5°
8	0.24 μT (0.8%)	0.46°	0.15°

Table 6-1 - Truncation errors for different EMF model order (MAG95 11th as truth model, GOCE altitude 250km, orbit inclination 96.4deg)

In order to address the effect of spacecraft position error on the determination of local magnetic field, a simple dipole model for the Earth Magnetic field has been considered. On this assumption, the magnetic field has a rotational symmetry and only variations on latitude are significant.

Fixing:

$\boldsymbol{r}$: is the position vector of spacecraft ($r = \|\boldsymbol{r}\|\,; \hat{\boldsymbol{r}} = \frac{\boldsymbol{r}}{r}$);

$\hat{v}$: is the unit vector associated to the magnetic dipole;

then the magnetic field vector of the Earth in $\boldsymbol{r}$ holds:

$$\boldsymbol{B} = \boldsymbol{B}_O\left[3\left(\hat{v}\cdot\hat{\boldsymbol{r}}\right)\hat{\boldsymbol{r}} - \hat{v}\right]$$

$$\boldsymbol{B}_O = \frac{\mu_E}{r^3}$$

The expected Earth Magnetic field versor is:

$$\hat{\boldsymbol{n}}_H = \frac{3\left(\hat{v}\cdot\hat{\boldsymbol{r}}\right)\hat{\boldsymbol{r}} - \hat{v}}{\left\|3\left(\hat{v}\cdot\hat{\boldsymbol{r}}\right)\hat{\boldsymbol{r}} - \hat{v}\right\|}$$

Error on spacecraft altitude is not significant due to normalized use of magnetic field. Errors on spacecraft true anomaly, orbit inclination, ascending node, etc. give rise to an error on expected magnetic field direction indicated by $\delta\hat{\boldsymbol{n}}_H$.

$$\left\|\delta\hat{\boldsymbol{n}}_H\right\| = S\begin{bmatrix} d\alpha_{AT} \\ d\alpha_{CT} \end{bmatrix}\frac{1}{r} \le \bar{\sigma}_S\begin{bmatrix} d\alpha_{AT} \\ d\alpha_{CT} \end{bmatrix}$$

where:

$d\alpha_{AT}$: along-track angular error

$d\alpha_{CT}$: cross-track error

S : sensitivity matrix

$\overline{\sigma}_S$: higher singular value of the sensitivity matrix S ($\overline{\sigma}_S \cong 1.2$)

Data in Table 6-2 link the error magnitude on spacecraft position with the error on direction of the local magnetic field. The same data permit to derive also the impact on the local magnetic field direction determination due to on-board time error (1s corresponds to an along track angle error equals to 0.06deg, i.e. 0.072deg on the magnetic field).

In order to have an error on Earth magnetic field due two spacecraft orbit propagator lower than the Earth magnetic field model, the not radial position of the spacecraft must be available with accuracy better than 10km.

Error on EMF [deg]	Along and across position error [deg]	Position error @600km [km]
1	0.83	100
0.10	0.083	10
0.01	0.0083	1
0.001	0.00083	0.1

Table 6-2 - Error on direction of Earth magnetic due two orbit propagator position error

The required position error is not a critical value to be met on a time horizon of 12÷24h, thank to the almost equatorial orbit and low drag. In any case, during Phase B detailed analysis on expected accuracy versus model complexity and versus updating frequency of the orbit propagator state vector.

EMF measurement accuracy depends on:

- Magnetometer accuracy (scale factor error, orthogonality, sensor bias and random error);
- Coupling between MGM and platform additional dipoles, due to electronic equipment, tanks, etc.

Usually, the first contributors are very little (see Table 11-4) and major errors come from the coupling with on-board equipment and devices.

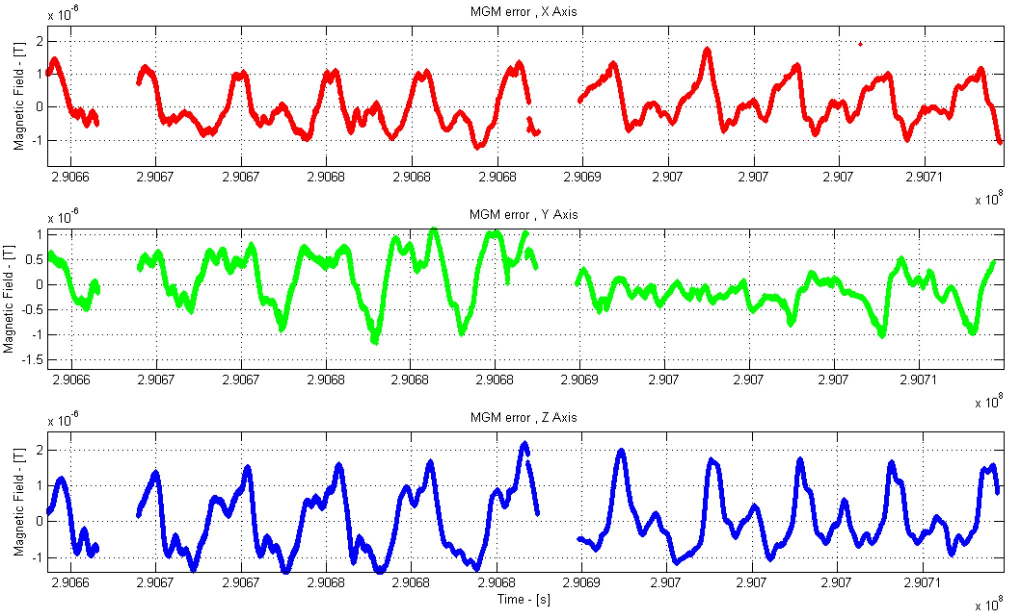

Figure 6-1 – Differences between measured EMF (as provided by magnetometer before in-flight calibration) and expected one (computed using GPS receiver, star-tracker, EMF model up to 7th order).

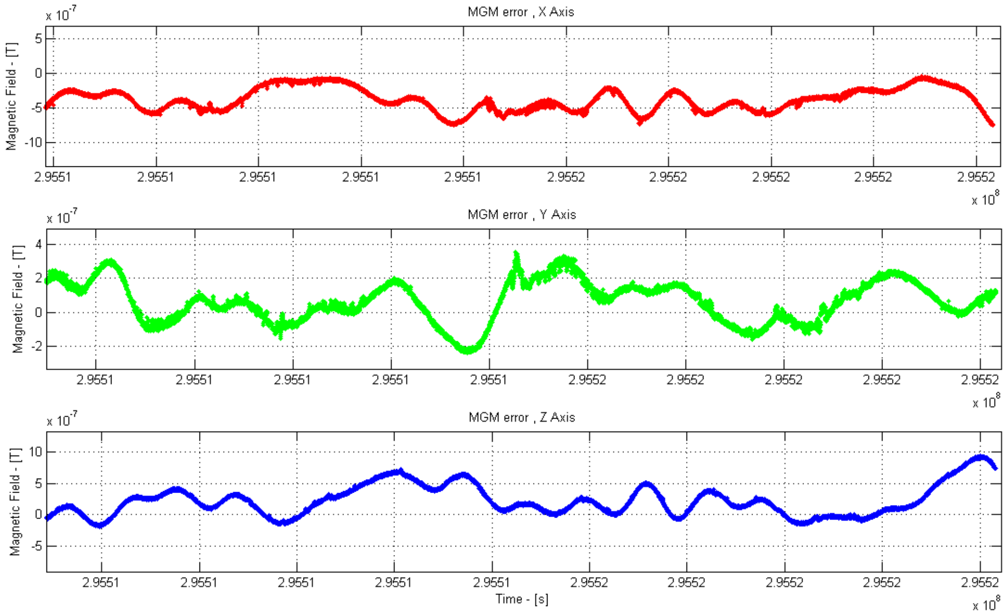

Figure 6-2 – Differences between measured EMF (as provided by magnetometer after in-flight calibration) and expected one (computed using GPS receiver, star-tracker, EMF model up to 7th order).

In order to permit high accuracy by magnetometer, it will necessary to mount properly such equipment inside the spacecraft, i.e. as far as possible from time varying dipoles. Moreover, specific on-ground calibration procedure based on flight-data shall be considered.

Several calibration algorithms are proposed by literature; they are organized as (see [RD 14], [RD 15], [RD 16]):

- Attitude-independent Three-Axis Magnetometer (TAM) calibration methods;
- Attitude-dependent Three-Axis Magnetometer (TAM) calibration methods.

First type methods permit to determine the biases, scale factor and the non-orthogonal part of the alignment (a measure of the skewness of the three axes). When data from other sensors are available, the orthogonal misalignment can be determined relative to those other sensors (second type of methods). An integrate procedure shall be foreseen for GG applications based on accurate Sun sensor.

In order to show the effectiveness of such a calibration, actual flight-data provided by GOCE mission are shown in Figure 6-1 and Figure 6-2. Actual measurements provided by MGM have been compared with the expected EMF taking into account the spacecraft position (provided by GPS receiver), attitude (from star-tracker) and EMF model truncated at 7th order. Figure 6-1 shows measurement errors with magnitude about 2.5μT, which reduce to 1μT (see Figure 6-2) after calibration (the equivalent angle error is in the range 0.9÷1.9deg). Better results (0.5÷1 deg, see [RD 14]) may be achieved considering a satellite design oriented to a fine EMF measurement (not required by GOCE mission).

The accuracies provided in Table 6-3 have been used to assess the expected accuracy of the attitude measurement based on magnetometer and fine Sun sensor according to TRIAD method,

		Error	Overall error
Smart Sun Sensor (from Selex GA)			
	Equipment	0.02°	
	Sun propagator	0.01°	
	Mounting error	0.015°	
			0.045°
Three axis magnetometer			
	Equipment after calibration	0.5°	
	EMF model and orbit propagator	0.5°	
	Mounting error	0.015°	
			1.015°

Table 6-3 – Error budget for the overall accuracy to be used for TRIAD covariance analysis.

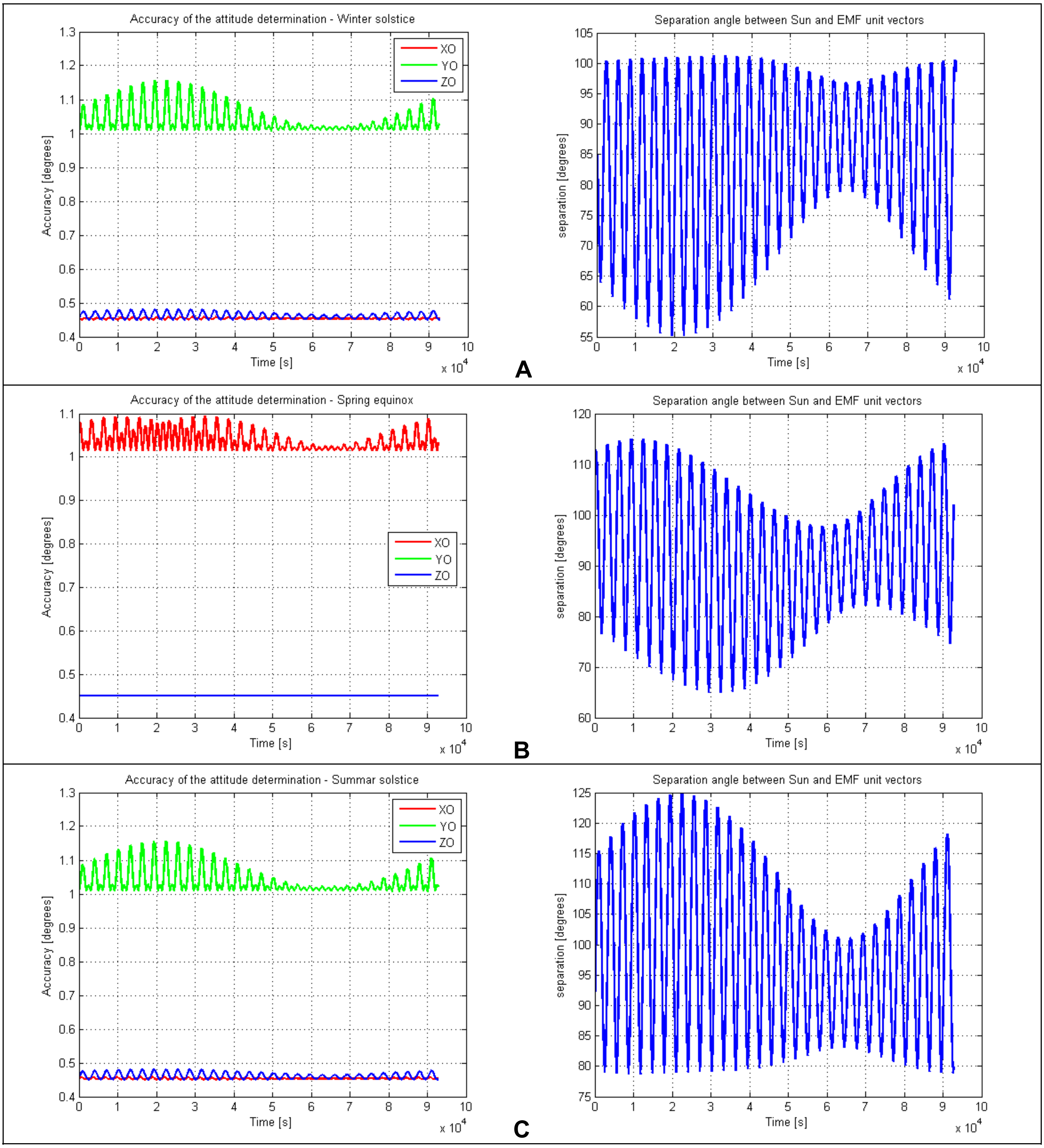

Figure 6-3 – Expected attitude determination accuracy during one day at winter solstice (A), spring equinox (B) and summer solstice (C).

It has been considerate a simplified model for the EMF (dipole), and three relative orientation of the Sun with respect to the orbital reference frame have been considered (Winder solstice, Spring equinox and Summer solstice). Accuracy is provided in Figure 6-3.

6.5 Reaction control system

The present chapter describes the reaction control system. It will be used for:

- detumbling after separation from the launcher;
- satellite spin-up.

It will consist of two branches of 4 thrusters each one. Figure 6-4 shows the layout of the proposed assembly.

Preliminarily, it should be possible to consider on/off thrusters with force in the range 0.3-0.5 N, with MIB < 0.005 Ns (TBC). A possible solution may be based on the Small GEO Cold Gas Propulsion in development by TAS-I (Firenze) ([RD 13]).

Small GEO is general purpose small geostationary satellite platform supporting up to 300 kg payload mass, payload power of up to 3 kW and a lifetime of up to 15 years. The cold-gas thrusters are used for de-tumbling (after separation from the launch vehicle) and momentum management (in Safe Mode).

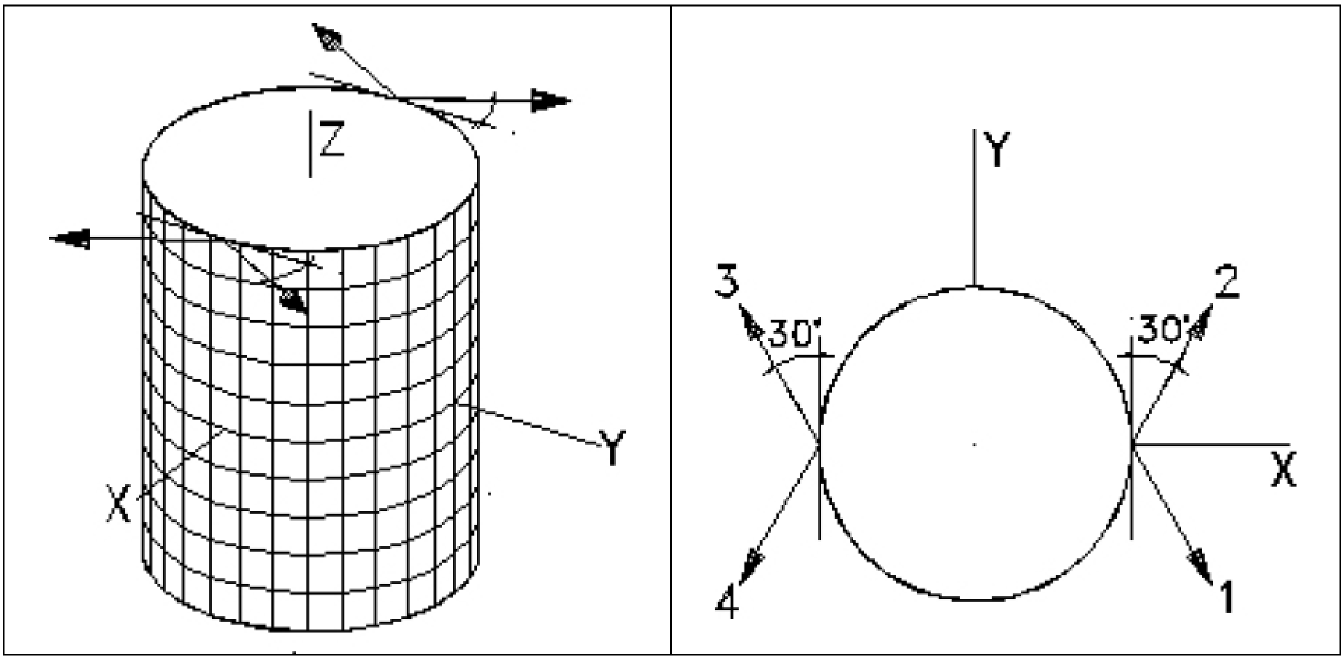

Figure 6-4 – Layout of the cold-gas thrusters

The applied torque is related to each force commanded to each thruster by the formula:

$\boldsymbol{T} = \boldsymbol{B}_t\, \boldsymbol{u}$

where:

$\boldsymbol{T}$: torque;

$\boldsymbol{B}_t$: thrusters assembly matrix;

$\boldsymbol{u}$: force applied by each thrusters.

Considering the actual satellite geometry (radius ≈ 0.75m, height ≈ 1.4m), and the layout provided above, the thrusters assembly matrix becomes:

$$\boldsymbol{B}_t = \begin{matrix} -0.5196 & 0.5196 & -0.5196 & 0.5196 \\ 0.3000 & 0.3000 & -0.3000 & -0.3000 \\ -0.5629 & 0.5629 & 0.5629 & -0.5629 \end{matrix}$$

Considering such a matrix, taking into account the worst separation conditions (three-axis stabilized attitude), a commissioning time of 2 weeks, and the final satellite spin rate, a preliminary propellant budget has been computed: considering specific impulse equals to 60s, the foreseen propellant mass is 9.5kg.

7. EXPERIMENT AND MISSION REQUIREMENT RELEVANT FOR ATTITUDE AND DRAG FREE CONTROL DESIGN

7.1 Driver requirements

The following functional requirements drives the attitude and drag-free control design:

- dumping of the residual angular rate after separation, Sun acquisition and spin-up of the spacecraft;
- absolute pointing error (APE) of the spin axis (< 2÷3 deg, half-cone, 99% confidence level);
- magnitude of the angular rate around the spinning axis (360 deg/s, ±10%);
- rejection of overall environmental perturbation at spin frequency (space environmental and spacecraft induced disturbances). It is required to recover the EP violation (up to 8.37 10^{-17} m/s^2)[4]
- maintaining the relative position and rotation magnitudes between spacecraft and PGB well below the bounds for PGB suspension integrity, and dynamic range of the sensors. It means that the linear displacement between PGB COM and spacecraft COM shall be lower than 0.15mm (TBC), and that the angular displacement shall be lower than 0.1 rad (see [AD1], TBC).

7.2 From scientific requirement to DFC requirement

7.2.1 XY plane

In order to derive the major DFM requirements, it is necessary to introduce several assumptions related to the approach that will be followed to detect and estimate the Equivalence Principle violation, taking into account the payload characteristics.

Let be:

T : the interval of observation;

Δf : frequency resolution,

---

[4] This value is related to the GG goal to test the EP to 1 part in 10^{17} by the relation:

$$a_{EP} = \eta \frac{GM_E}{(R_E + h)^2} = 10^{-17} g(h)$$

$$\cong 8.37\,10^{-17}\, m/s^2 \quad @h = 500km$$

$$\cong 8.13\,10^{-17}\, m/s^2 \quad @h = 600km$$

$$\cong 7.90\,10^{-17}\, m/s^2 \quad @h = 700km$$

$$\Delta f = \frac{1}{T}$$

A : amplitude of the proof masses differential acceleration due to the EP violation that it is necessary to detect in reliable way (8.37 10-17 m/s^2);

D : amplitude of the proof masses differential displacement due to the EP violation that it is necessary to detect in reliable way;

δD : residual of all other environmental harmonic disturbances (space environment and spacecraft) at spinning rate;

$\hat{D}$: estimated amplitude of the EP violation that it is necessary to detect in reliable way;

N : spectral density of the overall environmental disturbances noise (space environment and spacecraft, capacitors measurement noise) affecting the EP violation measurement,

χ_{CMRR} : balance displacement common mode rejection ratio (CMRR) rejection in XY spacecraft axes

χ_{DFC} : drag-free displacement rejection on XY spacecraft axes

N_T : thrusters force noise spectral density (N/√Hz) around spin rate

N_{MDF} : spectral density of the measurement error of the relative position between PGB and spacecraft (m/√Hz) around spin rate

N_{MS} : spectral density of the measurement of the relative position variation between the test masses

α_1 , α_2 : apportionment coefficients

β_1 , β_2 , β_3 : apportionment coefficients

Without loss in the generality, it has been considered that the detection of the EP violation will be based on the computation of the spectrum of the signal acquired by PGB capacitors in real time. The use of other approaches like Maximum likelihood provides the same conclusions.

The estimated amplitude of the EP violation is affected by residual of environmental disturbances and measurement:

$$\hat{D} = \sqrt{D^2 + \delta D^2 + 2N^2 \Delta f}$$

$$\hat{D} = D\sqrt{1 + \left(\frac{\delta D}{D}\right)^2 + \frac{2N^2 \Delta f}{D^2}}$$

The amplitude of the proof masses displacement is related to the acceleration induced by EP violation according to the relation:

$$D = \frac{A}{(\omega_{dm})^2}$$

$$\omega_{dm} = \frac{2\pi}{T_{dm}}$$

D is as much lower as ω_{dm} is higher and as T_{dm} is lower.

Since it shall be $\frac{2N^2\Delta f}{D^2} << 1$ and $\left(\frac{\delta D}{D}\right)^2 << 1$, a first order approximation may be considered:

$$\hat{D} \cong D\left(1 + \frac{1}{2}\left(\frac{\delta D}{D}\right)^2 + \left(\frac{N^2\Delta f}{D^2}\right)\right)$$

$$\frac{\hat{D}}{D} \cong 1 + \frac{1}{2}\left(\frac{\delta D}{D}\right)^2 + \frac{N^2}{D^2T}$$

$$\frac{\hat{D} - D}{D} = \frac{\Delta D}{D} \cong \frac{1}{2}\left(\frac{\delta D}{D}\right)^2 + \frac{N^2}{D^2T}$$

From above formulas, each error contributors shall be a fraction of the allowed relative error. Let α_1 and α_2 be these fractions. The following formulas read:

$$\frac{1}{2}\left(\frac{\delta D}{D}\right)^2 \le \alpha_1^2 \frac{\Delta D}{D}$$

$$\frac{N^2}{D^2T} \le \alpha_2^2 \frac{\Delta D}{D}$$

$$\alpha_1^2 + \alpha_2^2 \le 1$$

The upper bounds for harmonic and random disturbances at and around spinning frequency shall be such that:

$$\delta D \le D\sqrt{2\alpha_1^2 \frac{\Delta D}{D}}$$

$$N \cong D\sqrt{T\alpha_2^2 \frac{\Delta D}{D}}$$

δD results from:

- Residual drag and solar pressure compensation left by drag-free controller and balance CMRR rejection;
- Residual harmonic disturbance at spinning rate introduced by the spacecraft (e.g. thrusters mechanical noise due to open/close of valves if any, etc.) and left by drag-free controller and balance displacement common mode rejection ratio (CMRR) rejections.

$$\chi_{CMRR}\,\chi_{DFM}\frac{(a_D + a_T)}{(\omega_{dm})^2} \le \delta D$$

N depends on:

- displacement measurement noise (electronic chain, ADC quantization, etc.);
- residual effects of drag-free control :
    - residual effects after CMRR rejection and DFC rejection of thrusters noise;
    - residual effects after CMRR rejection and DFC rejection of thrusters resolution.

Then

$$\sqrt{(\chi_{CMRR}N_{DFM})^2 + N_{MS}^2} \le N$$

where

$$(\chi_{CMRR}N_{DFM})^2 = \left(\chi_{CMRR}\chi_{DFM}\frac{1}{(\omega_{dm})^2}\frac{N_T}{m_S}\right)^2 + (\chi_{CMRR}N_{MDF})^2$$

The random error shall be

$$\sqrt{\left(\chi_{CMRR}\,\chi_{DFM}\frac{1}{(\omega_{dm})^2}\frac{N_T}{m_S}\right)^2 + (\chi_{CMRR}N_{MDF})^2 + N_{MS}^2} \le N$$

$$\chi_{CMRR}\,\chi_{DFM}\frac{1}{(\omega_{dm})^2}\frac{N_T}{m_S} \le \beta_1 N$$

$$\chi_{CMRR}N_{MDF} \le \beta_2 N$$

$$N_{MS} \le \beta_3 N$$

$$\beta_1^2 + \beta_2^2 + \beta_3^2 \le 1$$

Considering the balance characteristics and the apportionment rules provided in Table 7-1, it is possible to derive:

$$\chi_{DFM} < 2.4\,10^{-5}$$
$$N_{MS} \le 0.5\,10^{-12}\ \mathrm{m}/\sqrt{Hz}$$
$$N_{MDF} \le 0.5\,10^{-6}\ \mathrm{m}/\sqrt{Hz}$$
$$N_T \le 0.06\,\mathrm{N}/\sqrt{Hz}$$

The maximum thruster's noise shall also be compatible with the requirement on gap between PGB and spacecraft (0.15mm). The spectral density of the thrusters noise shall be:

$$N_T \leq \frac{\sqrt{2\pi}\, d_{PGB\_SP}\, \omega_O^{3/2} m_S}{\sqrt{p}} \quad \mathrm{N}/\sqrt{Hz}$$

where:

d_{PGB_SP} : standard deviation of the allowed displacement

p : multiple of the suspension bandwidth (p>2)

$$N_T \leq \quad 120\,\mu\mathrm{N}/\sqrt{Hz}\ \left(p = 4,\ m_S = 400kg\right)$$

Table 7-1 – Parameter considered for DFM requirement derivation at 2Hz spin rate

No	Parameter	Symbol	Unit	Value	Comments
1	Minimum observable differential acceleration due to the EP violation	A	m/s^2	8.37 10^{-17}	
2	Balance differential period	T_{dm}	s	$\geq$ 500[5]	The lower admissible value shall be considered
3	Balance differential angular frequency		rad/s	0.0126	
4	Proof masses differential displacement due to the minimum observable EP violation	D	m	0.53 10^{-12}	
5	Maximum allowed relative uncertainty acceptable in the EP violation detection	$\Delta D / D$		0.3	TBC
6	Maximum perturbing environmental force	a_D	m/s^2	$\leq$ 0.2 10^{-6}	
7	Maximum perturbing spacecraft force	a_T	m/s^2	$\leq$ 0.02 10^{-6}	
8	Apportionment coefficient	α_1		0.7071	
9	Apportionment coefficient	α_2		0.7071	
10	Apportionment coefficient	β_1		0.07053	
11	Apportionment coefficient	β_2		0.07053	
12	Apportionment coefficient	β_3		0.00705	
13	PGB-spacecraft	d_{PGB_SP}	m	30 10^{-6}	

---

[5] The GGG experimental results show the differential period greater than 536s.

	displacement variation due to overall thrusters noise				

7.2.2 *Z spin axis*

The movement of the test-masses along Z direction, due to coupling with gravity gradient, introduces an additional differential acceleration in the plane XY that is not separable with respect to the EP violation.

The acceleration along Z axis is due to the fact that the satellite spin-axis is not orthogonal to the orbital plane. In preliminary way, for requirement derivation the assumed worst case value of the tilt angle is 10deg (about 5deg is the orbit plane inclination, 5deg as very conservative maximum spin-axis de-pointing). At 10deg, the maximum expected magnitude for the acceleration along Z axis is equal to 3.4 10^{-8} m/s^2.

According to [RD 10], the relation between the acceleration along Z axis and the differential one in XY plane is about:

$$A_Z = \frac{A_{XY}}{\left(2\;10^{-6}\right)\chi_{DFM\_Z}\;\chi_{CMRR\_Z}}$$

The same relation is applicable to the displacement:

$$D_Z = \frac{D_{XY}}{\left(2\;10^{-6}\right)\chi_{DFM\_Z}\;\chi_{CMRR\_Z}}$$

Considering:

- The maximum allowed acceleration A_{XY} due to the Z-axis movement and coupling with gravity gradient not greater than 5 10^{-10} m/s^2;
- χ_{CMRR_Z} < 0.02;
- The magnitude of the acceleration along Z axis A_Z < 4 10^{-8} m/s^2

then χ_{DFM_Z} shall be not greater than 1/200.

Starting from the apportionment for the random error considered for XY plane, but considering the effect of random error lower than 1/10 of the measurement error (negligible), it is possible to derive:

$$D_Z = \frac{0.05\,10^{-12}\ \mathrm{m}/\sqrt{Hz}}{\left(2\;10^{-6}\right)\;2\,10^{-2}} < 1.25\;\;10^{-6}\,\mathrm{m}/\sqrt{Hz}$$

8. DRAG COMPENSATION CONTROL

8.1 The model of the plant

The model to be considered for the control design (control law, equipment requirement specification) starts from the following assumptions:

- the spacecraft is a rigid body;
- the PGB is a rigid body;
- coupling between spacecraft and PGB is provided by suspension.

Let be:

x, y, z : the coordinates of the PGB COM with respect to the spacecraft COM;
m_S : the spacecraft mass
m_{PGB} : the PGB mass
m_r : the reduced mass

$$m_r = \frac{m_S\, m_{PGB}}{m_S + m_{PGB}}$$

F_P : perturbing force (drag, solar pressure, thruster's noise)
F_T : thruster assembly control force
F_C : capacitors' control force
Q : quality factor of the PGB suspension
ω_S : spacecraft spin rate
ω_0 : natural frequency of the suspension

The following differential equations describe the dynamics of the PGB-spacecraft COMs relative motion with respect to an inertial observer positioned at the orbital reference frame at the init time:

$$\ddot{x} = -\omega_0^2 x - \left(\frac{\omega_0^2}{Q\omega_S}\right)\dot{x} + \left(\frac{\omega_0^2}{Q\omega_S}\right)\omega_S y - \frac{F_{PX} + F_{TX}}{m_S} - \frac{F_{CX}}{m_r}$$

$$\ddot{y} = -\omega_0^2 y - \left(\frac{\omega_0^2}{Q\omega_S}\right)\dot{y} - \left(\frac{\omega_0^2}{Q\omega_S}\right)\omega_S x - \frac{F_{PY} + F_{TY}}{m_S} - \frac{F_{CY}}{m_r}$$

$$\ddot{z} = -\omega_0^2 z - \left(\frac{\omega_0^2}{Q\omega_S}\right)\dot{z} - \frac{F_{PZ} + F_{TZ}}{m_S} - \frac{F_{CZ}}{m_r}$$

The model shows coupling between the movements on the XY plane, while the movement on z axis is independent. The coupling occurs by the parameter $\left(\frac{\omega_0^2}{Q\omega_S}\right)\omega_S$ that is equal to about $2\ 10^{-5}$ (weak coupling) (see Table 14-1).

The poles of the 4th order system describing the dynamics on XY plane are:

$$p_{1,2} = -0.000234 \pm j0.0419 = -0.000234 \pm j\omega_0$$

$$p_{3,4} = 0.000231 \pm j0.0419 = 0.000231 \pm j\omega_0$$

The poles of the 2nd order system describing the dynamics along Z-axis are:

$$p_{5,6} = -1.551\ 10^{-6} \pm j0.0419 = -1.551\ 10^{-6} \pm j\omega_0$$

Without any external control action the movement on the plane X-Y is unstable. Figure 8-1 shows the magnitude of the transfer function between the force applied in X axis (Y axis) and the movement along X (along Y).

The following equations describe the dynamics of the PGB-spacecraft COMs relative motion with respect to an observer fixed with the spacecraft body frame:

$$\ddot{x} = -\left(\omega_0^2 - \omega_S^2\right)x - \left(\frac{\omega_0^2}{Q\omega_S}\right)\dot{x} + 2\omega_S\dot{y} - \frac{F_{PX} + F_{TX}}{m_S} - \frac{F_{CX}}{m_r}$$

$$\ddot{y} = -\left(\omega_0^2 - \omega_S^2\right)y - \left(\frac{\omega_0^2}{Q\omega_S}\right)\dot{y} - 2\omega_S\dot{x} - \frac{F_{PY} + F_{TY}}{m_S} - \frac{F_{CY}}{m_r}$$

$$\ddot{z} = -\omega_0^2 z - \left(\frac{\omega_0^2}{Q\omega_S}\right)\dot{z} - \frac{F_{PZ} + F_{TZ}}{m_S} - \frac{F_{CZ}}{m_r}$$

As in previous reference frame, the model shows coupling between the movements on the X and Y, while the movement on Z axis is independent. The coupling occurs by the parameter $2\omega_S$ that is equal to about 12.6 (strong coupling).

The poles of the 4th order system describing the dynamics on XY plane are:

$$p_{1,2} = -0.000234 \pm j6.3251 = -0.000234 \pm j\left(\omega_S + \omega_0\right)$$

$$p_{3,4} = 0.000231 \pm j6.2413 = -0.000231 \pm j\left(\omega_S - \omega_0\right)$$

The poles of the 2nd order system describing the dynamics along Z-axis are (same for inertial reference frame):

$$p_{5,6} = -1.551\ 10^{-6} \pm j0.0419 = -1.551\ 10^{-6} \pm j\omega_0$$

Without any external control action the whirl motion is unstable. The stabilization of whirl motion can be implemented by building in a rotating frame a damping command proportional to the relative velocity between bodies in the inertial (non-rotating) reference frame. A simple way to show this capability is by examining the problem of 2 bodies connected by a dissipative spring.

The stabilization of the whirl control is achieved introducing a dumping β_W proportional to the inertial rate:

$$\ddot{x} = -\left(\omega_0^2 - \omega_S^2\right)x - \left(\frac{\omega_0^2}{Q\omega_S} + \frac{\beta_W}{m_r}\right)\dot{x} + 2\omega_S\dot{y} + \frac{\beta_W}{m_r}\omega_S y - \frac{F_{PX} + F_{CX}}{m_S}$$

$$\ddot{y} = -\left(\omega_0^2 - \omega_S^2\right)y - \left(\frac{\omega_0^2}{Q\omega_S} + \frac{\beta_W}{m_r}\right)\dot{y} - 2\omega_S\dot{x} - \frac{\beta_W}{m_r}\omega_S x - \frac{F_{PY} + F_{CY}}{m_S}$$

$$\ddot{z} = -\omega_0^2 z - \left(\frac{\omega_0^2}{Q\omega_S}\right)\dot{z} - \frac{F_{PZ} + F_{CZ}}{m_S}$$

The stabilization (all poles with real part equal to zero or negative) is achieved for β_W equals to the critical damping, that is:

$$\beta_{W\_CR} = \frac{\omega_0}{Q}$$

The poles of the system are:

- $-0.0005 \pm j6.32509 = -0.0005 \pm j(6.28319 + 0.0419)$
- $0.0000 \pm j6.24129 = 0.0000 \pm j(6.28319 - 0.0419)$

If $\beta_W = 10\frac{\omega_0}{Q}$, the poles are (all poles have real part less then zero):

- $-0.0026 \pm j6.32509 = -0.0026 \pm j(6.28319 + 0.0419)$
- $-0.0021 \pm j6.24129 = -0.0021 \pm j(6.28319 - 0.0419)$

Figure 8-2 shows the magnitude of the transfer function between the force applied in X axis (Y axis) and the movement along X axis (Y axis). Figure 8-3 provides a zoom around spin rate (1 Hz) of the magnitude of the above transfer function: it is possible to recognize the effect of frequency shift of the suspension transfer function due to spacecraft and PGB spin rate. The disturbances at spinning frequency are not attenuated by the PGB suspension (natural frequency around 6.7 mHz). This is the reason why so fine drag compensation is required to the drag-free controller: drag is not attenuated by the PGB suspension but only by CMRR of the balance connecting the proof masses.

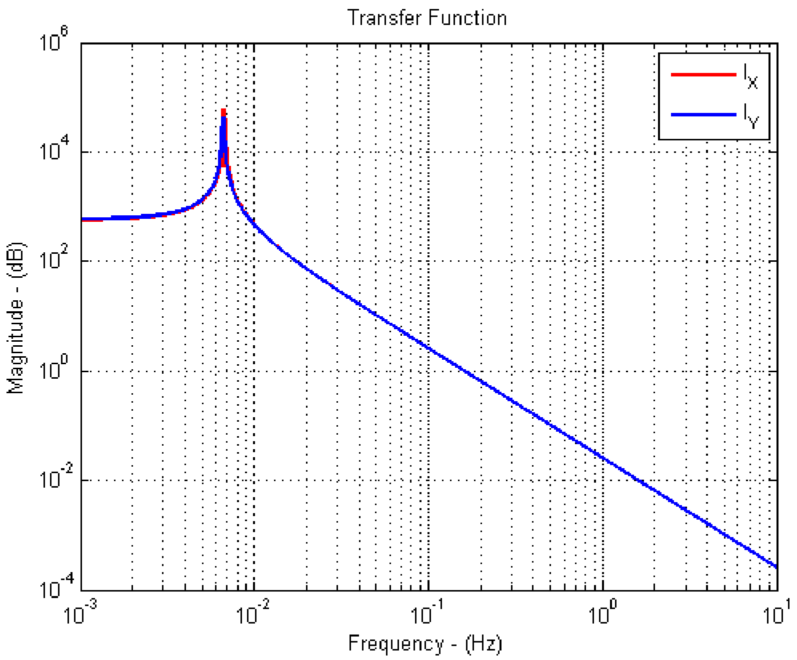

Figure 8-1 - Magnitude of the transfer functions between X force and X displacement (red), Y force and Y displacement (blu) in Inertial reference frame.

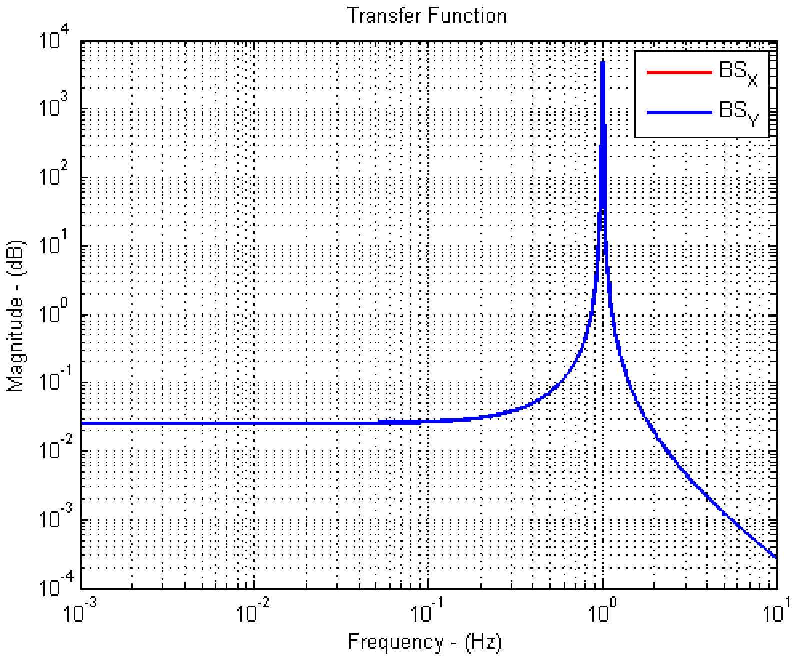

Figure 8-2 - Magnitude of the transfer functions between X force and X displacement (red), Y force and Y displacement (blu) in Body reference frame.

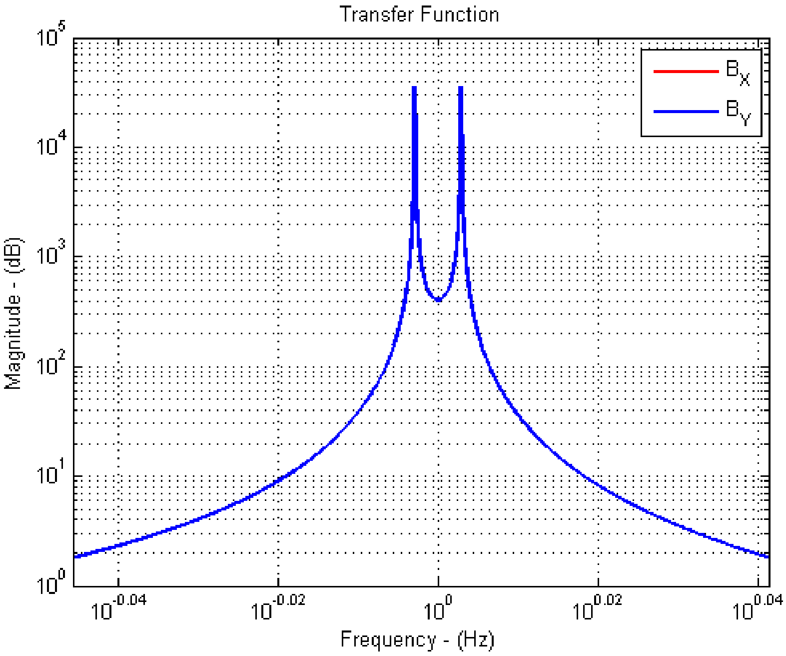

Figure 8-3 - Zoom around 1 Hz of the magnitude of the transfer functions between X force and X displacement (red), Y force and Y displacement (blu) in Body reference frame.

8.2 Architecture and algorithms for the drag compensation

According to previous analysis, the designed controller has in charge:

- the stabilization of the relative displacement in the plane XY, limiting the magnitude;
- the rejection of any disturbances (drag is the expected major one, but others are solar pressure, thrusters noise, etc.) at spinning rate (1Hz) on overall axis;
- the stabilization of the spin rate versus variation of the spacecraft inertia moment due to thermo-elastic deformations. It is necessary to preserve the integrity of the suspension and sensors.

The controller has been organized according to the architecture provided in **Error! Reference source not found.**.

There are three independent controllers:

- *XY drag-free controller* for drag compensation on the XY plane. The controller shall reduce the drag disturbances at spinning rate providing a rejection lower than 2 10^{-5};
- *XY whirl controller* for the stabilization of the movement in the plane XY. The controller shall stabilize the movement introducing a low-frequency action.
- *Z drag-free controller* for drag compensation and displacement reduction along Z axis.
- *Spin-axis angular rate controller*, to limit the relative rotation between PGB and satellite for suspension integrity.

XY drag-free controller is feed by measurement on relative XY displacement between PGB and spacecraft COM provided by capacitors sensors. The fine compensation occurs thank to micro-thrusters assembly.

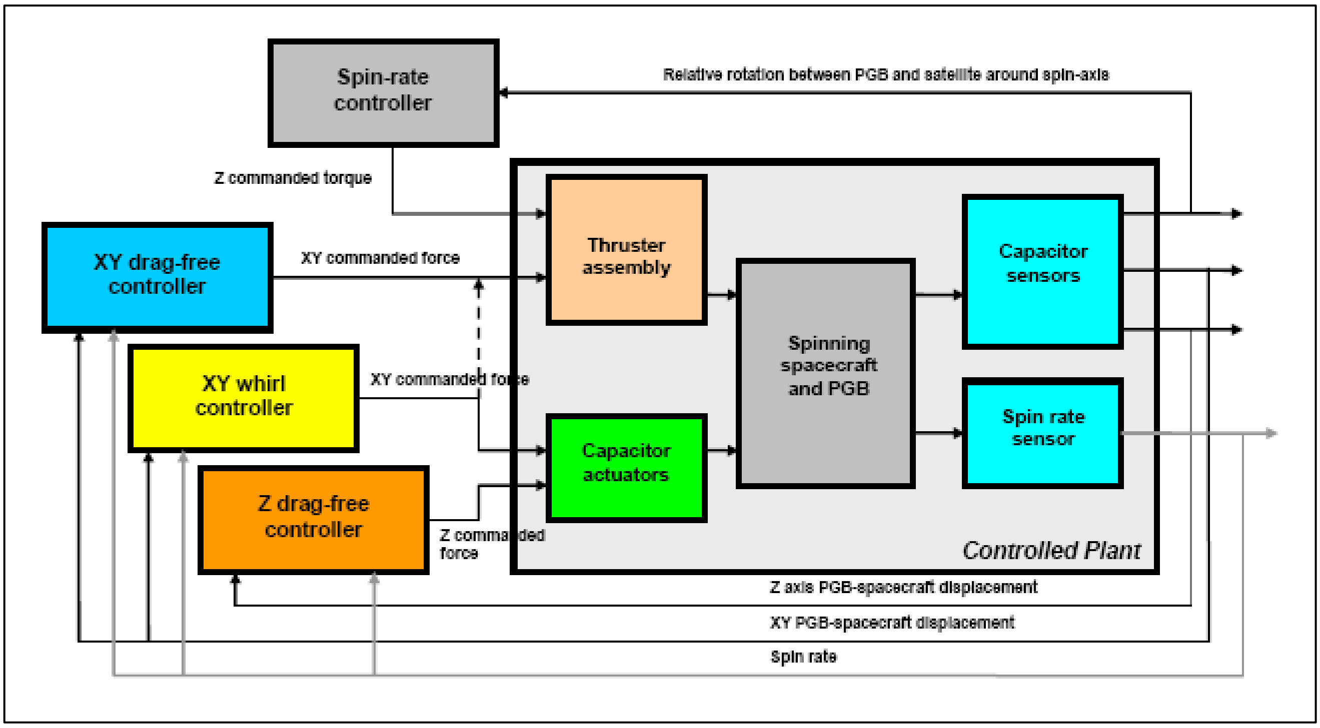

Figure 8-4 – Linear axis control architecture

XY drag-free controller is feed by measurement on relative XY displacement between PGB and spacecraft COM provided by capacitors sensors. The fine compensation occurs thank to micro-thrusters assembly.

Also XY whirl controller is feed by measurement on relative XY displacement between PGB and spacecraft COM as for XY drag-free controller, and the actuation is realized by capacitors (out from DFM, when PGB is released by mechanism and micro-thrusters assembly disabled) and/or micro-thrusters assembly (during DFM, as alternative).

Z drag-free controller is feed by measurement on relative displacement along Z axis between PGB and spacecraft COM provided by capacitors sensors. Actuation is realized always by capacitors.

The spin-rate controller is driven by measurement on relative rotation around Z axis between PGB and spacecraft provided by capacitor sensors. Actuation is realized thrusters.

XY drag-free controller is the most challenging one considering the required very fine drag compensation and the limitations on the response time of the available actuators that reduces the useful command update rate. Two control design approaches have been envisaged for it:

- controller designed directly in body reference frame (see Figure 8-5);

- controller designed in the inertial reference frame (see Figure 8-6):
  - The controller commands the required force in an inertial reference frame;
  - The actual thrusters commands (in body reference frame) are computed by modulation starting from above commanded force ;
  - The acquired measurements (in body reference frame) are reported in body reference frame by de-modulation.

The above approaches are equivalent for what concern the thruster’s requirements and the performances. Both solutions need the estimated spacecraft orbital and spin rates in order to provide required rejection. For the spin rate measurement, specific equipment has been considered (see chapter 10)

The first solution in principle is the better one since the “natural one”. It permits to work directly in the body reference frame where the measurements are available and the commands shall be provided. At the same time, using the body reference frame, the observer (see next in the chapter) may be shared between XY drag-free controller and XY whirl controller. As drawback, the plant model envisages strong coupling between X and Y axes requiring higher measurement sampling frequency and greater care shall be put building the discrete model.

Using instead the inertial reference frame, the coupling between X and Y axes is weak and numerical problem are simpler to be managed. The draw-backs are in the necessity to introduce demodulation and modulation schemes at spinning rate. This solution has been selected.

XY drag-free controller and XY whirl controller are Multi Input Multi Output (MIMO) controller, and Z drag-free controller is a Single Input Single Output (SISO) controller.

All controllers have been designed according to the state variable approach building four lower level functions:

- state variable observer;
- control law;
- command distribution.

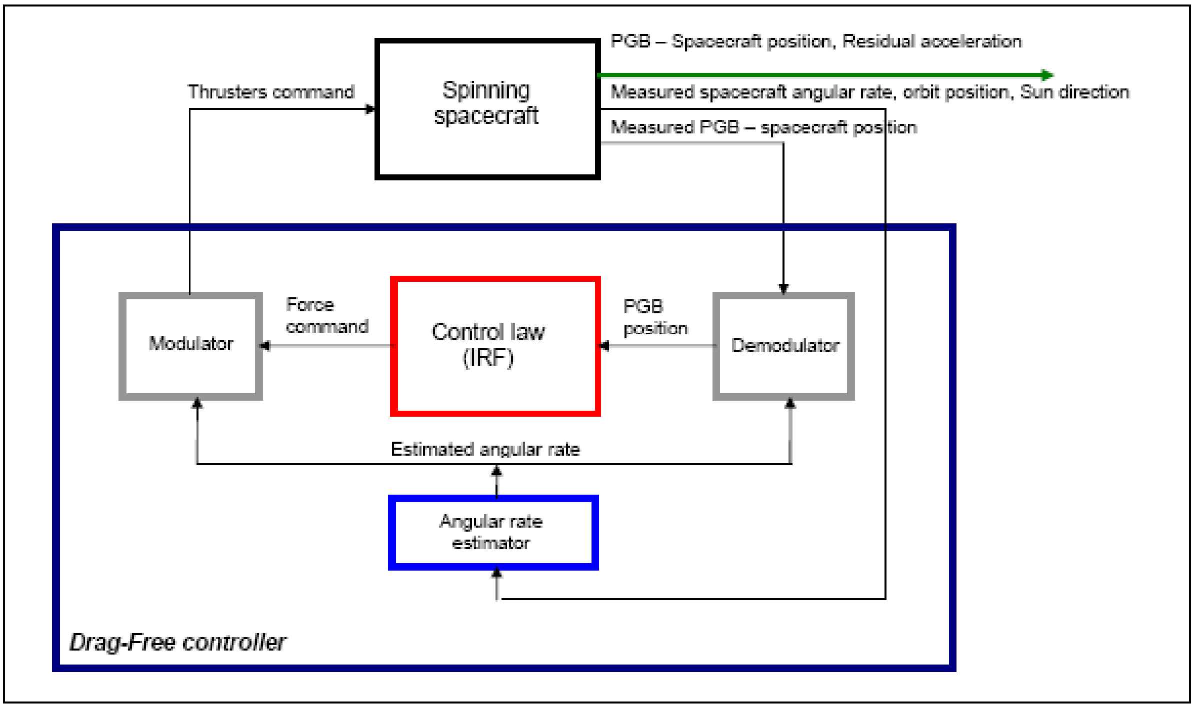

Figure 8-5 - Controller designed in Body frame – block diagram

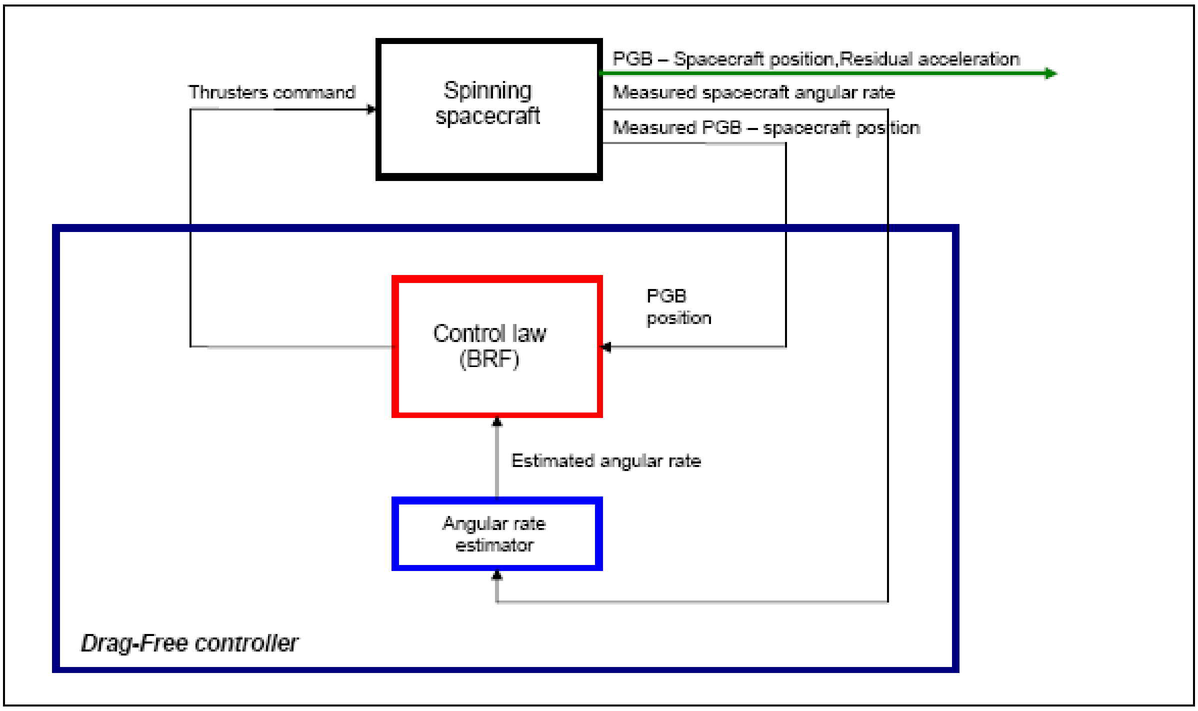

Figure 8-6 - Controller designed in Inertial frame – block diagram

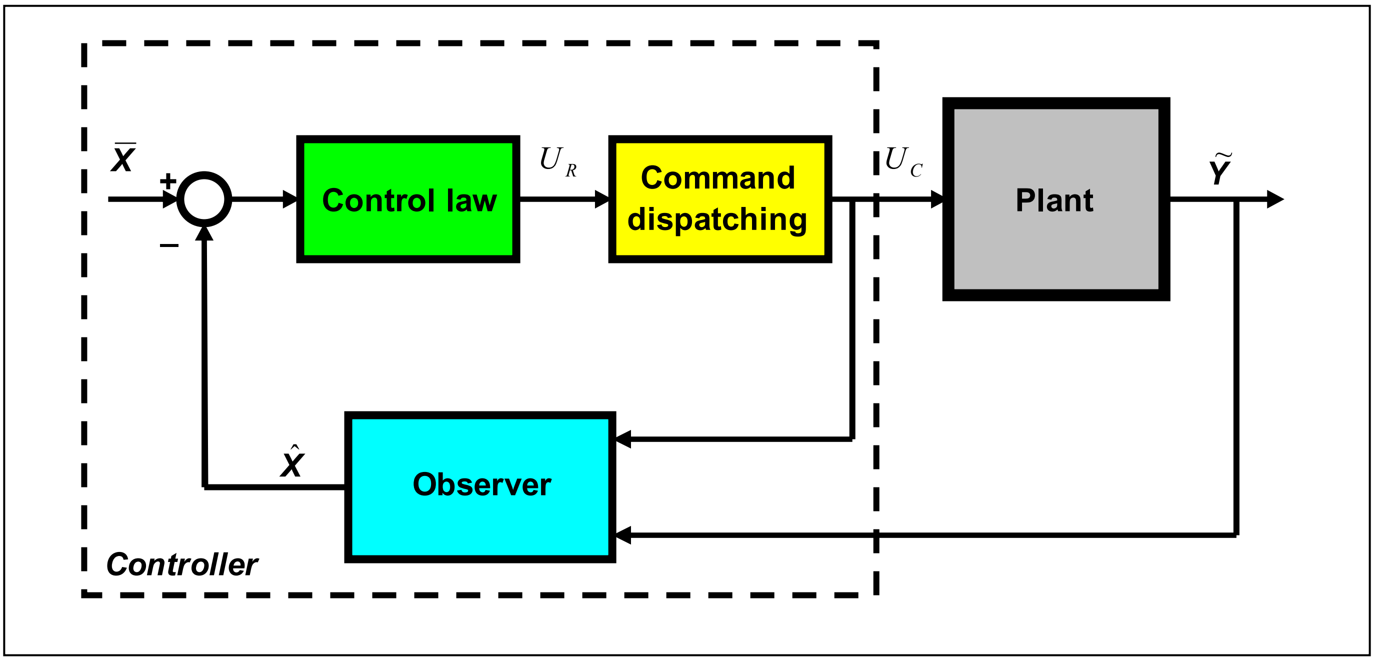

Figure 8-7 – Block diagrams a functions considered for the algorithm design.

State observer has in charge the reconstitution in real-time of all relevant plant state variables. It embeds:

- the dynamic and kinematics plant models with acceptable and/or convenient simplifications;
- relative disturbance force/torque model acting on the spacecraft and PGB;
- feed-forward by commanded force/torque.

It is realized as a discrete dynamic system, according to the following state equation:

$$\hat{\boldsymbol{X}}(i+1) = \boldsymbol{A}\hat{\boldsymbol{X}}(i) + \boldsymbol{B}_U \boldsymbol{U}_C(i) + \boldsymbol{B}_Y \widetilde{\boldsymbol{Y}}(i)$$

where

$\hat{\boldsymbol{X}}$: estimated state variables;
$\widetilde{\boldsymbol{Y}}$: measured variables;
$\boldsymbol{A}$: state evolution matrix;
$\boldsymbol{B}_U$: input matrix of the command;
$\boldsymbol{B}_Y$: input matrix of the measure;
$\boldsymbol{U}_C$: command send to the actuator;
i : current sample step;
$i+1$: next sample step.

XY drag-free observer has been designed neglecting the coupling between X and Y axes obtaining two one-axis observers. This is possible since the design has been done considering the inertial reference frame and the high observer bandwidth. The model state variables are 5 for X axis observer and 5 for Y axis observer. They are the relative position and velocity, disturbance acceleration constituted by an integrator preceded by a harmonic oscillator. Each observer embeds the model given in Figure 8-8.

Matrices $\boldsymbol{A}$, $\boldsymbol{B}_U$ and $\boldsymbol{B}_Y$ for the XY drag-free controller are provided in chapter 16.

Z drag-free observer has been designed as for X and Y axes. The general model embedded in the one-axis observer is shown in Figure 8-8. X_0 represents the relative position, X_1 the relative velocity, X_2 the disturbance acceleration. Depending on the considered axis and the reference frame, specific values have been considered for α, β, ω_X and m_X.

XY whirl observer is based on the plant model written in the body reference frame, with the addition of a simple disturbance force model. The overall plant model state variables are 6.

Z spin rate observer embeds the double integration dynamics and a simplified disturbance torque model. The number of model state variables is 4; the observer is a 5th order discrete model due to the introduction of a dynamic feed-back.

Usually, the control law function computes the required force based on the sum of the following terms:

- proportional to the difference between reference relative position and estimated one;
- proportional to the difference between reference relative velocity and estimated one;
- estimated disturbance force.

The general model is a linear combination of all estimated state elements, i.e.:

$$\boldsymbol{U}_R(i+1) = -\boldsymbol{K}\hat{\boldsymbol{X}}(i+1)$$

.

In the XY and Z drag-free controllers the above approach has been totally followed. Instead in the XY whirl controller, the commanded force is proportional to the actual linear velocity in the inertial reference frame and it takes into account the estimated disturbance force.

Starting from the required force provided by control law the command distribution computes:

- the command to be send to each actuator in the assembly;
- the resultant commanded force taking into account actuator resolution, saturations, etc.

Resultant commanded force is fed to the observer.

Observers' gains and control law gains have been computed according to pole placement approach. Controllers sampling frequency has been fixed to 10Hz (1 order of magnitude higher than the spacecraft spin rate).

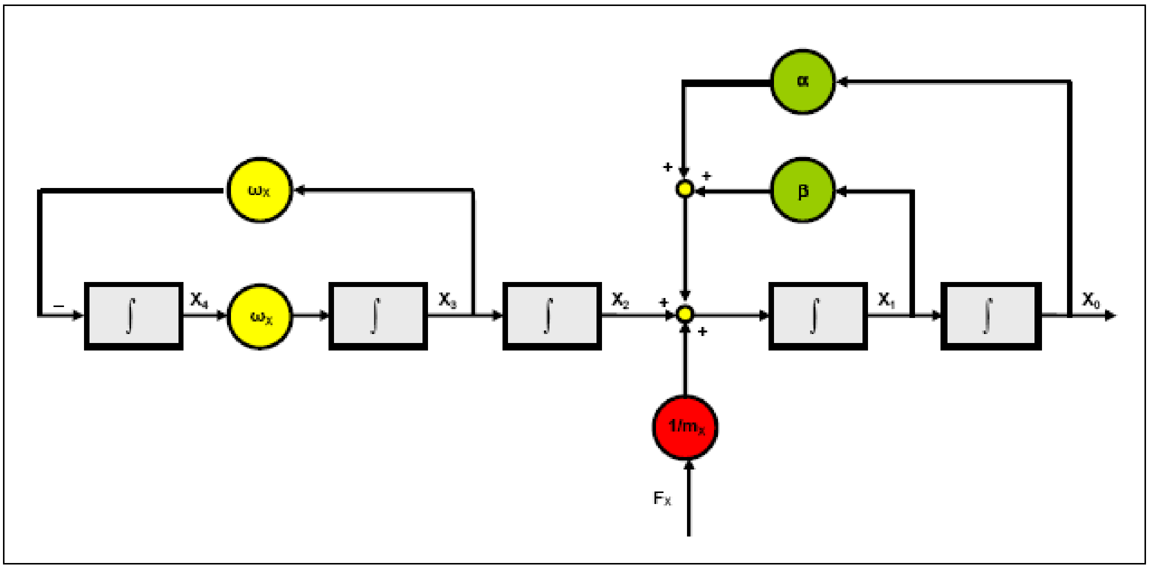

Figure 8-8 – Model embed in the one-axis observer (X , Y and Z axes).

The dispatching is a non-linear function that computes the thrust to be applied to each thruster in order to provide the required forces and torques. Formally

$$\boldsymbol{U}_C(i+1) = \textbf{\textit{Dispatching}}\left(\boldsymbol{U}_R(i+1)\right)$$

$\boldsymbol{U}_R$: required command (force and torque);

$\boldsymbol{U}_C$: command send to the actuator.

Depending on the available computation capabilities, the dispatching function may be based on different algorithms. Correct design of such a function is a key point for fuel saving. Here, the application of simplex like algorithms (linear programming for the solution of an optimization problem) will be considered.

Starting from the required force and torque at spacecraft level, the required force to be commanded to each thrusters in the assembly shall be computed. Such a computation takes into account minimum and maximum commandable forces and quantization level:

```
$u_c(i+1)$=(int)( $u_R(i+1)$/lq+0.5)

if ($u_c(i+1)>u_{MAX}$)
    $u_c(i+1)=u_{MAX}$
if ($u_c(i+1)<u_{MIN}$)
    $u_c(i+1)=u_{MIN}$
```

Using the forces commanded at each thruster in the assembly, the resulting commanded force and torque at spacecraft level are computed for estimation purposes (observer).

The control algorithms embed a sort of notch filter to achieve the very high required disturbance rejection taking into account the sampling frequency limitations. As well known from literature, the rejection is very high only in an interval of frequencies very little around the value considered for the design. Rejection greater than 25000 may be achieved only for if $\left|\frac{\tilde{\omega}_S - \omega_S}{\omega_S}\right|$ is lower than 10-4. The angular rate shall be well known but with less stringent requirement for the whirl controller too.

8.3 Modulation and demodulation

The simplification in the observer design out coming from the design based on the inertial reference frame is paid by the introduction of two additional functions for the measurement demodulation and command modulation.

The measurements of the PGB-satellite relative position in the plane XY are transformed to the equivalent relative position in the inertial reference frame by demodulation. The de-modulated relative positions are sent to the observer. The control law compute the force to be provided to the plant in inertial reference frame; by modulation such force is transformed in body frame.

The scheme considered is outlined in Figure 8-9 and Figure 8-10.

The measurement demodulation is executed using *N* measurement (*N*=10 in the figure and in the design). The demodulation is executed according to the following algorithm:

$$\begin{bmatrix} \tilde{x}_I \\ \tilde{y}_I \end{bmatrix} = \left(\boldsymbol{A}^T \boldsymbol{A}\right)^{-1} \boldsymbol{A}^T \tilde{\boldsymbol{Y}}$$

$$\tilde{\boldsymbol{Y}} = \begin{bmatrix} x_{B\_0} \\ y_{B\_0} \\ x_{B\_1} \\ y_{B\_1} \\ \dots \\ x_{B\_9} \\ y_{B\_9} \end{bmatrix}$$

$$\boldsymbol{A} = \begin{bmatrix} \cos(\vartheta_0) & \sin(\vartheta_0) \\ -\sin(\vartheta_0) & \cos(\vartheta_0) \\ \cos(\vartheta_1) & \sin(\vartheta_1) \\ -\sin(\vartheta_1) & \cos(\vartheta_1) \\ \dots & \dots \\ \cos(\vartheta_9) & \sin(\vartheta_9) \\ -\sin(\vartheta_9) & \cos(\vartheta_9) \end{bmatrix}$$

$$\vartheta_j = j\frac{2\pi}{N} \qquad j = 0,\dots,N-1$$

By symmetry, the modulation is computed according to the following algorithm

$$\begin{bmatrix} u_{R\_X0} \\ u_{R\_Y0} \\ u_{R\_X1} \\ u_{R\_Y1} \\ \dots \\ u_{R\_X9} \\ u_{R\_Y9} \end{bmatrix} = \boldsymbol{AU}_R = \boldsymbol{A}\begin{bmatrix} u_{R\_XI} & u_{R\_YI} \end{bmatrix}$$

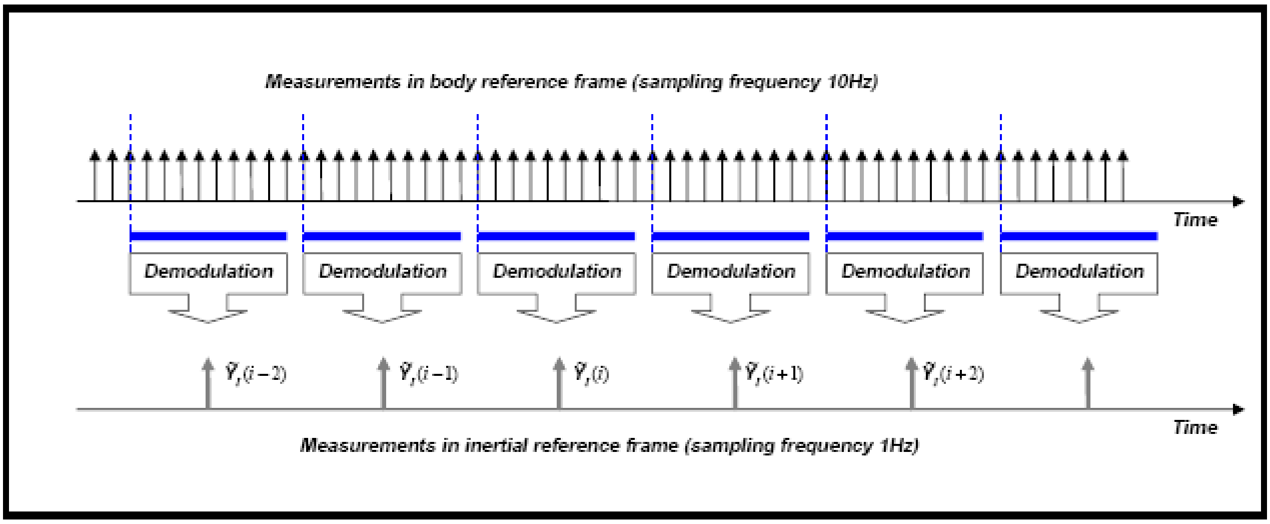

Figure 8-9 – Demodulation scheme.

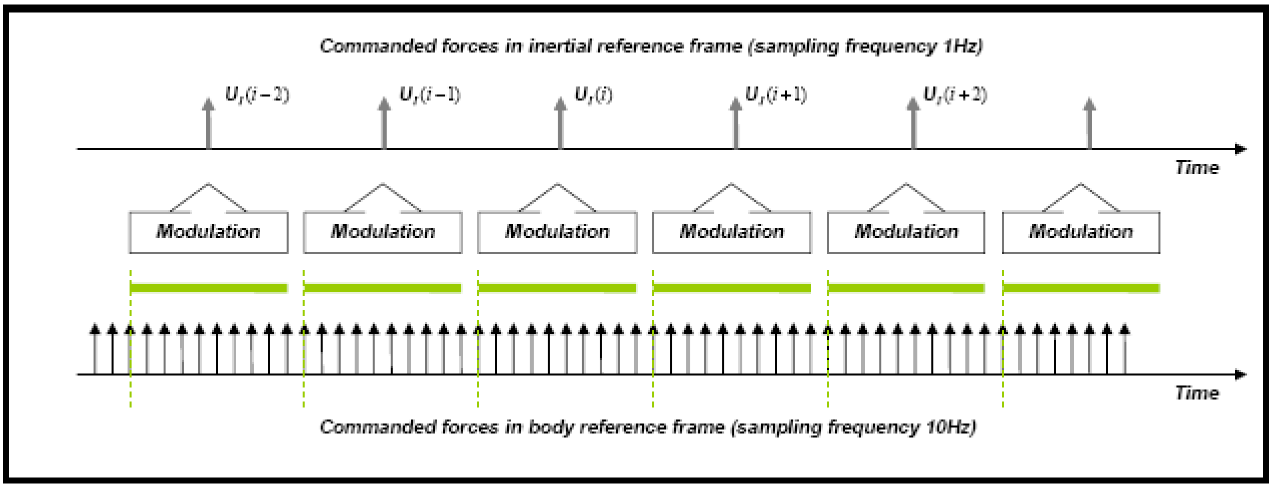

Figure 8-10 – Modulation scheme

8.4 Spin-rate control

The problem to be prevented is the angular shift between PGB and satellite. It occurs always due to differential de-spin effects between PGB and satellite, and due to Sun/eclipse transition, when the spacecraft spin rate increases/decreases as consequence of the reduction/rising of the inertia moment. The second effect is the major one.

To recover de-spin and angular shift, during Phase A1 a hybrid solution has been outlined ([RD 1]): a passive compensation system plus an active one based on moving masses.

The passive system was based on suitable masses suspended on rods that expand and contract in "counter-phase" to the spacecraft. The system can consist of a high-CTE rod cantilevered (and thermally anchored) on the outer shell and connected to a parallel, low-CTE rod supporting a balance mass on its free end.

A compensating system of masses, such as that described in above, can reduce the inertia variation (by expanding/contracting in the opposition with respect to the spacecraft outer shell) to about 10% of the total effect, in the worst case. This residual 10% variation needs an active control able to move small masses accordingly.

Thermal analysis and structural considerations executed during Phase A2 show that by proper design and material selection the variation of inertia moment may be no greater than about 10^{-5}. This value suggests the compensation by thrusters since the additional total impulse is only a little fraction of the overall value.

The total impulse is linked to the inertia moment variation by the following formula:

$$I_T = \left(\frac{dI_a}{I_a}\right)\frac{I_a\omega_S}{\alpha}N$$

where

$\left(\frac{dI_a}{I_a}\right)$: inertia moment relative variation;

N : number of transition Sun/eclipse plus transition eclipse/Sun;

α : geometrical efficiency of the assembly with respect to Z-axis torque.

For two years mission N=10520 (6000s orbit period), for the assembly described in chapter 9.3.1 $\alpha = 0.3980$:

$$I_T \cong 2.5\,10^7\left(\frac{dI_a}{I_a}\right)$$

It is possible to assume that 10% of the overall fuel will be allocated for spin-rate control, i.e. 500÷1000Ns. It means that acceptable inertia variation shall be such that $\left(\frac{dI_a}{I_a}\right) < 2 \div 4\,10^{-5}$.

Figure 8-11 shows the block diagram of the spin-rate control. The basic measurement is the relative rotation between PGB and satellite around Z-axis, and it is provided using capacitors as sensors. The controller sampling frequency is the same used also for other controller (10Hz).

The design has been done following the same approach already described in previous chapters. Z axis spin rate observer embeds the double integration dynamics and a simplified disturbance torque model (see Figure 8-12). The number of model state variables is 4; the observer is a 5th order discrete model due to the introduction of a dynamic feed-back.

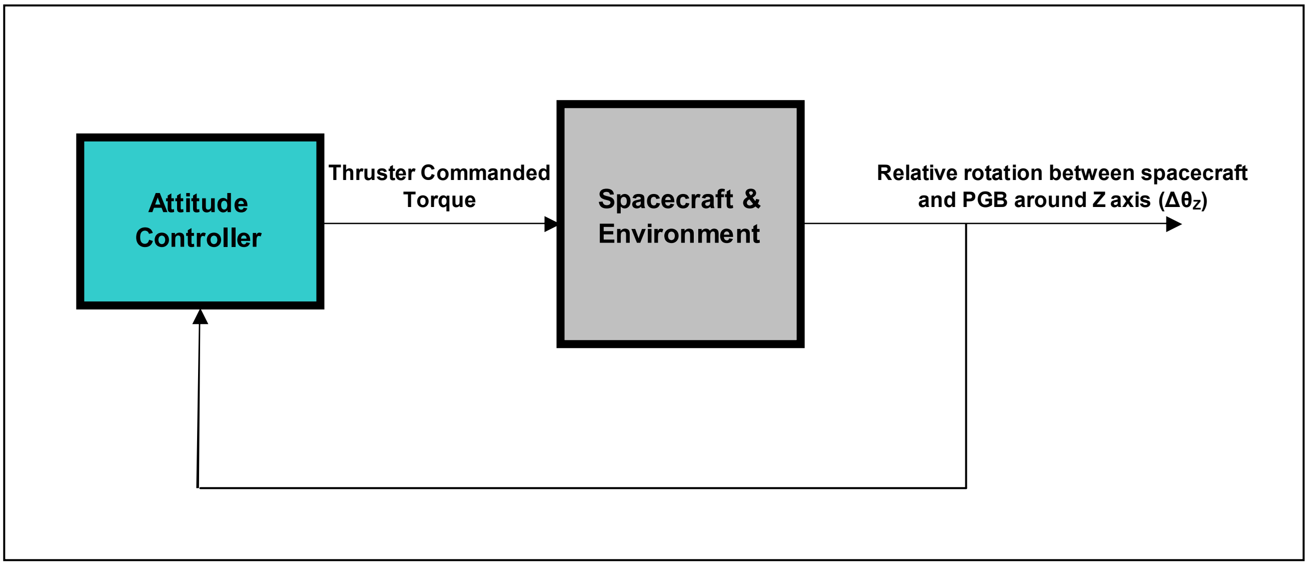

Figure 8-11 – Architecture of the spin rate control.

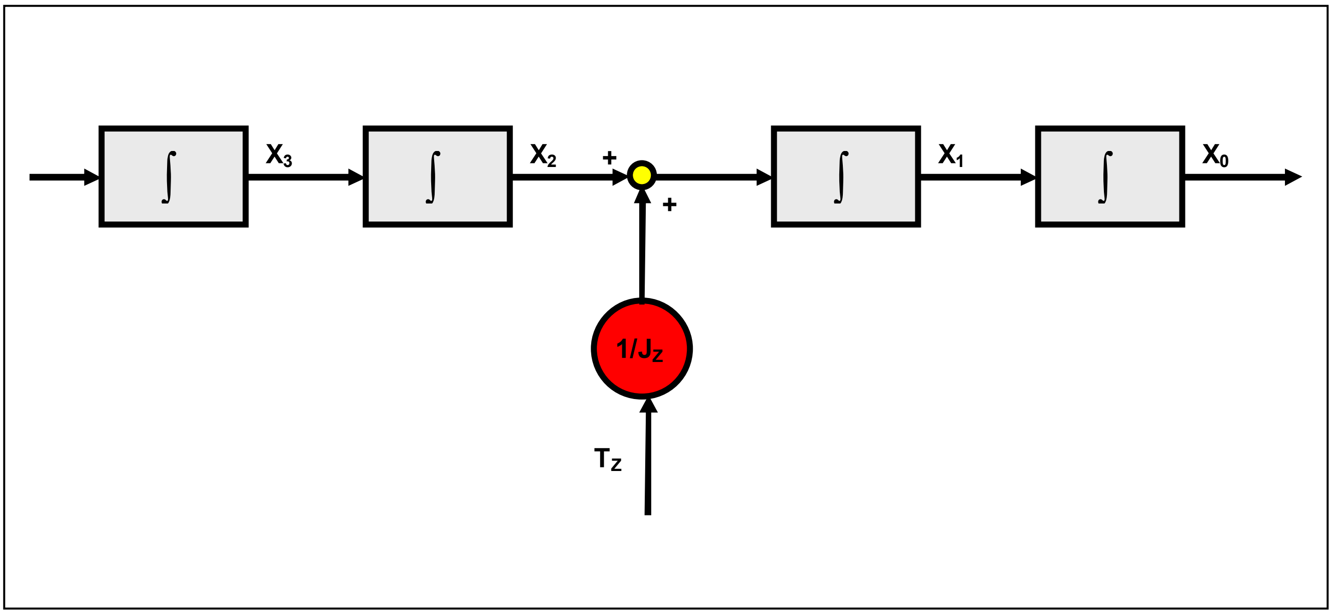

Figure 8-12 – Model embed inside the spin-rate observer.

9. DRAG-FREE ACTUATOR

9.1 Requirements

From the flow-down of the requirements provided in chapter 7.2, taking into account the available drag-free design, a preliminary set of thrusters requirement has been derived.

The requirements have been derived considering the assembly described in chapter 6.5, and considering 1 and 2 Hz as spacecraft spin rate. Table 9-1 and Table 9-2 show the derived preliminary requirement.

No	Parameter	Unit	Value	Comments
1	Maximum thrust	μN	>=150	50% margin
2	Max thruster response time[6]	ms	20	@ commanded step (up and down) >= 60 μN
3	Resolution (quantization)	μN	6	TBC, not critical
4	Max noise	μN/√Hz	6	Around 2 Hz
5	Scale factor error	%	4	Peak
6	Update com rate	Hz	20	TBC
7	Total impulse	Ns	4500	20 % margin
8	Minimum thrust	μN	<=10	TBC
9	Vector stability	rad	0.06	Peak, at 60 μN
10	Centrifugal acceleration	g	<17.4	20 % margin, 0.75m spacecraft radius

Table 9-1 – Thrusters requirements - Spin rate: 2Hz

The requirements have been derived considering the capability to compensate the perturbing drag on X-Y plane and Z axis at 20 Hz, in agreement with the current design solution. It means that the perturbing force is compensated in real-time with a step function at quantized values as shown in Figure 9-1 (the controller reduces the disturbance at spinning rate in agreement with sensitivity function, but the ZOH introduces high frequency disturbances as shown in Figure 9-2).

In principle, at least two more simple functions (less demanding in terms of thruster's response time) may be considered to compensate the perturbing force:

- square wave (Figure 9-3 shows the spectrum of the additional noise);
- triangle wave (Figure 9-4 shows the spectrum of the additional noise).

---

[6] Thrust response time is defined as the time required to achieve the 90% of the commanded step, and to remain definitively over this threshold.

No	Parameter	Unit	Value	Comments
1	Maximum thrust	μN	>=150	50% margin
2	Max thruster response time[7]	ms	40	@ commanded step (up and down) >= 60 μN
3	Resolution (quantization)	μN	24	TBC, not critical
4	Max noise	μN/√Hz	18	Around 1Hz
5	Scale factor error	%	12	Peak
6	Update com rate	Hz	10	TBC
7	Total impulse	Ns	4500	20 % margin
8	Minimum thrust	μN	<=10	TBC
9	Vector stability	rad	0.17	Peak, at 60 μN
10	Centrifugal acceleration	g	<4.4	20 % margin, 0.75m spacecraft radius

Table 9-2 – Thrusters requirements - Spin rate: 1Hz

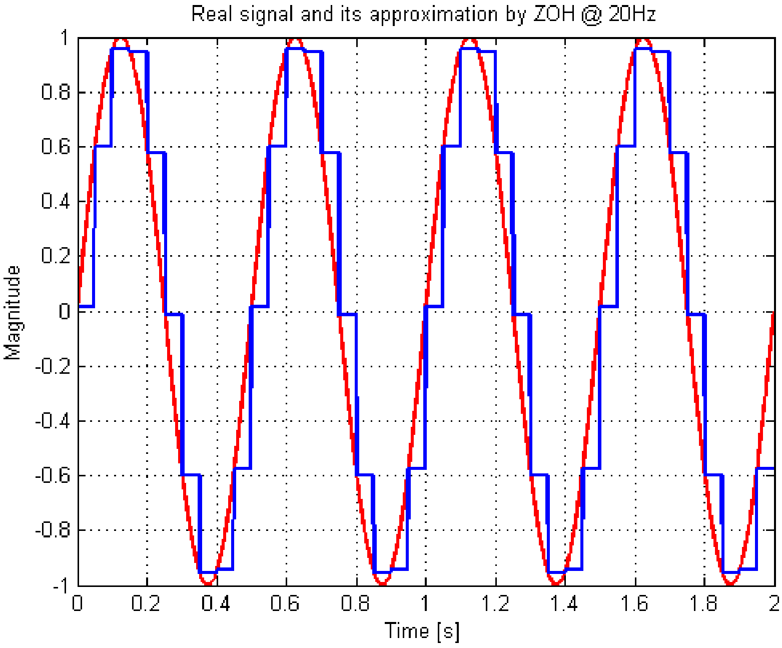

Figure 9-1 – Theoretical drag and solar pressure compensation at 20Hz by ZOH

---

[7] Thrust response time is defined as the time required to achieve the 90% of the commanded step, and to remain definitively over this threshold.

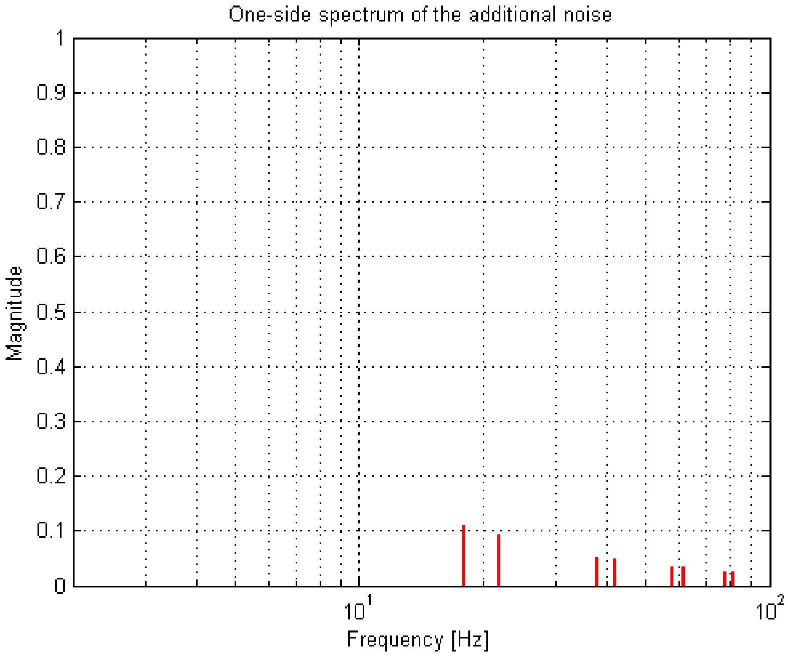

Figure 9-2 – Spectrum of the additional harmonic introduced by ZOH at 20Hz

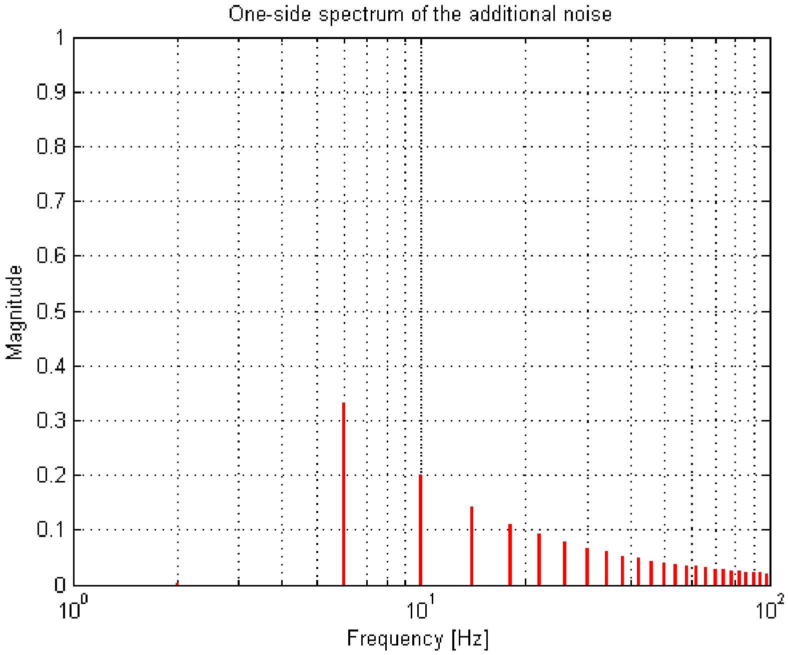

Figure 9-3 – Spectrum of the additional harmonic introduced by square wave at 2Hz

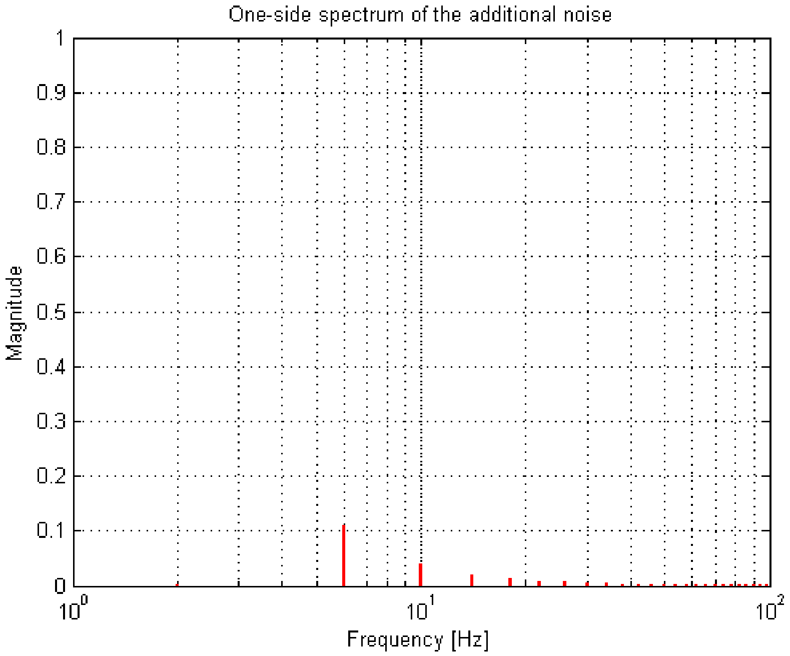

Figure 9-4 – Spectrum of the additional harmonic introduced by triangle wave at 2Hz

9.2 Survey of available technologies

The following chapters starts from [RD 7][RD 8] for FEEP, and [RD 9] for cold-gas.

9.2.1 FEEP thrusters

9.2.1.1 Development Status

FEEP Thrusters are being developed for the ESA Lisa Pathfinder (LPF) mission and the CNES Microscope mission (see Figure 9-5).
Thruster development is nearly completed, and the preparation of the Lisa Pathfinder FEEP Cluster Assembly (FCA) Qualification Model is ongoing. Manufacturing of FM parts for LPF was also released. Microscope programme is currently on hold, pending completion of thruster's development.

During thrusters development phase, the following results were achieved:
- demonstration of priming principle and repeatability (6 thrusters in a row were successfully activated and fired);
- full performance characterization;
- demonstration of endurance up to more than 1000 Ns (> 3200 hours firing);
- successful performance of environmental testing (sine + random vibration, thermal balance);

- direct thrust measurement (ongoing at TAS-I Turin);
- neutral flow measurement characterization (ongoing at ONERA Palaiseau).

LISA Pathfinder (ESA – Technology demonstration for LISA)

Microscope (CNES - Equivalence principle)

Figure 9-5 – ESA missions based on FEEP micro-propulsion.

9.2.1.2 Evaluation of thrusters performances vs. GG requirements

Maximum thrust

- Thruster is designed and currently being qualified for a maximum thrust of 150 μN.
- Command capability is, at present, up to 204.8 μN.
- During development phase, at least 150 μN were measured for all thrusters.
- Thrust up to 540 μN was recorded during one test, showing large design margins

Minimum thrust

- Thruster is designed and currently being qualified for a minimum thrust of 0.3 μN.
- Command capability is, at present, down to 0.05 μN.
- Dedicated tests were performed to measure 0.3 μN and below.
- Thrust generation was demonstrated by ion beam probes.

Thrust resolution

- Thruster/PCU are designed and currently being qualified for a thrust resolution of 0.1 μN.
- Command quantization is 12 bit, i.e. 4096 steps in the range 0.05 μN to 204.8 μN.
- Minimum commanded step is then 50 nN.
- Resolution of 0.1 μN was verified during dedicated tests.

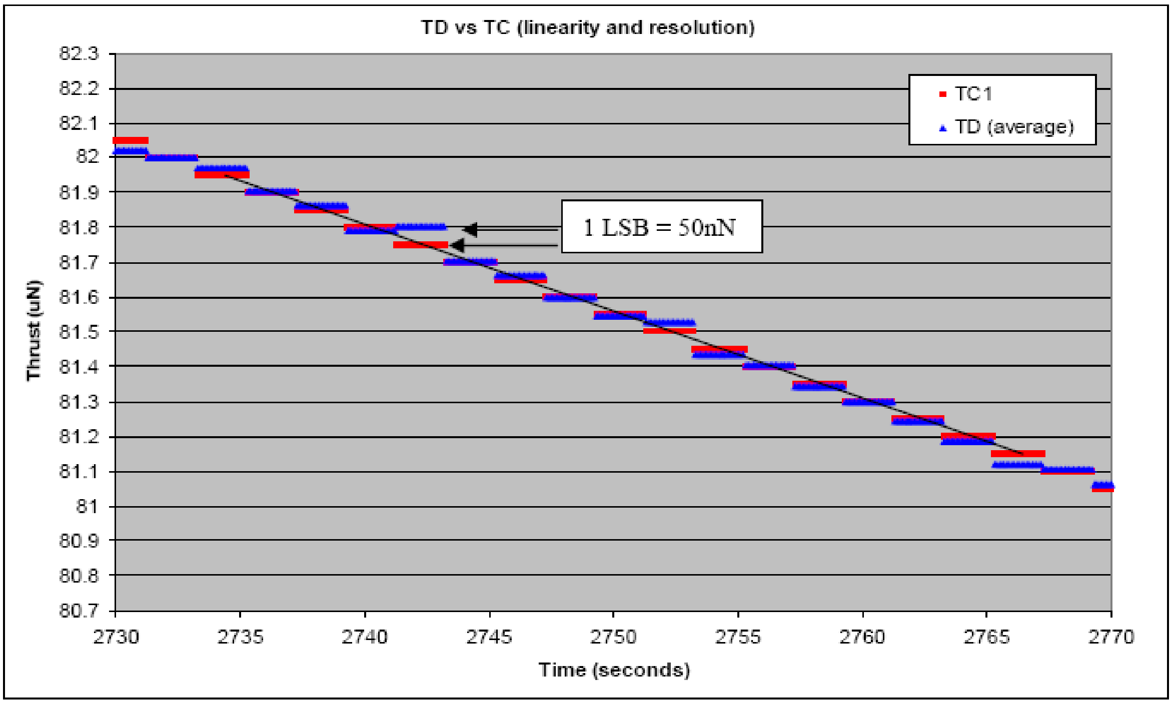

Figure 9-6 – FEEP thrusters resolution.

Thrust response time (60 µN step) and command frequency

- Current response (for 60 µN step) is about 80 to 150 ms, (depending on thrust and up or down command), with command frequency at 10 Hz.
- Internal digital control loop works at 50 Hz: command frequency at 20 Hz can be easily provided.
- Step response can be improved by:
  - reducing delay;
  - reducing rise time, tolerating some overshoot;
  - reducing fall time, by biasing minimum thrust and/or adding some internal dissipation.

Noise

- The thruster is being qualified for 0.03µN/√Hz (range 0.006 to 5 Hz).

Scale factor error

- Performance to be verified.
- PCU allows scale factor correction and re-calibration with a 12 bit resolution (individual command correction).
- Requirement is not deemed critical.

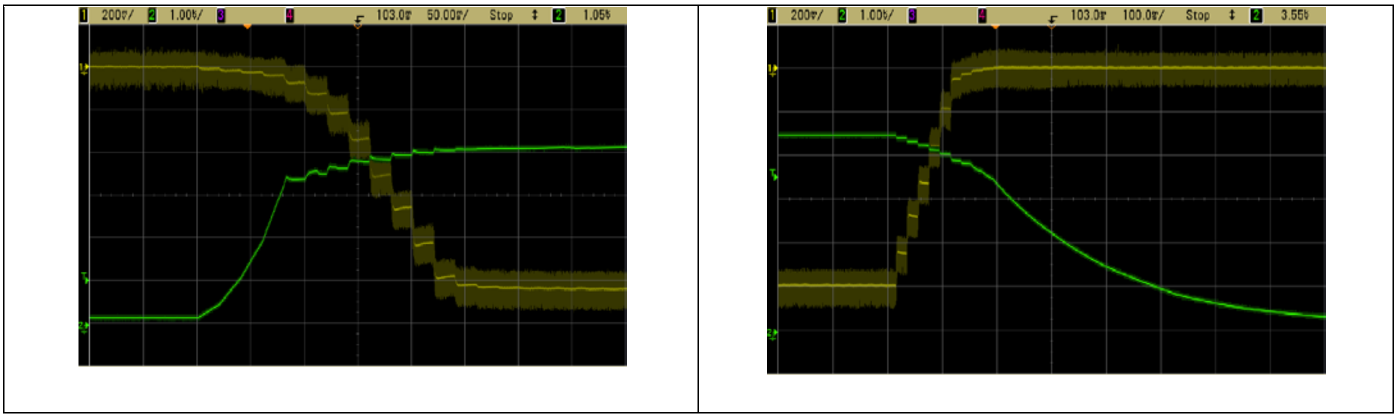

Figure 9-7 – FEEP response time.

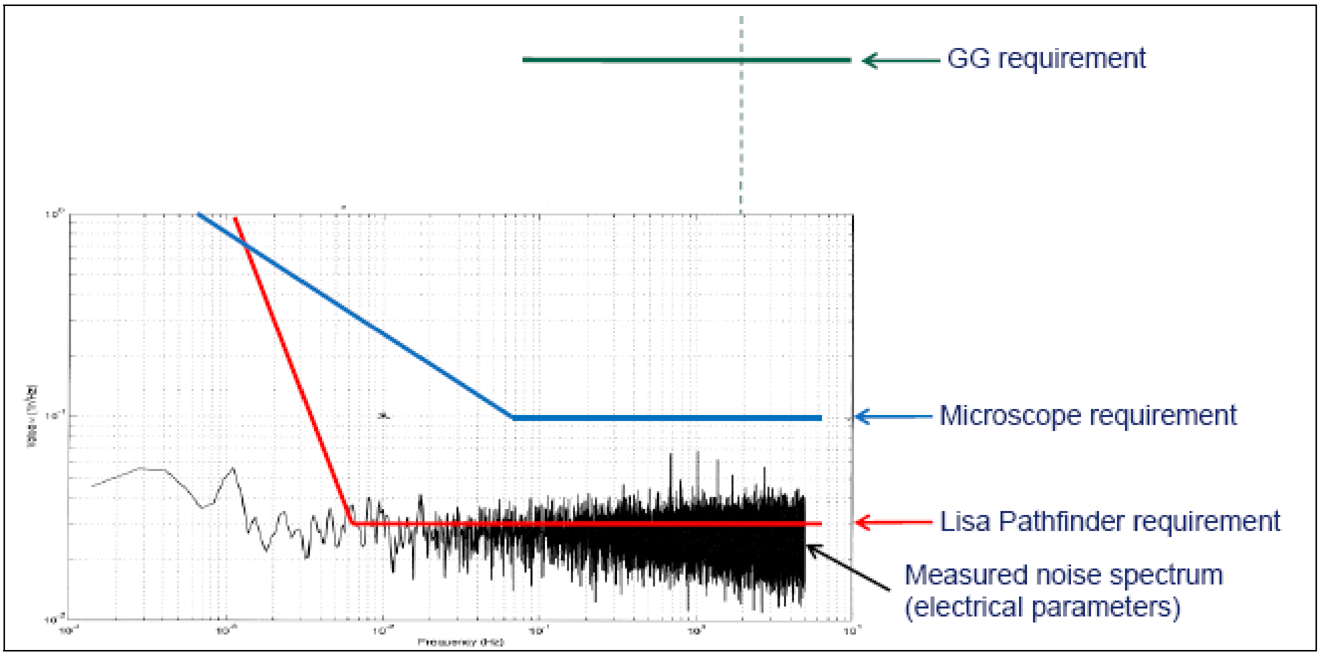

Figure 9-8 – FEEP noise profile compared with GG requirement.

Total Impulse.

- Thruster is designed vs. a requirement of 2900 Ns (Lisa Pathfinder). Requirement is likely to be relaxed to 1800 Ns.
- Life test (on QM) will be performed up to 1100 Ns (with possible extension to higher total impulse). Analysis will be performed to predict EOL performance. At present, > 1000 Ns were verified at EM level.
- Propellant tank can be doubled if needed to cope with higher total impulse.

Vector stability.

- Requirement is met for option B.
- Vector error budget for option A (according to recent test results) is about 5 deg

Arcing

- As every ion thrusters, FEEP is prone to arc discharge events
- Arc discharge occurs usually between emitter and accelerator electrodes (i.e., it is an event internal to the thruster)
- The discharge event lasts between 2 and 10 µs. After that, voltage drops down and thrust is temporarily interrupted. Thrust is recovered after the capacitors of PCU are recharged. Typical time is that of thrust command response (for a 0 to nominal thrust step).

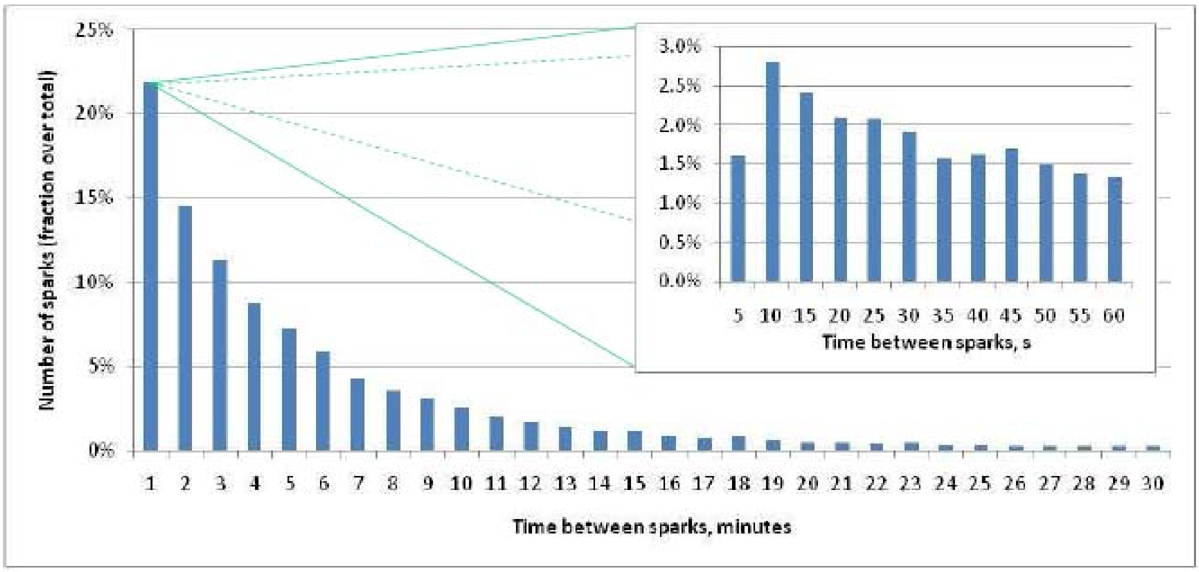

Figure 9-9 – Percentage of sparks vs. time between sparks

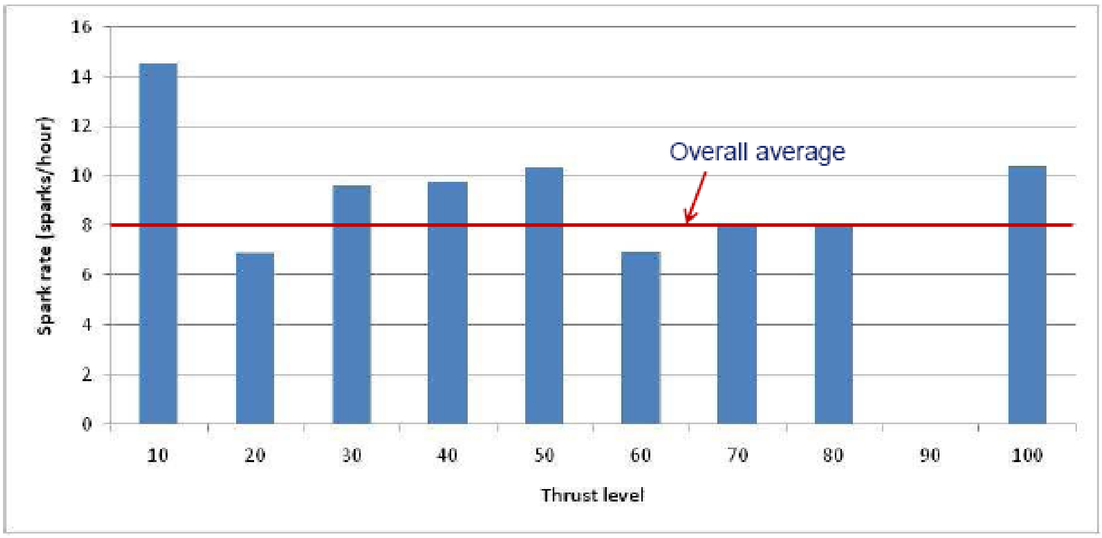

Figure 9-10 – Spark rate vs. thrust level.

Effects of the centrifugal acceleration

Considering the orientation of the thruster (30 deg from spin axis) and the geometry of the tank, the acceleration above corresponds to a maximum hydrostatic pressure of about 20 10^3 Pa.

The maximum theoretical pressure (considering real geometry and worst case cesium surface tension) that the liquid meniscus on the tip of the thruster can sustain is in the order of few hundreds of Pa (up to 1000, depending on actual geometry of slit). Alta demonstrated by test that the thruster can sustain without troubles an hydrostatic pressure in excess of 160 Pa. When compared with the result above, this shows that there is a significant difference (128 times) between what has been demonstrated so far and what would be required for direct application of the thruster to the mission. This can be overcome in several ways. Three possible ways forward are suggested:

- Reduction of the spin rate. To use the thruster “as is”, and with the selected thrust angle, a reduction down to about 0.2 Hz would be required;

- Relocation of the thrusters closer to the spin axis and/or modification of the thrust vector angle. This option alone, however, would not be sufficient to bring the hydrostatic pressure down to the required levels;

- Modification of thruster design, and, in particular, of tank position and shape, to minimize hydrostatic head. This would imply delta development and qualification.

9.2.2 Cold-gas thrusters

9.2.2.1 Development Status

GAIA Micro Propulsion System (MPS), currently under qualification at TAS-I, represents the reference design/technology starting point for configuring/realizing both Microscope and the GG drag-free and attitude control Col Gas Micro Propulsion System.

The GAIA Architecture/ technology/ design is however proposed, both for Microscope and GG with a significant variation requiring the use of an Electronic Pressure Regulator (EPR) instead then a Mechanical Pressure Regulator (MPR) for realizing the Pressure Reduction & Regulation Stage (PRS).

The main advantages of an EPR based on regulation valves as actuating elements are:

- fully european technology (key components are TAS-I products)
- no ITAR exportation/importation problems
- extremely low leakage (at least one order of magnitude better than the MPR)
- very low ripple in the regulated low pressure
- high degree of flexibility (regulated low pressure selectable according to a specified set point)
- contained mass and dimensions.

Figure 9-11 shows the images of key components for the cod-gas thrusters.

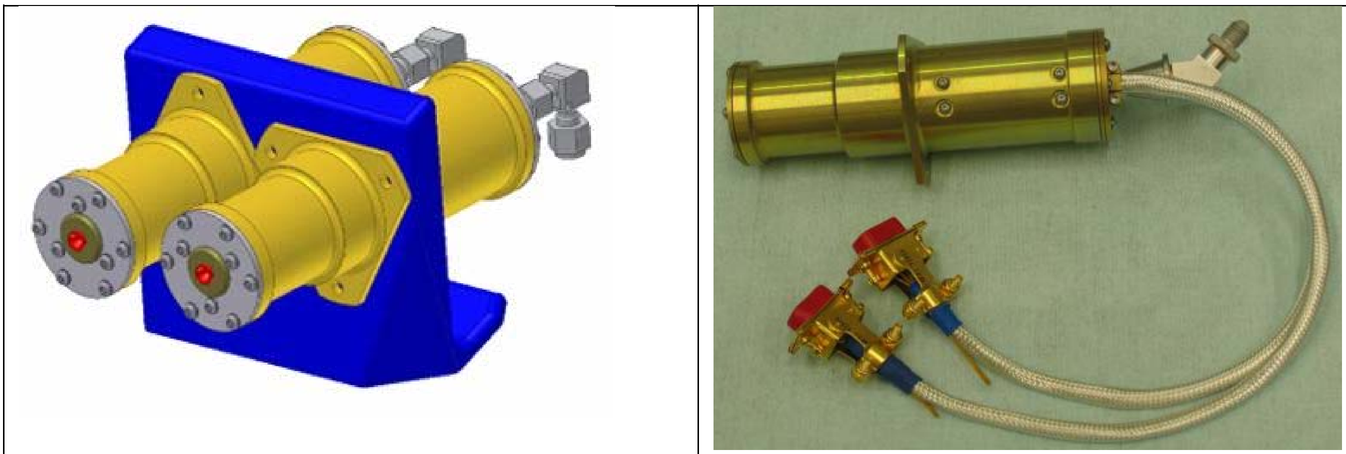

Micro-Thruster couple (nominal+ redundant) accommodated on the L shaped mechanical support

Micro-Thruster EQM model assembled in view of qualification Campaign vs. GAIA requirements

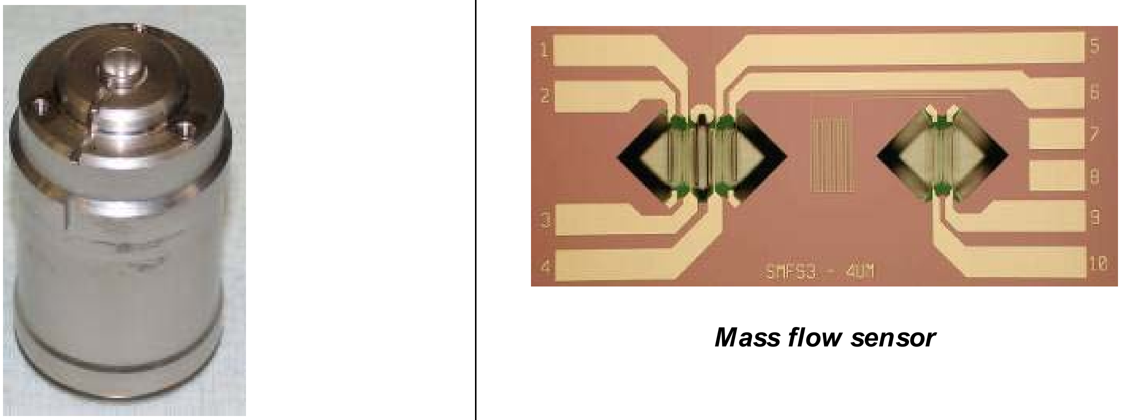

EQM of the Thrust Valve for GAIA MPS

Mass flow sensor

Figure 9-11 – Pictures of the main components of the cold-gas micro-thrusters.

9.2.2.2 Evaluation of thrusters performance vs. GG requirements

Maximum thrust

- Thrust levels up to 500 μN achievable.

Minimum thrust

- 1 μN achievable with the current GAIA design.

Thruster response time

- about 100 ms: commanded thrust level below 50 µN;
- 100 to 200 ms: commanded thrust level in the 50 to 500 µN range.

Resolution

- 1 µN achievable with the current GAIA design.

Noise

- 1 µN/√Hz from 0.01 Hz to 1 Hz
- 0.045 µN/√Hz from 1 Hz to 150 Hz achievable with GAIA design.

Scale factor error

- 1% for GAIA

Command update rate

- 1 Hz for GAIA.

Total impulse

- @150 µN the total operating time is about 8400h. The same total impulse figure required for GAIA.
- Due to the technology, about 60 million cycles have been foreseen with the valve. 700 million cycles at 10 Hz, in open loop, performed on the Thruster Valve engineering model.

Thruster Vector stability

- No data available at the moment.

Effects of the centrifugal acceleration

The direction of the centrifugal acceleration acting on the thrust actuator is almost orthogonal to the thrust direction in any operational flight situation. In this case the centrifugal acceleration is not believed to produce any remarkable effect on the thrust actuator correct operation.

Should, for some reasons or any particular flight condition, the centrifugal acceleration result directed in the same direction of the thrust, there could be a “side” effect to be taken into account and evaluated.

The resulting centrifugal force could act in the direction of forcing the opening of the thruster valve orifice by acting in opposition to the mechanical force exerted by the spring that maintains the valve fully closed, when in the off condition (no voltage applied to the piezo actuator).

- force exerted by the spring : about 10 N (corresponding to about 1 kg)
- mass of the valve actuator: 10 grams (0.01 kg)
- centrifugal acceleration: 17.4 g
- centrifugal force acting on the Valve actuator: about 0.174 kg

Centrifugal force (0.174 kg) << spring strength (1 kg)

No significant risk of valve opening induced by the centrifugal force.

9.3 Assembly for micro-thrusters

9.3.1 FEEP solution

The definition of the assembly starts from:

- force and torque to be applied;
- failure management.

Main forces and torque to be compensated are:

- force on XY plane for drag-free;
- torque on Z axis for spin rate control.

Since each FEEP thruster has its own tank and each electronic unit is internally redundant, the failure management approach is different with respect to what it is used for cold-gas and chemical thrusters. Using FEEP the thruster cluster concept is considered (see [RD 9]).

For GG, the FEEP assembly is constituted by 2 clusters of 4 thrusters each one. A preliminary design of the cluster is provided in Figure 9-12. Table 9-3 reports the considered angles defining thrust direction in cluster reference frame. The clusters are mounted in the spacecraft X axis direction and in opposite versus (see the sketch provided by Figure 9-13)

The applied force $\boldsymbol{F}$ and torque $\boldsymbol{T}$ at satellite level are related to the commanded thrust to each thruster $\boldsymbol{u}$ by the relation

$$\begin{bmatrix} \boldsymbol{F} \\ \boldsymbol{T} \end{bmatrix} = \boldsymbol{B}\,\boldsymbol{u}$$

being $\boldsymbol{B}$ the assembly matrix related to the cluster geometry and cluster mounting position.

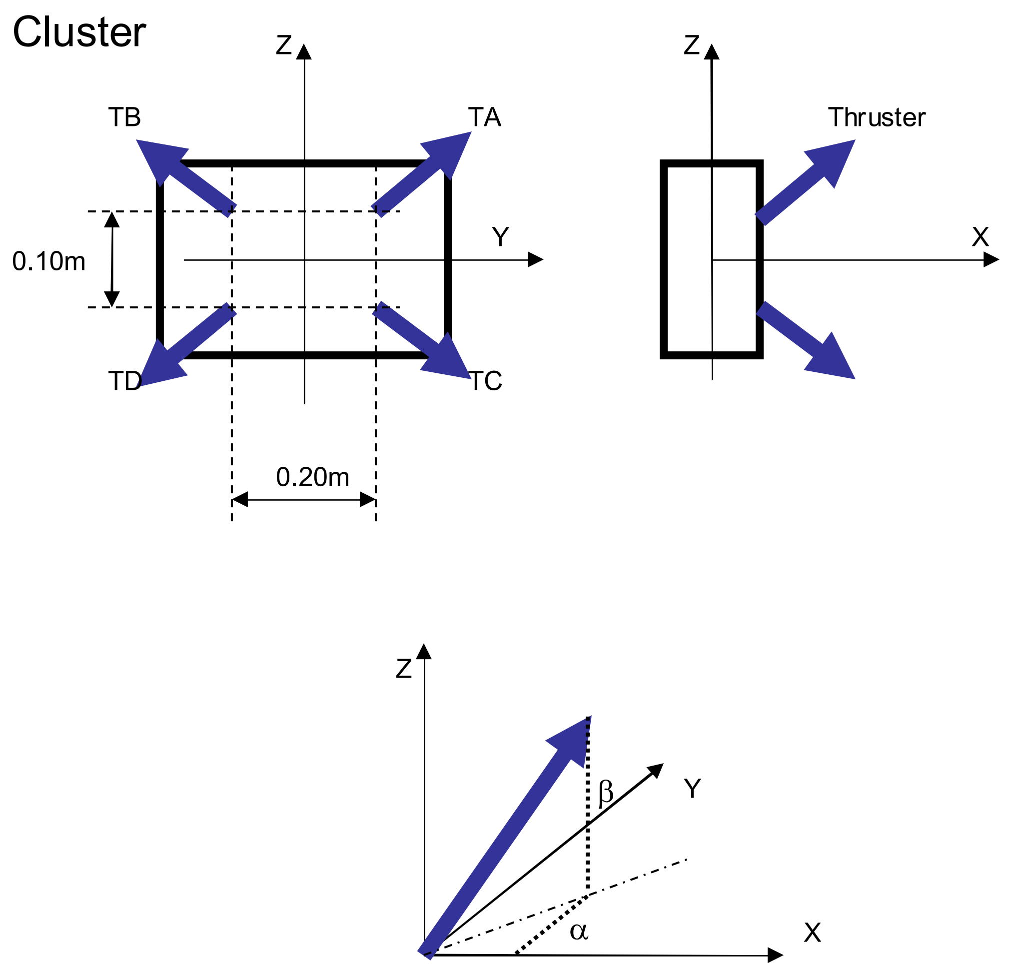

Figure 9-12 – FEEP cluster: the arrow shows the direction of ion way out.

Thruster code	α	β
TA	+45°	+30°
TB	-45°	+30°
TC	+45°	-30°
TD	-45°	-30°

Table 9-3 - FEEP cluster: thrust nominal mounting angle

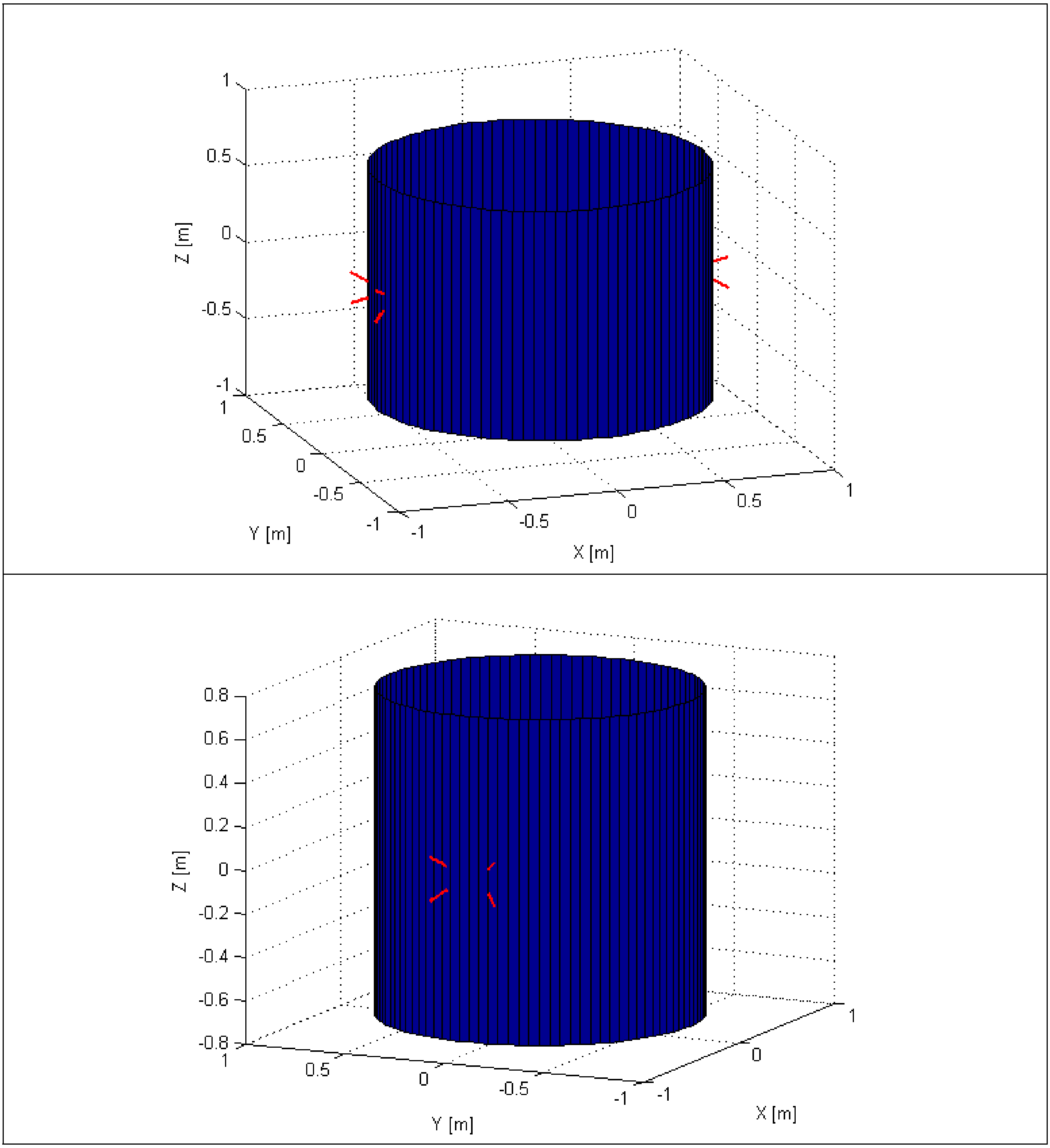

Figure 9-13 – FEEP assembly: clusters and thrusters mounting positions.

Thruster	Position			Thrust direction		
	X	Y	Z	X	Y	Z
1A	0.7500	0.1000	0.0500	-0.6124	-0.6124	-0.5000
1B	0.7500	-0.1000	0.0500	-0.6124	0.6124	-0.5000
1C	0.7500	0.1000	-0.0500	-0.6124	-0.6124	0.5000
1D	0.7500	-0.1000	-0.0500	-0.6124	0.6124	0.5000
2A	-0.7500	0.1000	0.0500	0.6124	-0.6124	-0.5000
2B	-0.7500	-0.1000	0.0500	0.6124	0.6124	-0.5000
2C	-0.7500	0.1000	-0.0500	0.6124	-0.6124	0.5000
2D	-0.7500	-0.1000	-0.0500	0.6124	0.6124	0.5000

Table 9-4 - FEEP mounting position and thrust direction for each clusters

For the selected case, the assembly matrix is equal to:

$$\begin{matrix} -0.6124 & -0.6124 & -0.6124 & -0.6124 & 0.6124 & 0.6124 & 0.6124 & 0.6124 \\ -0.6124 & 0.6124 & -0.6124 & 0.6124 & -0.6124 & 0.6124 & -0.6124 & 0.6124 \\ -0.5000 & -0.5000 & 0.5000 & 0.5000 & -0.5000 & -0.5000 & 0.5000 & 0.5000 \\ -0.0194 & 0.0194 & 0.0194 & -0.0194 & -0.0194 & 0.0194 & 0.0194 & -0.0194 \\ 0.3444 & 0.3444 & -0.3444 & -0.3444 & -0.3444 & -0.3444 & 0.3444 & 0.3444 \\ -0.3980 & 0.3980 & -0.3980 & 0.3980 & 0.3980 & -0.3980 & 0.3980 & -0.3980 \end{matrix}$$

Starting from the required control force and torque, the thrust to be applied on each thruster may be computed by linear programming algorithms (simplex and other more less demanding in terms of computation capability).

The selected assembly permits to apply pure forces and/or pure torques. After first failure and second failure it is possible to have full controllability on X, Y and Z linear axis, on Z angular axis leaving spurious low torque on X and Y axes.

In order to address the total impulse required by each thruster, it has been considered a profile of X,Y and Z forces, and Z torque as shown in Figure 9-14.

Without failure (8 thrusters active), the time history of the thrust to be applied by each thrusters is given in Figure 9-14A. The maximum impulse required at each thruster for 2 years mission equals to 2060Ns.

After first failure (7 thrusters active), the time history of the thrust to be applied by each thrusters is given in Figure 9-14B. The maximum impulse required at each thruster for 2 years mission equals to 4065.

Results show the effective of the selected assembly; optimizations are still possible reducing the β angle.

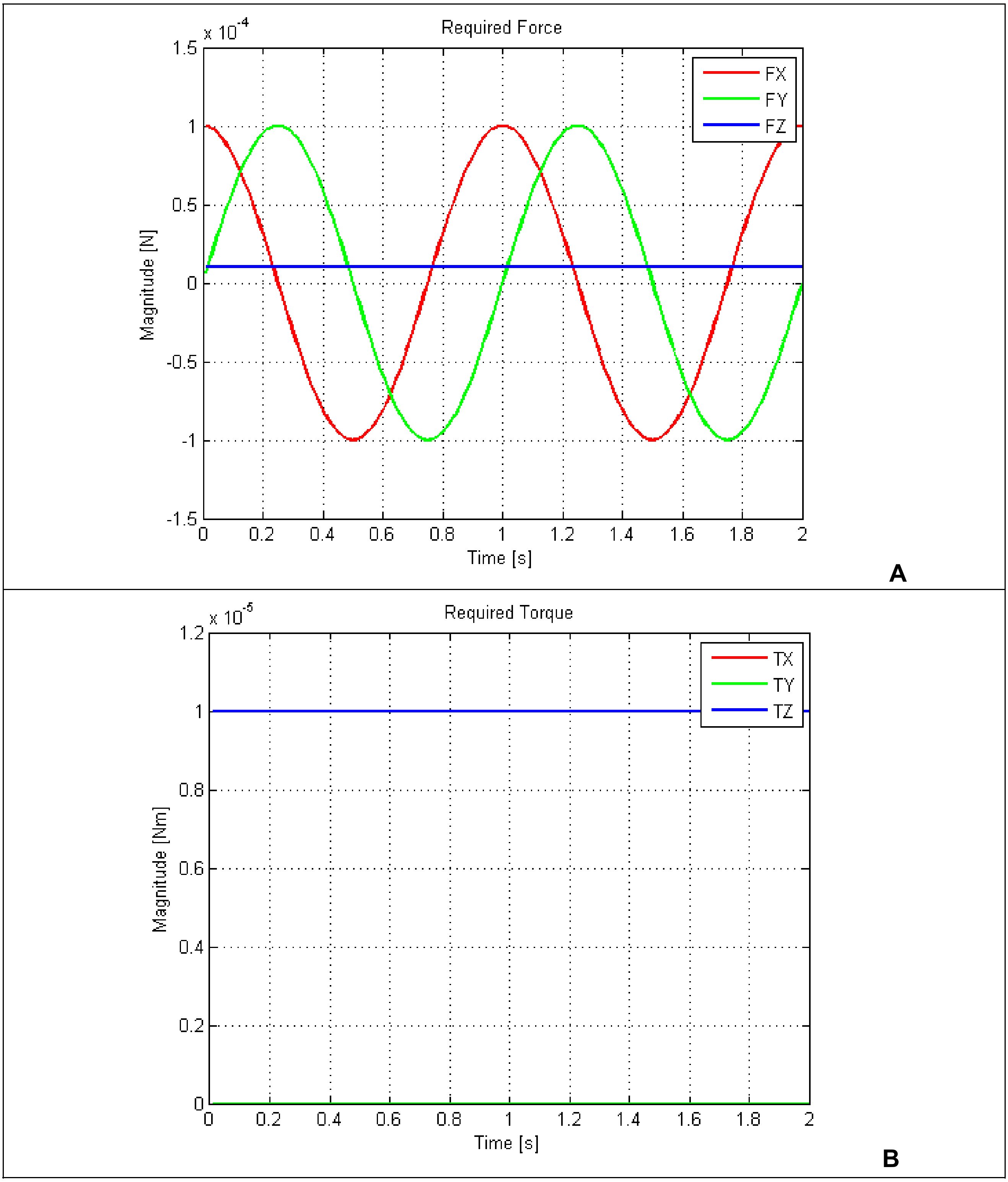

Figure 9-14 – Operating profile – Required force (A) and torque (B).

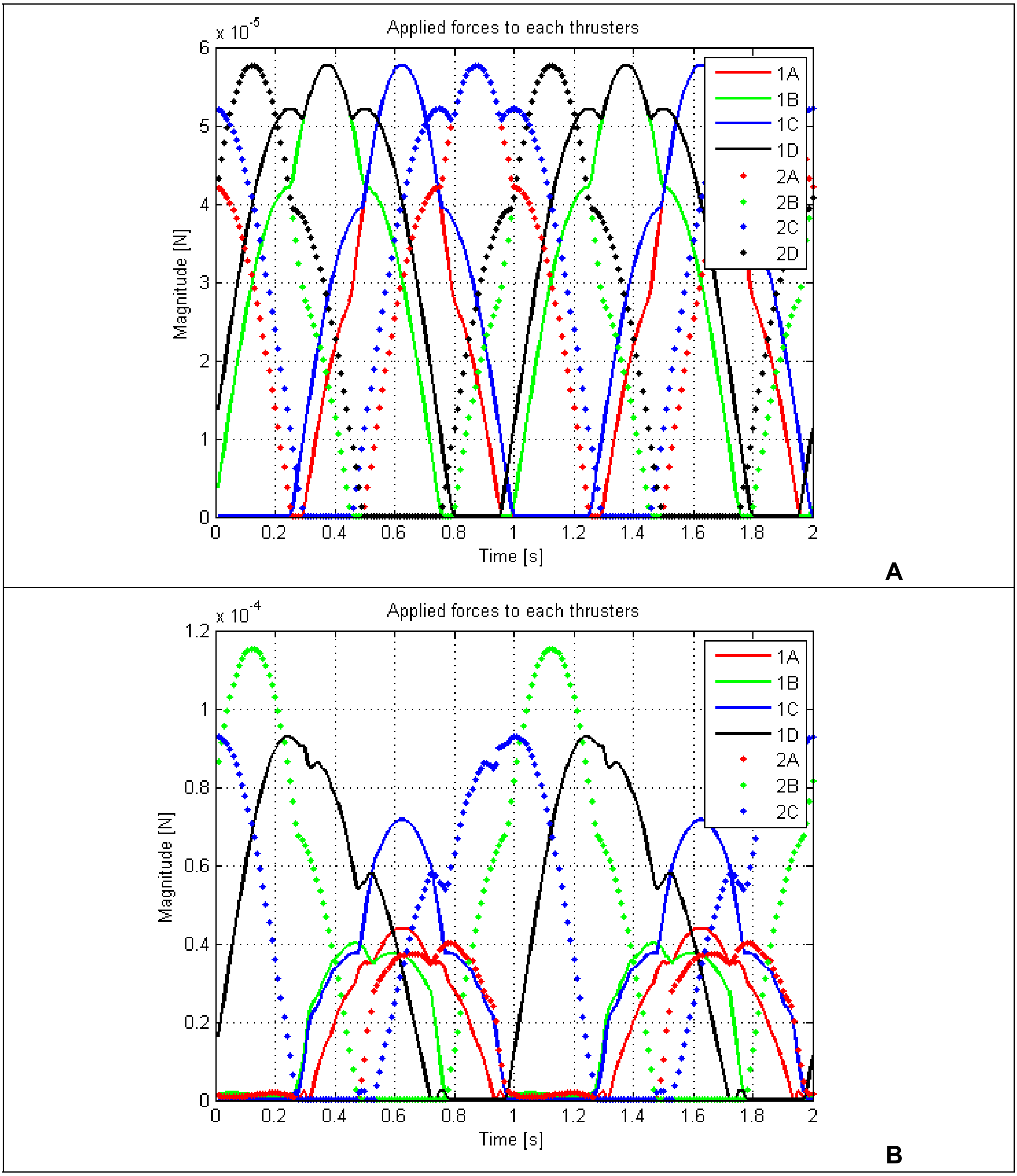

Figure 9-15 – Commanded force to each thrusters: without failure (A) and with 2D thruster fault (B).

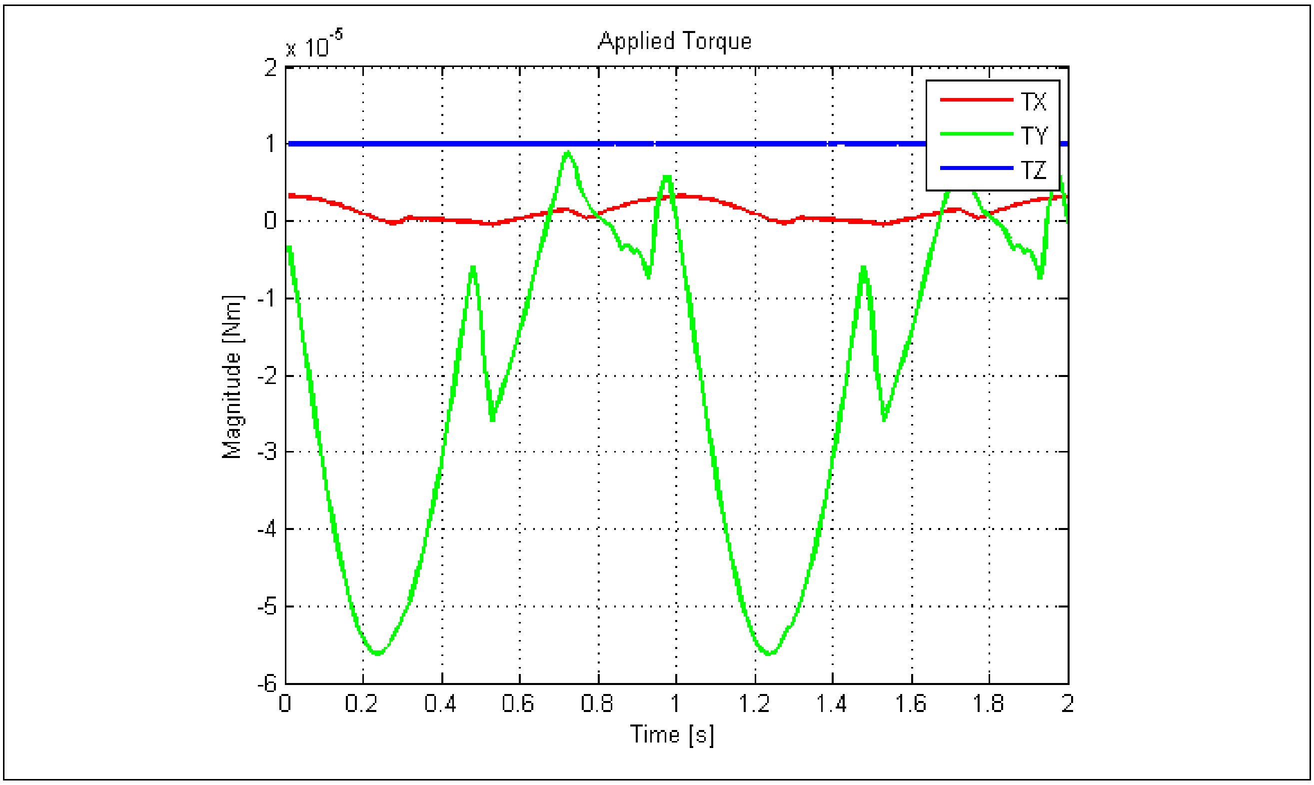

Figure 9-16 – Applied torque with 2D thruster out. In addition to the required torque around Z axis, spurious torque around X and Y are present

Operating condition	Mean [Ns/s]	Max [Ns/s]
No failure	2.6500e-005	3.2633e-005
1 Failure	2.9061e-005	6.4402e-005

Table 9-5 – Required total impulse by each thrusters for each satellite rotation (1s)

9.3.2 Cold-gas thruster solution

The same consideration done for FEEP assembly may be considered still valid for cold-gas solution. It has been observed that the solution based on 6 thrusters only releases torque that may produce de-pointing.

The solution with 8 thrusters is recommended for a two year mission; possible improvements will be considered in Phase B. The propellant mass has been derived considering a simplified assembly (optimization will be still possible).

Assembly : 13380Ns (two years mission)

Considering a two years mission, the propellant required is 23kg (Isp=60s).

10. DRAG-FREE SENSOR

10.1 Requirements

Starting from results of previous study phase, and preliminary analiysis it has been possible to derive requirements for other equipment involved in drag-free like capacitor sensors (for PGB-spacecraft relative position measurements) and high-accuracy rate sensor (to permit the controller gains computation).

10.2 Description of the equipment

10.2.1 Capacitor sensors for PGB and spacecraft COM relative position

Capacitor sensors are used to measure the displacement between PGB and spacecraft COM. According to the results provided in chapter 7, the measurement accuracy at frequency in a neighbour of the spacecraft spin rate shall be:

$$N_{MDF\_XY} \leq 0.5\,10^{-6}\ \mathrm{m}/\sqrt{Hz}$$

$$N_{MDF\_Z} \leq 4\,10^{-6}\ \mathrm{m}/\sqrt{Hz}$$

From those requirements, taking into account the stage of the program, the following requirement shall be considered for the design:

- XY plane

  $N_{MDF\_XY} \leq 0.05\,10^{-6}\ \mathrm{m}/\sqrt{Hz}$

  bias < 10^{-5} m

- Z channel

  $N_{MDF\_Z} \leq 0.4\,10^{-6}\ \mathrm{m}/\sqrt{Hz}$

  bias < 10^{-5} m

10.2.2 Spin rate sensor

Taking into account the unavailability of off-the-shelf equipment due to high relative accuracy and high angular rate (at beginning of Phase A2 the required angular rate was 720deg/s), specific equipment has been designed by TAS-I in cooperation with SILO. During the Phase 2 the design has evolved, and, taking into account the lower spin rate, other solutions may be considered too. In early Phase B, the use of such sensor will be addressed again, to provide the most effective solution (cost, performances).

A small telescope endowed with Position Sensing Detectors (PSD) as focal plane detects Sun position from the position of the light spot focused on the PSD.

Sensor main features are:

- square camera design to detect Sun for the whole year
    - Field Of View (FOV) corresponding to Sun annual declination range i.e. ± 25°
- optical system focusing light spot on PSD sensing area
- PSD outputs:
    - Optical power of detected light source i.e. Sun
    - Coordinates of light spot focused on PSD sensing plane, translating into angular measurement of Sun position

The sensor accommodation will be normal to the satellite spin axis.

The internal section view is provided in Figure 10-1.

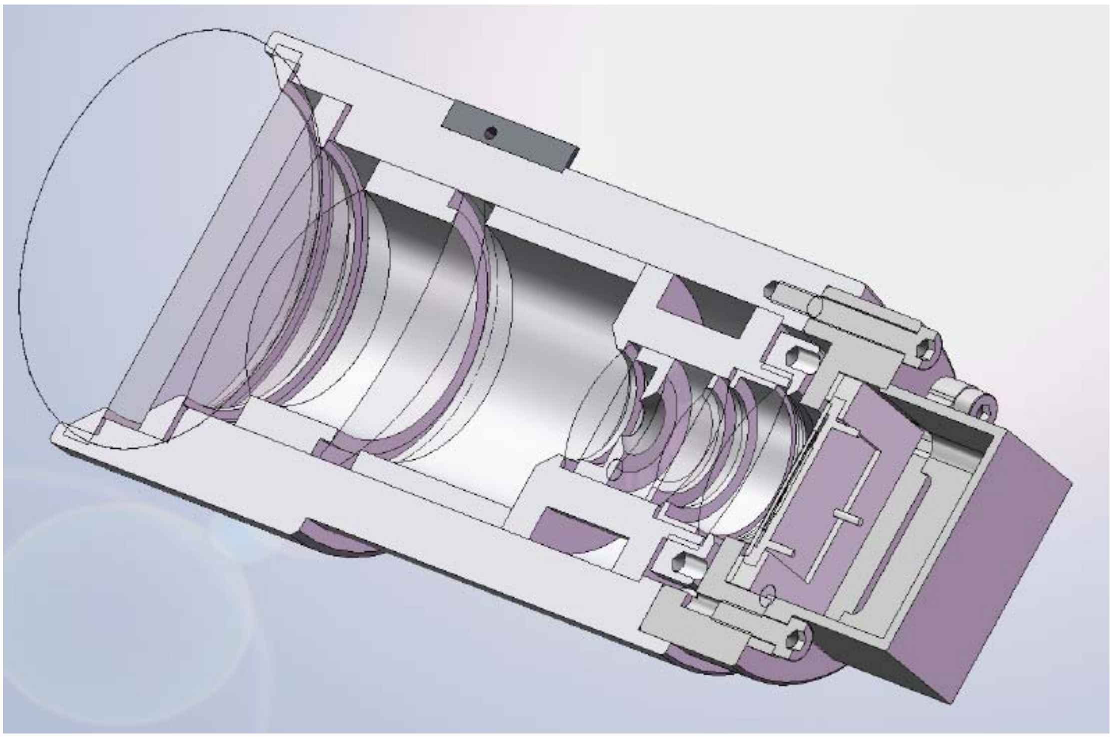

Figure 10-1 – Spin rate sensor - Internal section view

The sensor gives also Sun coordinates, providing additional Sun information to be used together with SSS for cross-check.

11. CANDIDATE EQUIPMENTS – BASELINE DEFINITION

11.1 Gyroscope

A coarse gyroscope has been considered for rate damping, coarse pointing and to have a more robust spacecraft spin-up. It shall be without moving part (e.g. FOG or RLG instead of HRG).The following solutions have been proposed:

- Northrop Grumman LN-200;
- Northrop Grumman μFORS-6U;
- Honeywell MIMU.

The Northrop Grumman gyroscopes and Honeywell MIMU have a dynamic range compatible with spin-up.

The baseline sensor is Northrop Grumman LN-200, candidate also for EXOMars ESA mission. It a three axis gyroscope and two units are required.

Litef μFORS-6U is a one axis gyroscope and then 4 units are necessary. Northrop Grumman μFORS-6U has been used in the mission Sloshsat FLEVO[8] and LAPAN-TUBSAT[9].

Honeywell is the best solution in terms of performance, but it is very expensive. The use of such a equipment permits to delete the spin-rate sensor (to be verified in phase B)

Manufacturer	Northrop Grumman
Product name	LN200S
Description	3-axis solid state FOG with EU, no internal redundant
Heritage	Clementine, Deep Space I, GRACE, candidate also for EXOMars
Mass	0.75 kg
Power	12 Watt
Interface	RS-422/485
Dynamic range	±1000 deg/s
Bias (full temperature)	1 °/hour
Bias stability (RRW)	0.1 °/hour in 1 hour
Angle Random Walk (ARW)	0.07 °/√hour
Scale factor	100÷500 ppm
Warm-up time	0.1s

---

[8] ESA mission, NLR (prime) mini satellite for the study of liquid dynamics. Launched with ARIANE 5 ECA V164, 12/02/2005

[9] Indonesian Berlin University

Table 11-1 - Northrop Grumman LN-200S technical data

Figure 11-1 - Northrop Grumman LN-200S

Manufacturer	Northrop Grumman
Product name	μFORS-6U
Description	1-axis FOG gyro with EU , no internal redundant
Heritage	Sloshsat FLEVO, LAPAN-TUBSAT
Mass	<0.15kg
Power	2.3 Watt
Interface	RS-485
Dynamic range	±1000 deg/s
Bias (full temperature)	< 6 °/hour (1 sigma)
Bias stability (RRW)	3 °/hour in 1 day (stabilized temperature)
Angle Random Walk (ARW)	0.15 °/√hour
Scale factor	2000 ppm (1σ, day to day repeatability)
Warm-up time	0.1s

Table 11-2 - Northrop Grumman μFORS-6U Gyroscopes technical data

Figure 11-2: Northrop Grumman μFORS-6U

Manufacturer	Honeywell
Product name	MIMU
Description	3-axis RLG gyro
Heritage	Flown on LEO, GEO and Deep Space probe mission
Mass	4.7 kg
Power	22 Watt (typical), 32 Watt (max)
Interface	RS-422, MIL-STD-1553
Dynamic range	±375 deg/s
Rate Bias Drift (RBD)	0.005 °/hour (1σ)
Angle Random Walk (ARW)	0.005 °/√hour (1σ)
Scale factor	1 ppm (1σ)
Warm-up time	22s

Table 11-3 - Technical data of the Honeywell MIMU 3-axes rate sensor

Figure 11-3: Honeywell MIMU

11.2 Magnetometer

Magnetometers are used for spacecraft coarse z-axis pointing. It shall be without moving part (e.g. flux-gate). Three units with three-axis magnetometer shall be considered (electronic board is not redundant). Possible commercial solutions are:

- IAI TAMAM Model 2425;
- LusoSpace magnetometer;
- TFM100SH Billingsley Aerospace and Defence.

Manufacturer	Model 2425
Product name	IAI TAMAM
Description	Three axis flux-gate magnetometer
Heritage	PRIMA platform – Cosmo SkyMed
Mass	0.185 kg
Power	< 0.8 Watt
Data interface	analogue
Power supply	±15 V
Range	60 μTesla
Noise	10 nTesla (1σ, up to 20Hz)
Axis misalign.	±0.1°
Linearity	±0.1% (3σ)
Bandwidth	50÷100 Hz (adjustable)

Table 11-4 – IAI TAMAM Model 2425 magnetometer technical data

Manufacturer	Lusospace
Product name	AEOLUS, PROBA2
Description	Three axis flux-gate magnetometer
Heritage	
Mass	0.3 kg
Power	< 1 Watt
Data interface	analogue
Power supply	15÷40 V
Range	70 μTesla
Noise	20 nTesla (1σ)
Axis misalign.	±0.1°
Linearity	±0.2%
Bandwidth	40 Hz

Table 11-5 – Lusospace magnetometer technical data

Figure 11-4: LusoSpace magnetometer

IAI TAMAM Model 2425 magnetometer have been selected are baseline for PRIMA bus. The sampling frequency shall be in the order of 10-20 Hz, with a bandwidth of the magnetometer not lower than 20Hz. Table 11-4 reports the IAI TAMAM magnetometer technical data; Table 11-5 reports the Lusospace magnetometer technical data.

11.3 Sun Sensor

Sun detection assembly is constituted by two Sun sensors mounted in +X body axes.

The candidate equipment is the Smart Sun Sensor (SSS), manufactured by Selex Galileo Avionica.

Manufacturer	Selex Galileo Avionica
Product name	Smart Sun Sensor
Description	Digital Sun sensor based on APS technology
Heritage	GOCE
Mass	0.4 kg
Power	<1.3 Watt
Data interfaces	RS-422
Power supply	up to 50V (16 to 40V nominal) or pre-regulated 5.5V±5%
Field of View (FoV)	±64°
Accuracy	0.01° (1σ) at low rate 0.015° (1σ) at 15rpm 0.02° (1σ) at 30rpm and higher

Table 11-6 – Smart Sun Sensor from Selex Galileo Avionica

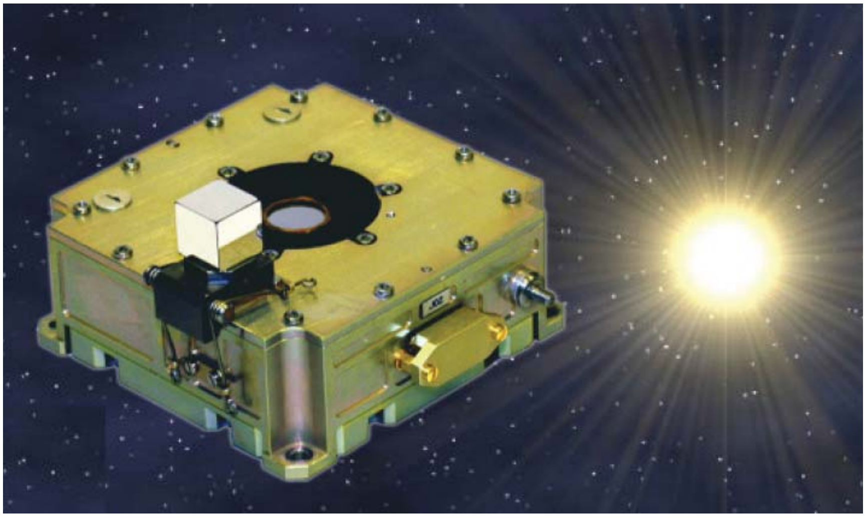

Figure 11-5 – Selex Galileo Avionica Smart Sun Sensor (SSS)

12. SIMULATION RESULTS

12.1 Introduction

In the following, the major results related to most challenging XY drag-free and XY whirl controllers will be provided. Equipment parameters have been considered in agreement with the specified values.

The presentation has been organized in lower level chapters devoted to:

- simulated perturbing force;
- simulation results without whirl and drag controls;
- simulation results trajectory with whirl control and without drag control;
- simulation results trajectory with whirl and drag controls.

12.2 Simulated perturbing force

The simulated perturbing force takes into account the drag only. The drag force profile time series and its amplitude spectrum both given in the inertial reference frame are shown in Figure 12-1 and in Figure 12-2 respectively. Figure 12-3 shows the drag force in body reference frame with spacecraft spin rate equals to 1Hz. Drag force amplitude has been scaled in order to provide a maximum linear acceleration equals to 0.2 10-6 m/s2. The orbital period is about 5800s (600km).

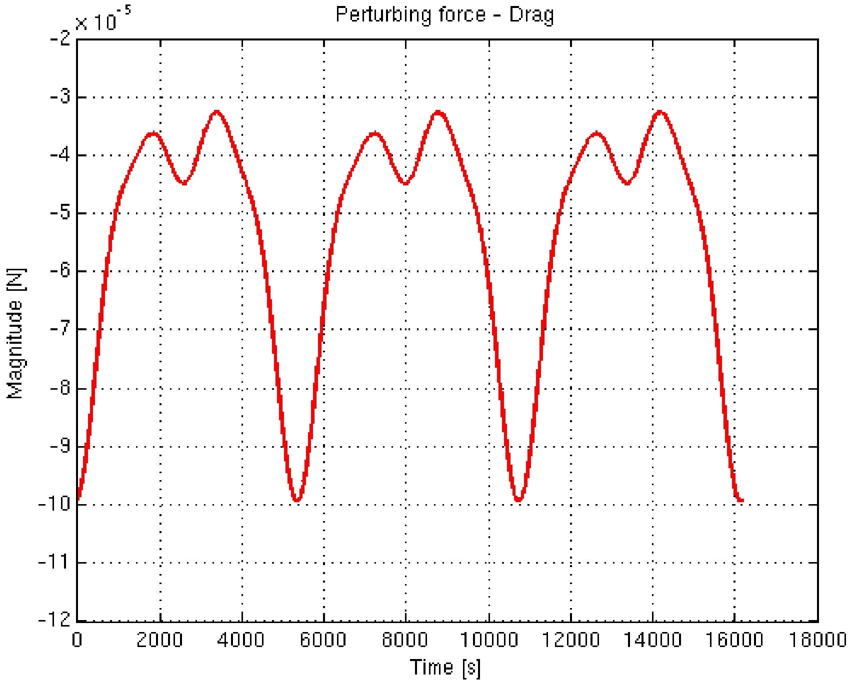

Figure 12-1 – Simulated drag profile

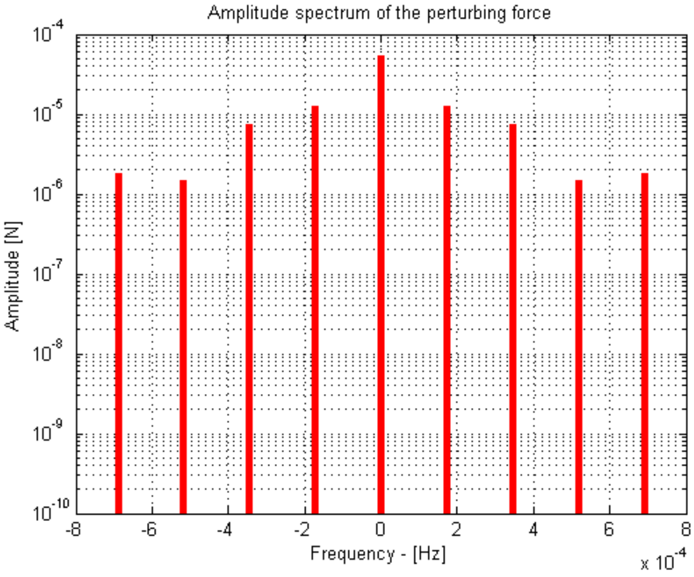

Figure 12-2 – Amplitude spectrum of the simulated drag profile

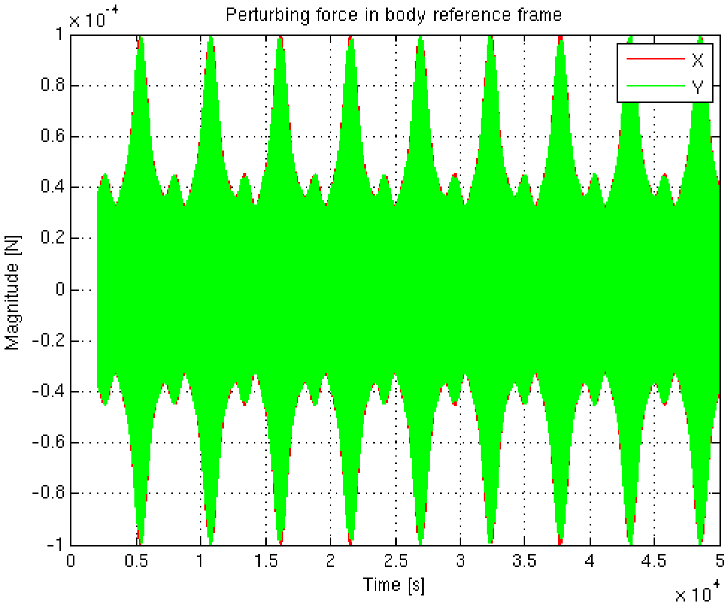

Figure 12-3 - Time series of the XY plane perturbing force (body reference frame)

12.3 Simulation results without whirl and drag controls

Figure 12-4 shows the XY displacements as function of time without whirl and drag-free controllers. The growing of magnitude of X and Y relative positions due to instability is evident. Figure 12-5 shows a zoom of the XY movements.

Figure 12-6 and Figure 12-7 provide the XY displacements in phase diagram.

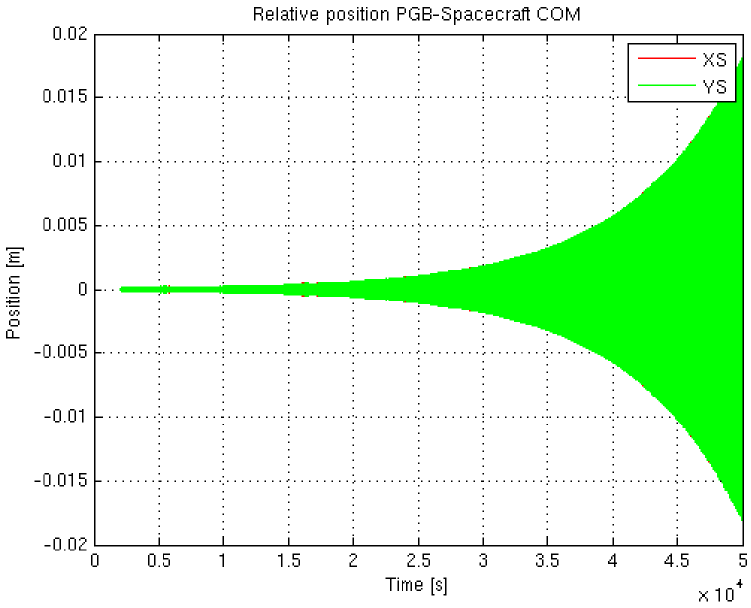

Figure 12-4 – Time evolution of the PGB- spacecraft COMs relative position

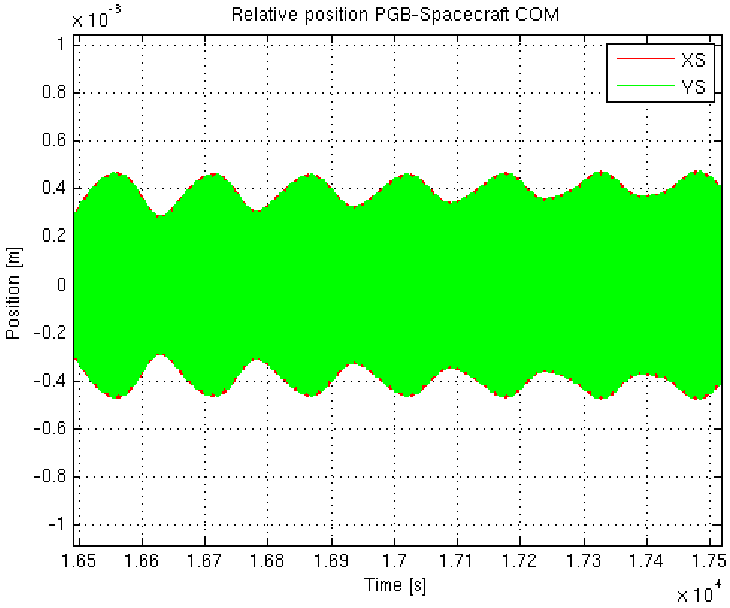

Figure 12-5 – Time evolution of the PGB- spacecraft COMs relative position (zoom)

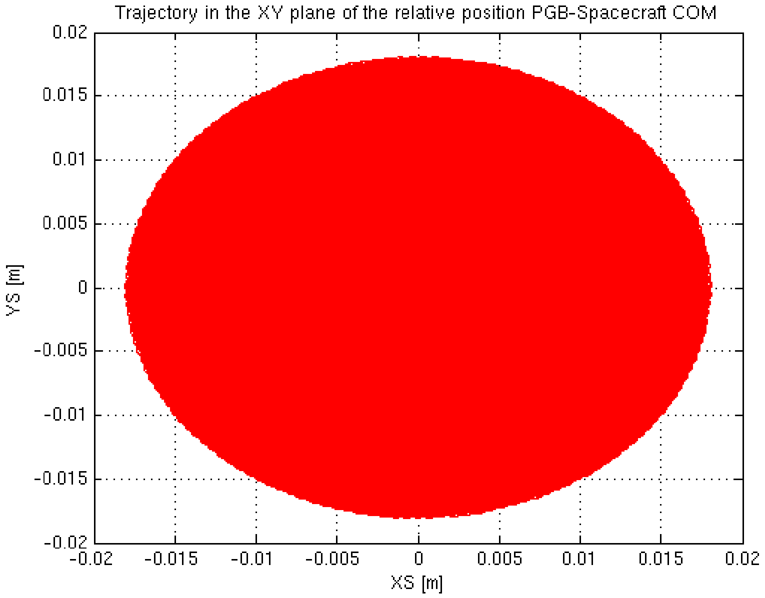

Figure 12-6 – Phase diagram of the PGB- spacecraft COMs relative position

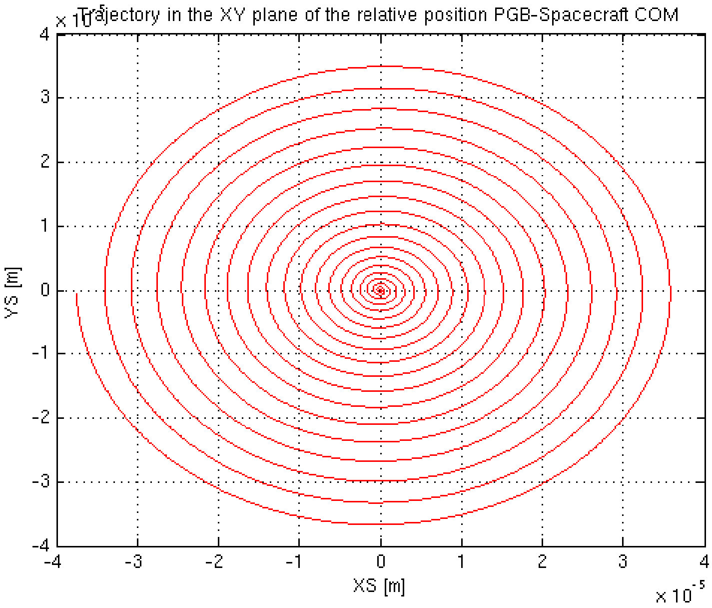

Figure 12-7 – Phase diagram of the PGB- spacecraft COMs relative position (zoom)

12.4 Simulation results trajectory with whirl control and without drag control

Figure 12-8 and Figure 12-9 show the XY displacements as function of time with whirl control and without drag-free control. The pictures show the effectiveness of the stabilization introduced by control law.

Figure 12-10 and Figure 12-11 show the one-side spectral density of the XY PGB-spacecraft relative position given in body reference frame. It is possible to recognize around 1 Hz the rows due to the perturbing force spectrum (see also Figure 12-2). The maximum value of the relative position spectral density around 1Hz, computed with a frequency resolution equals to about 2 10^{-5} Hz, is 7 10^{-3} m/√Hz.

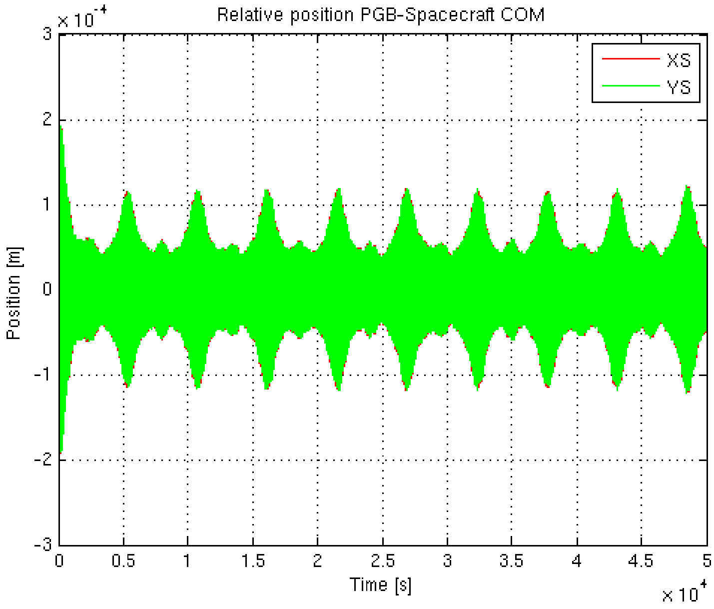

Figure 12-8 – Time evolution of the PGB- spacecraft COMs relative position (body reference frame)

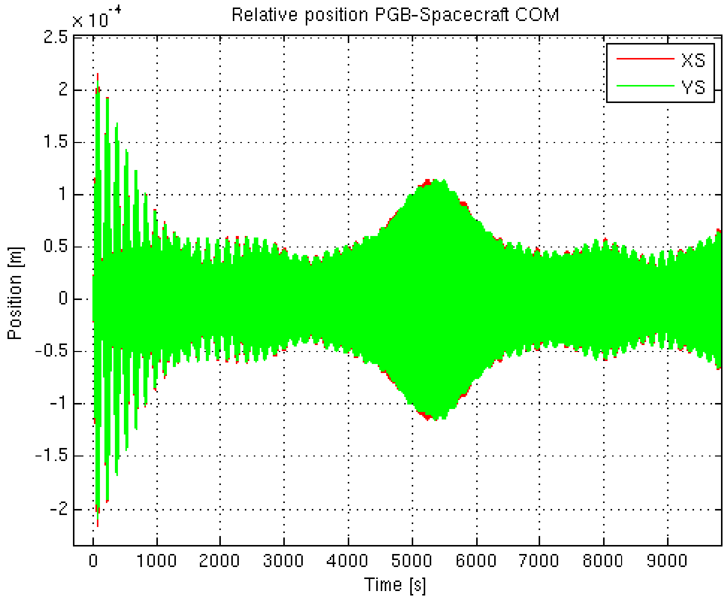

Figure 12-9– Zoom of the PGB- spacecraft COMs relative position (body reference frame)

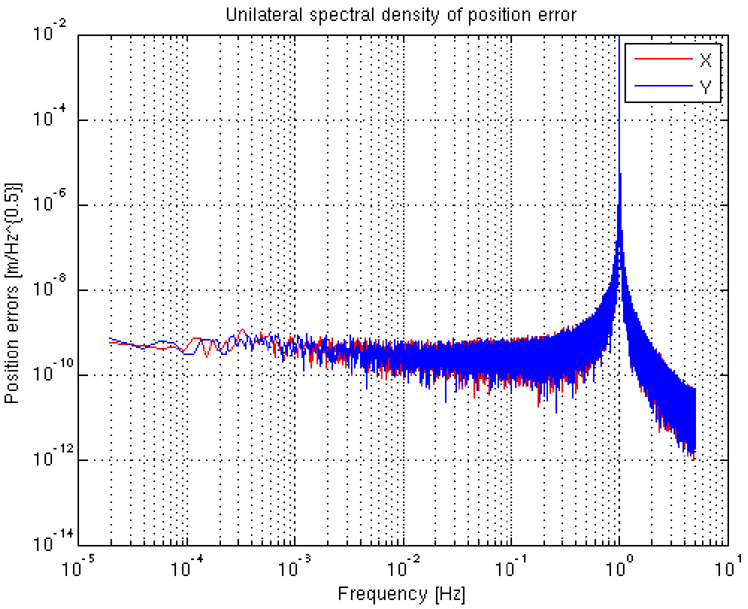

Figure 12-10– One-side spectral density PGB- spacecraft COMs relative position (body reference frame)

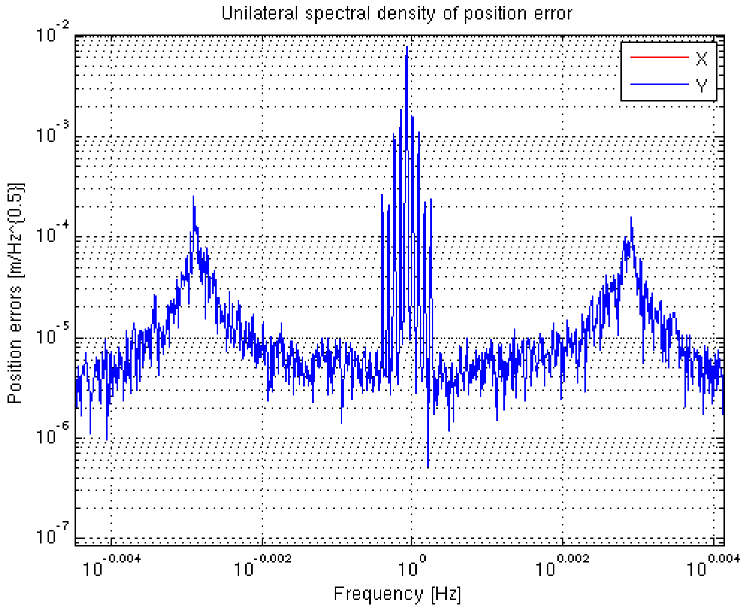

Figure 12-11– Zoom around 1Hz of the one-side spectral density PGB- spacecraft COMs relative position (body reference frame)

12.5 Simulation results trajectory with whirl and drag controls

Results provided in the pictures below have been obtained considering a relative uncertainty on spacecraft spin rate equals to 10^{-4} Hz (one order of magnitude worse that the required value).

Two cases have been considered:

- without capacitor sensors measurement noise (Figure 12-12, Figure 12-13, Figure 12-14 and Figure 12-15). This case is relevant to appreciate the drag compensation capabilities provided by the designed control;
- with capacitor sensors measurement noise (Figure 12-16 and Figure 12-17). It permits to see the end performances, to be considered for scientific post-processing.

Comparing the maximum spectral density around 1Hz given Figure 12-11 and Figure 12-15, it is possible to observe that the rejection on drag-disturbances provided by XY drag-free controller is lower than 1/150000 with a relative uncertainty on angular rate knowledge equals to 10-4.

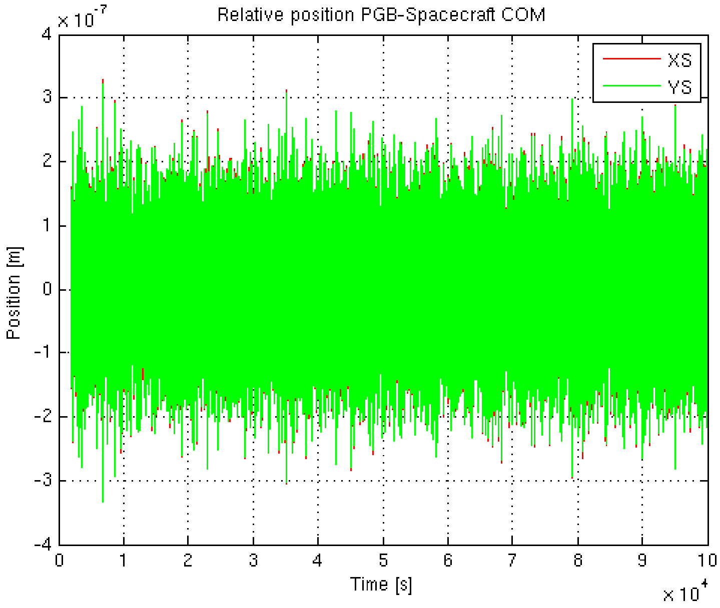

Figure 12-12– Time evolution of the PGB- spacecraft COMs relative position (body reference frame, without measurement noise)

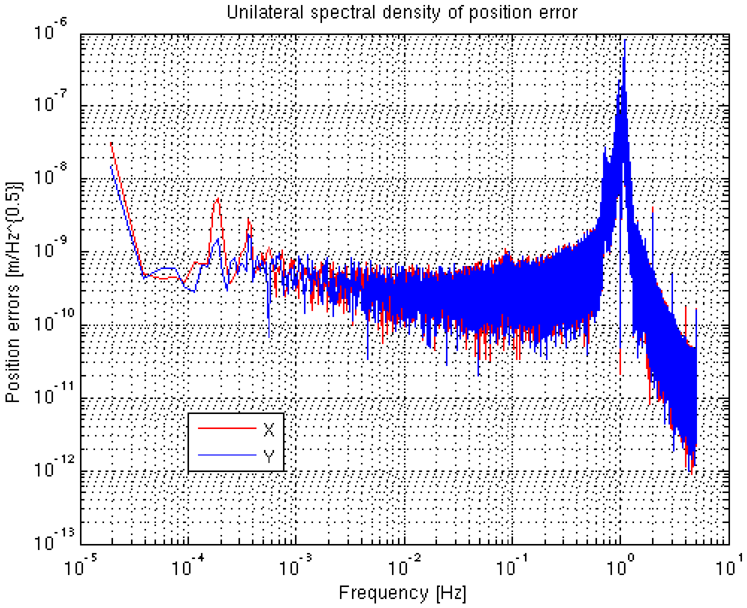

Figure 12-13– One-side spectral density PGB- spacecraft COMs relative position (body reference frame, without measurement noise)

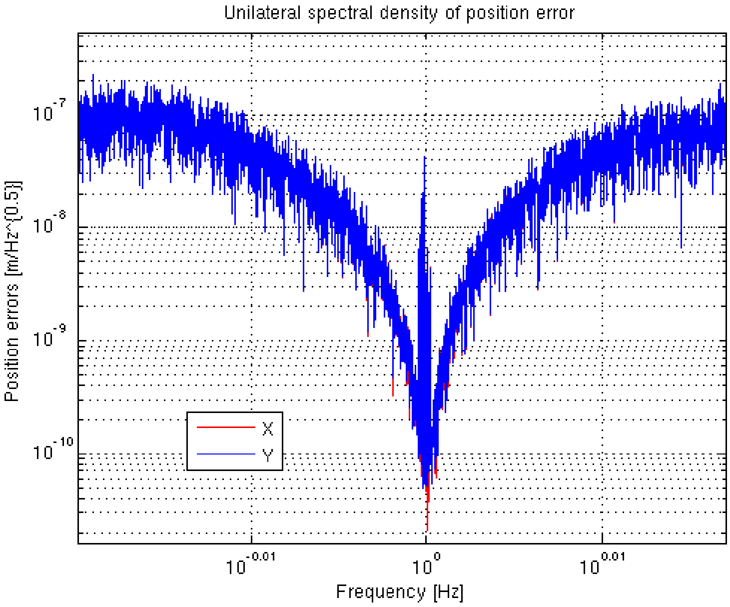

Figure 12-14– Zoom around 1Hz of the one-side spectral density PGB- spacecraft COMs relative position (body reference frame, without measurement noise)

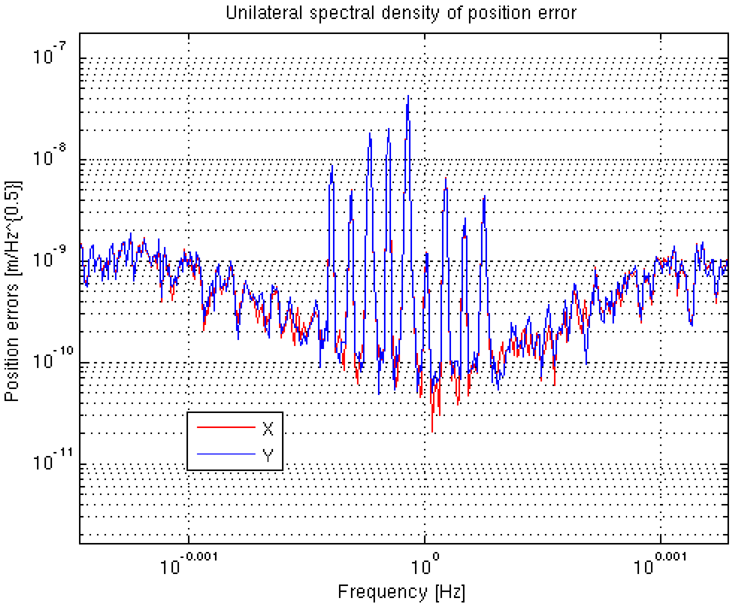

Figure 12-15– Zoom around 1Hz of the one-side spectral density PGB- spacecraft COMs relative position (body reference frame, without measurement noise)

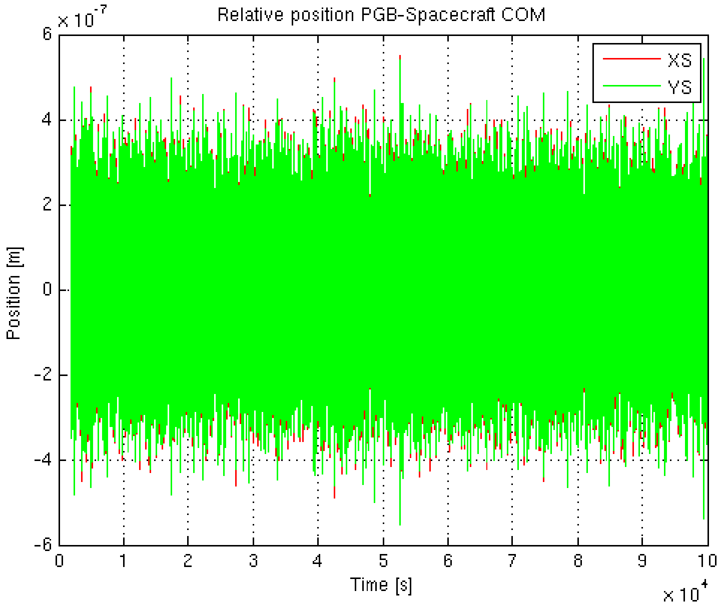

Figure 12-16– Time evolution of the PGB- spacecraft COMs relative position (body reference frame, with measurement noise)

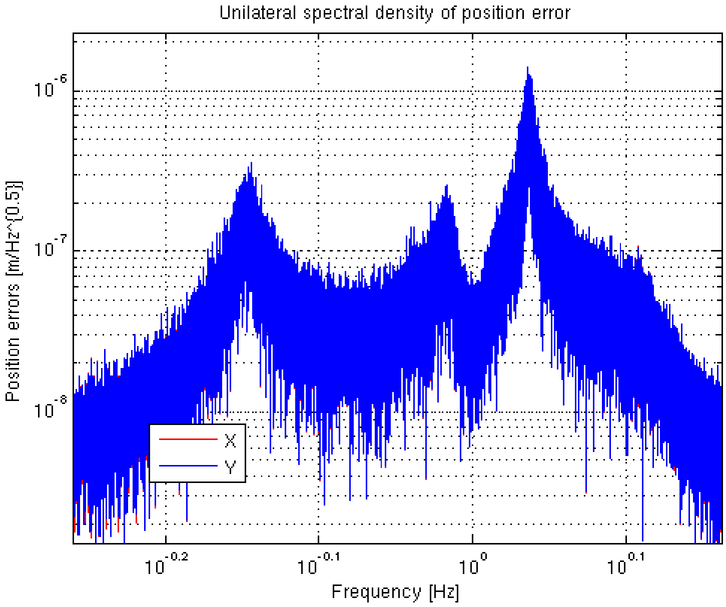

Figure 12-17– Zoom around 1Hz of the one-side spectral density PGB- spacecraft COMs relative position (body reference frame, with measurement noise)

13. CONCLUSIONS

The technical note has summarized the requirements, the architecture, the algorithms, the specific technologies and the results for the Drag Free and Attitude Control sub-system.

At it has been shown, the design of the basic algorithms for fine drag compensation is completed. As usually, they will be completed with additional logics not relevant for the performance but relevant for system robustness (failure detection and isolation, sensors monitoring, etc.) during the Phase B.

Results from simulation clearly show that:

- the proposed solutions permit to meet requirements with margins considering already available technologies.
- during Phase A2 of the study, improvements in the control performances has been achieved.

Minor open points are still present on thrusters' performances (particularly for response time, and maximum centrifugal acceleration). Two technologies have been considered, both leaded by Italian industries:

- Field Emission Electrical Propulsion (FEEP) from ALTA S.p.A.;
- Cold gas propulsion system (CGPS) from TAS-I S.p.A.

FEEP Thrusters are being developed for the ESA Lisa Pathfinder (LPF) mission and the CNES Microscope mission. Thruster development is nearly completed, and the preparation of the Lisa Pathfinder FEEP Cluster Assembly (FCA) Qualification Model is ongoing. Manufacturing of FM parts for LPF was also released.

GAIA Cold-gas Micro Propulsion system (GCPS), currently under qualification at TAS-I, represents the reference design and technology starting points for configuring/realizing both Microscope and Galileo Galilei.

ESA Lisa Pathfinder FEEP are almost in line with required response time, but need modifications of tank positioning and shape to meet the requirement on maximum centrifugal acceleration. Additional activities during Phase B are needed to extend the performances of already available LPF FEEP to GG FEEP.

GAIA CGPS are compliant with required maximum centrifugal acceleration, but need modifications on electronic box and control algorithms to meet the requirement on response time. Additional activities during Phase B are needed to extend the performances of already available GAIA CGPS to GG CGPS.

The following activities already outlined during current study phase shall be investigated in mode details during Phase B to consolidate the proposed design:

- possible improvement in thrusters assembly finalized to fuel reduction and to reduce the impact on satellite spin-axis pointing after one FEEP failure;
- relaxation of response time for micro-propulsion thrusters;
- calibration procedure for three axis magnetometers to improve the spin-axis pointing and determination accuracies;
- review of spin rate measurement requirement to verify the necessity of the additional spin rate sensor (spin-rate may be also estimated using of-the shelf Smart Sun Sensor, that provide very good accuracy);
- algorithms review finalized to their real-time implementation.

APPENDIX A – FREQUENCY INTERPRETATION OF THE EXPERIMENT

With the objective of providing a simple tool to translate from inertial reference frame to body reference frame and vice-versa, the following chapter has been introduced.

The spacecraft spin-rate may be seen as the carrier of the amplitude modulation scheme (see Figure 0-1). All signal components around the DC in inertial reference frame (drag, solar pressure) are translated around spin rate due to modulation effects.

The controller compensates the perturbing forces, leaving a residual related to controller authority, PGB-spacecraft relative position measurement noise and thruster's noise.

The above residuals are attenuated by the balance in the PGB. The PGB scientific channel providing the relative position between the two proof masses is used by post-processing to detect and to estimate the magnitude of possible EP violation. In Figure 0-1, a simplified but effective (and equivalent) scheme for the post-processing has been proposed (spectrum analysis, maximum likelihood may be actually considered).

Figure 0-2 shows the frequency transformation induced by spacecraft spin-rate, the control action and the post-processing.

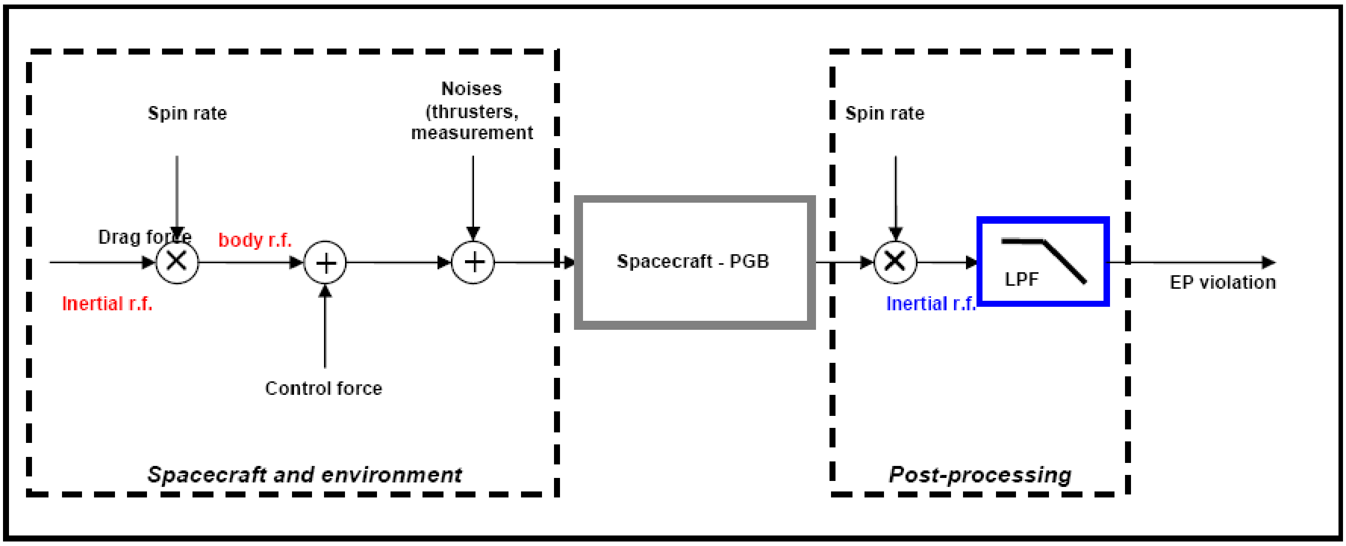

Figure 0-1 – Simplified block diagram of the experiment

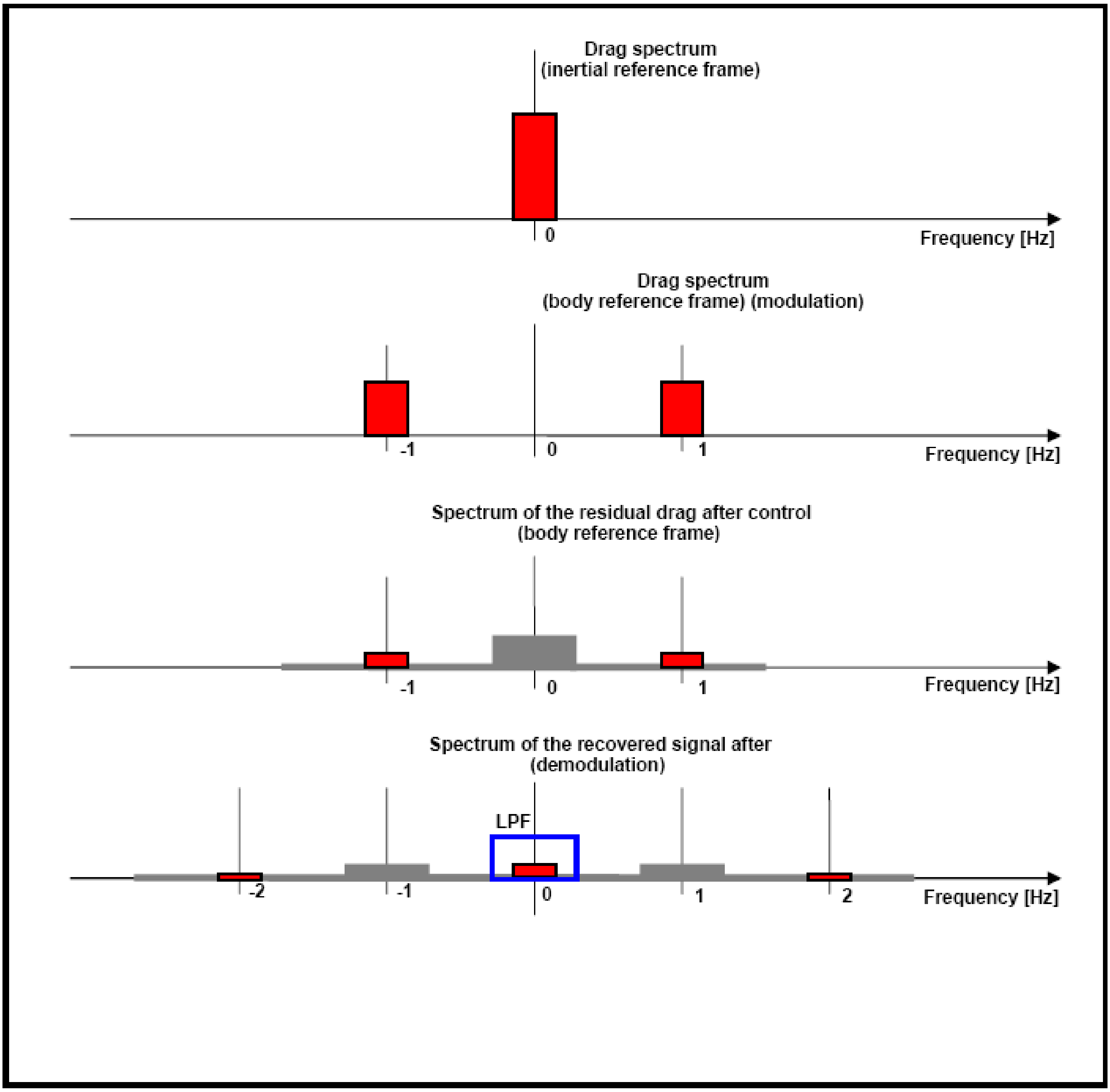

Figure 0-2 – Frequency interpretation of the experiment

14. APPENDIX B – PARAMETERS CONSIDERED FOR THE SPACECRAFT AND PICO-GRAVITY BOX.

No	Parameter	Unit	Value	Comments
1	Spacecraft mass	kg	500	
2	PGB mass	kg	45	
3	PGB suspension quality factor		90	
4	Period of the PGB suspension	s	150	
5	Natural frequency of PGB the suspension	rad/s	0.0419	
6	Spacecraft spin angular rate	rad/s	6.2832	Nominal value. Acceptable variation ±10%
7	Ixx	kgm^2	124.97	
8	Iyy	kgm^2	120.51	
9	Izz	kgm^2	155.1	
10	Ixy	kgm^2	-2.79	
11	Ixz	kgm^2	0	
12	Iyz	kgm^2	0	

Table 14-1 – Nominal values of relevant spacecraft and suspension parameters used as reference for control design

The values presented in the above table are not coming from the last spacecraft configuration. In any case they are very close, and all considerations and analysis are still totally valid.

15. APPENDIX C – PERTURBING FORCE AND TORQUE

Perturbing force and torque due to environment has been computed. The spacecraft surface has been described by a finite number of surfaces, considering specific electro-optics and aerodynamic coefficient. The reference shape and dimension of the spacecraft are given in Figure 15-1and Figure 15-2.

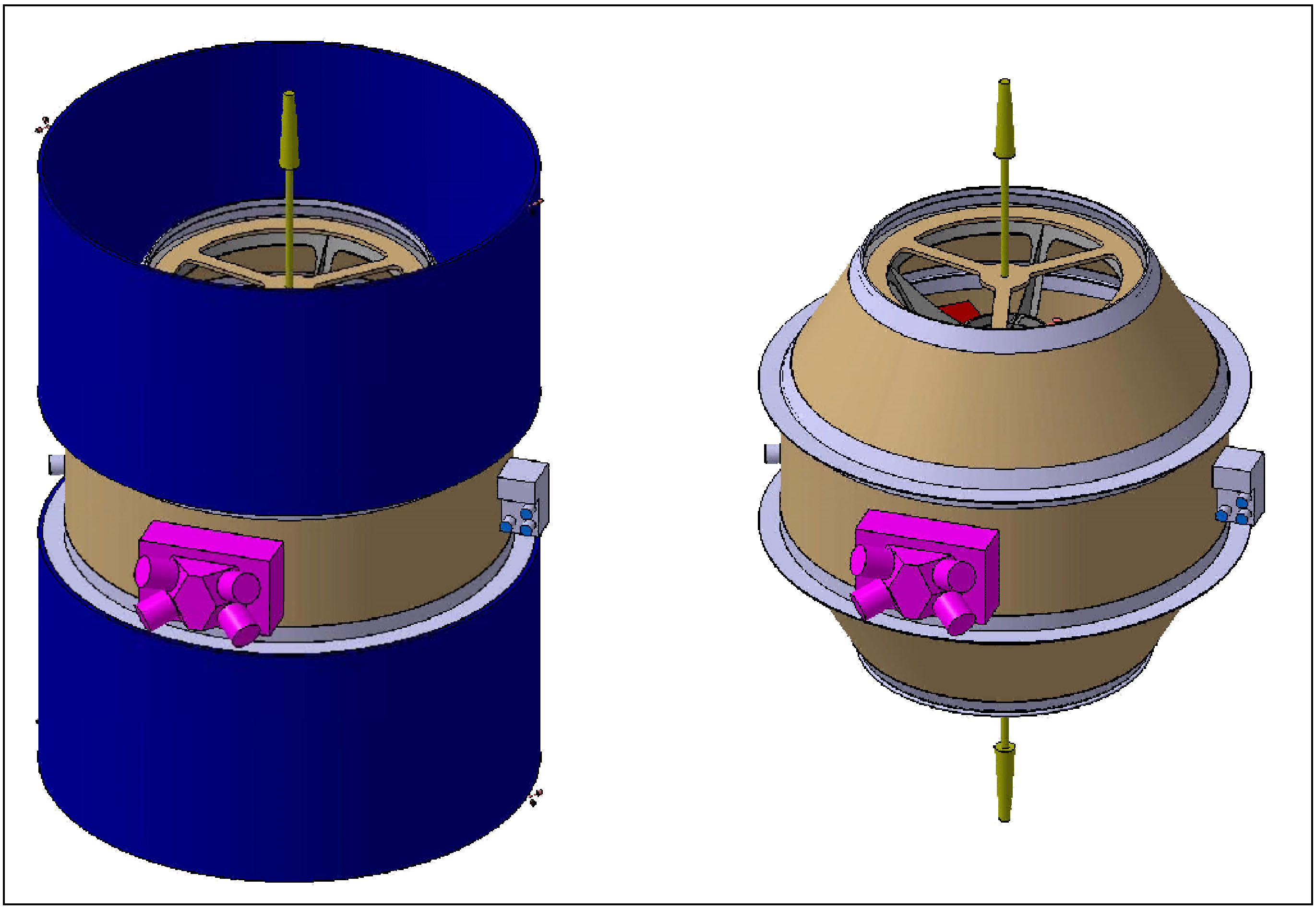

Figure 15-1 – Galileo Galilei spacecraft (left) and main body without solar array (right)

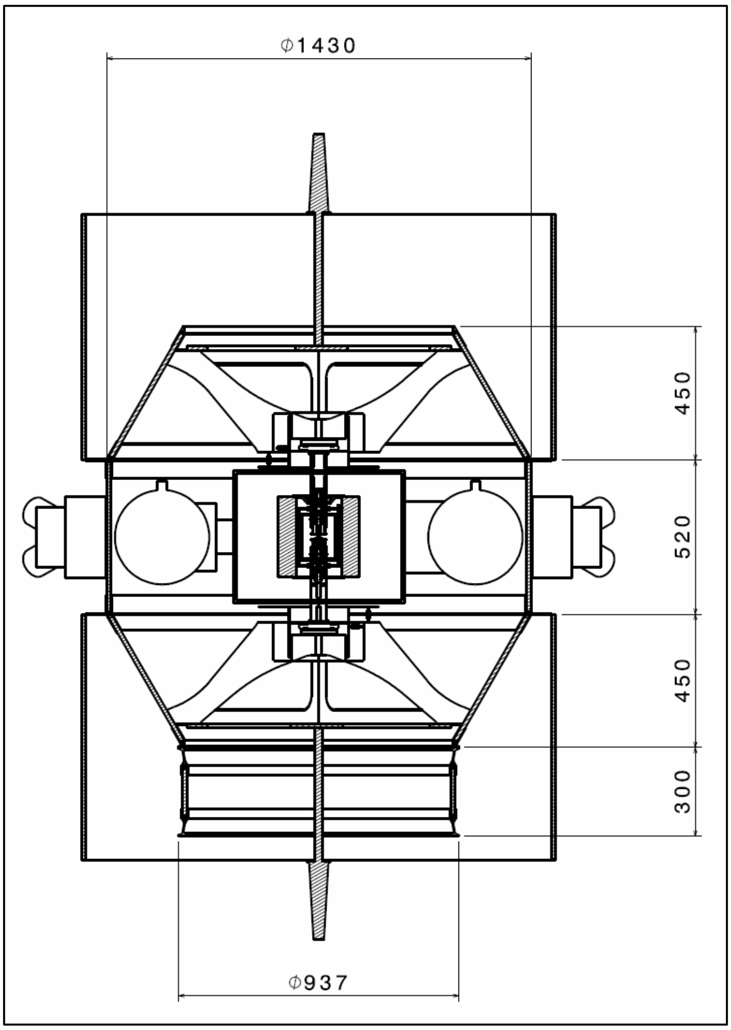

Figure 15-2 – Galileo Galilei spacecraft relevant dimension

Table 15-1 collects the parameter for each kind of surface. Table 14-1 provides the mass properties considered for any computation presented in the TN.

Table 15-2 provides the derived results.

Surface	Ca	Cs	Cd	Cx
Solar array	0.89	0.0	0.11	2.0
mlay	0.090	0.683	0.228	2.0
feep cluster	0.090	0.683	0.228	2.0
Top and bottom covers	0.090	0.683	0.228	2.0

Table 15-1 – Surface properties

Perturbation	**Force [μN]**	**Torque [μNm]**	**Comments**
Solar pressure	10	0.1	Separation between COM and COP 0.1m
Drag	100	10	Separation between COM and COA 0.1m
Gravity gradient	0	30	
EMF interaction	0	15	The dipole has been provided as a requirement: < 0.5Am2

Table 15-2 – Surface properties

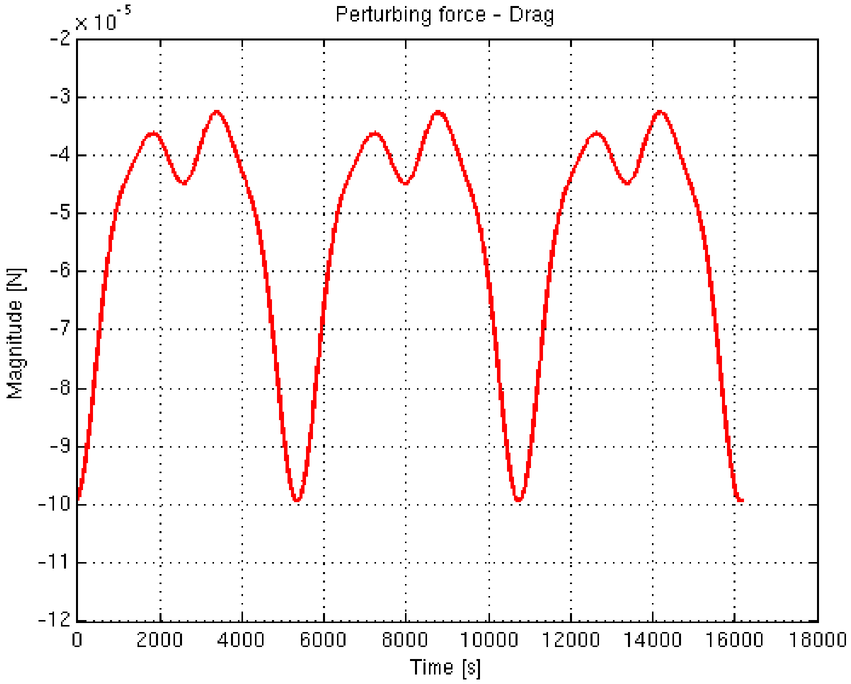

Figure 15-3 – Simulated drag profile

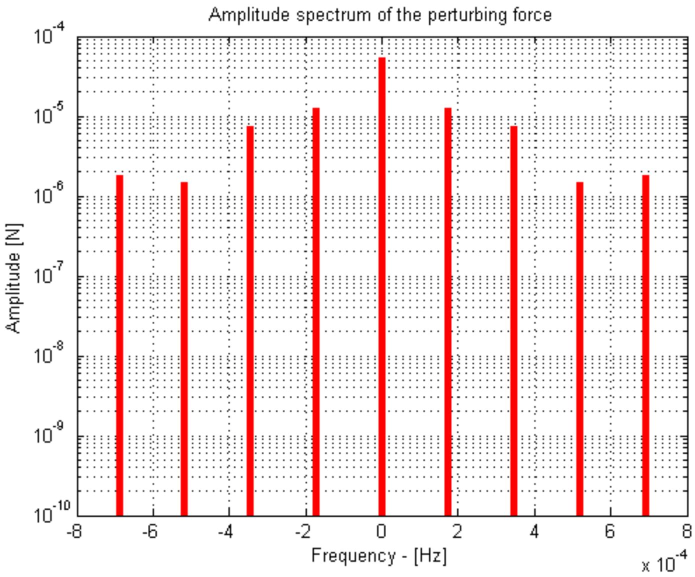

Figure 15-4 – Amplitude spectrum of the simulated drag profile

16. APPENDIX D – CONTROLLERS PARAMETERS

16.1 Introduction

The following chapter contains all the parameters used by designed control algorithms.

16.2 XY drag free-controller

16.2.1 Observer matrix

Matrix A

```
    -7.967955993166342e-01     9.985437335908758e-01     4.995387765851819e-01     1.744159892597718e-04
    -1.032484723398384e+00     9.967966959392451e-01     9.985435509428789e-01     5.231157835677468e-04
    -3.140020148141537e-01                         0     9.999994516886945e-01     1.047197359799839e-03
    -3.671632367034522e+01                         0    -1.047197359799839e-03     9.999994516886945e-01
```

Matrix Bc

```
      4.995388222537048e-01     9.985437335908770e-01                         0                         0
```

Matrix By

```
      1.795919110328433e+00     1.030732682220121e+00     3.140020148141537e-01     3.671632367034522e+01
```

16.2.2 Controller gains

```
Poli azione di controllo con azione integrativa
0.6   0.6   0.2   0.2
```

16.3 Z drag-free controller

16.3.1 Observer matrix

Matrix A

```
     1.000000000000000e+00     1.000000000000000e-01     5.000000000000001e-03                         0
0                         0
    -1.560584532479721e+01     1.000000000000000e+00     1.000000000000000e-01                         0
0    -3.592306979343688e+01
                         0                         0     1.000000000000000e+00     9.354892170897806e-02
3.039588897244259e-02    -3.075447006509022e+01
                         0                         0                         0     8.090169970096867e-01
5.877852103843443e-01     6.541778822740071e+01
                         0                         0                         0    -5.877852103843443e-01
8.090169970096867e-01     1.942593308399246e+02
    -1.000000000000000e+00                         0                         0                         0
0    -1.338033994019374e+00
```

Matrix Bc
```
5.000000000000000e-03 1.000000000000000e-01 0       0       0       0
```

Matrix By
```
0            1.560584532479721e+01    0       0       0       1.000000000000000e+00
```

16.3.2 *Controller gains*

```
Poli azione di controllo
0.995 0.995
```

16.4 XY whirl controller

16.4.1 *Observer matrix*

Matrix A
```
     1.515608374111622e+00     8.090139220350866e-02     4.517336245120143e-03    -1.096098231270014e+00
5.877910469797624e-02     2.012873681536191e-03
     1.431054638980076e+01     4.396890956060788e-01     8.090139220350866e-02     4.179803956382293e+00
1.096098231270383e+00     5.877910469797624e-02
    -1.216688868319264e-04                         0     1.000000000000000e+00     8.839796578690293e-05
0                         0
     1.096098231270677e+00    -5.877910469797624e-02    -2.012873681536191e-03     1.515608374111347e+00
8.090139220350866e-02     4.517336245120143e-03
    -4.179803956384105e+00    -1.096098231270383e+00    -5.877910469797624e-02     1.431054638979221e+01
4.396890956060788e-01     8.090139220350866e-02
    -8.839796577008634e-05                         0                         0    -1.216688868301386e-04
0     1.000000000000000e+00
```

Matrix Bc
```
     1.000000000000000e-02                         0
     1.000000000000000e-01                         0
                         0                         0
                         0     1.000000000000000e-02
                         0     1.000000000000000e-01
                         0                         0
```

Matrix By
```
    -3.372790134691026e-01     1.175559767273729e+00
    -1.111682939290324e+01    -1.859401048307192e+00
     1.216688868319264e-04    -8.839796578690293e-05
    -1.175559767274392e+00    -3.372790134688273e-01
     1.859401048309004e+00    -1.111682939289469e+01
     8.839796577008634e-05     1.216688868301386e-04
```

16.4.2 *Controller gains*

```
Poli azione di controllo
0.9998       0.9998
```

16.5 Z spin-axis angular rate controller

16.5.1 Observer matrix

Matrix A

```
     1.000000000000000e+00     1.000000000000000e-01                         0                         0
0
    -8.600000000001271e-01     1.000000000000000e+00     1.000000000000000e-01                         0
-1.939999999997187e-01
                         0                         0     1.000000000000000e+00     1.000000000000000e+00
8.100000030673847e-05
                         0                         0                         0     1.000000000000000e+00
2.000001053659161e-07
    -1.000000000000000e+00                         0                         0                         0
7.599999999999998e-01
```

Matrix Bc

```
0       0.01   0       0              0
```

Matrix By

```
      0      8.600000000001271e-01                              0                               0
1.000000000000000e+00
```

16.5.2 Controller gains

```
Poli azione di controllo
0.99   0.99
```

END OF DOCUMENT